Universitat Politècnica de Catalunya

PhD program in Photonics

Quantum nonlinear optics at the single-photon level with cold Rydberg atoms

Author:
María Auxiliadora Padrón Brito

Supervisor:
Prof. Dr. Hugues de Riedmatten

A thesis submitted to obtain the title of Doctor by the Universitat Politècnica de Catalunya

in the

QPSA - Quantum Photonics with Solids and Atoms *group,*
ICFO - The Institute of Photonic Sciences

February 17, 2021

UNIVERSITAT POLITÈCNICA DE CATALUNYA
BARCELONATECH

ICFO

Abstract

Photons are good candidates for carrying quantum information because they are very stable particles: they interact weakly with the medium and barely with each other. However, this has drawbacks when you want to process the information because, in this case, it is preferable to have photon-photon interactions. For example, for applications in quantum repeaters, such interactions would allow deterministic Bell state measurements, increasing the entanglement distribution rate between two remote nodes. Getting two photons to interact with each other efficiently requires mapping them into a nonlinear medium at the single-photon level, that is, a medium that reacts differently when it interacts with a single photon than when it does with two. Such strong nonlinearity has been demonstrated with Rydberg atoms, which are atoms excited to a state with a high principal quantum number.

In this thesis we have performed nonlinear quantum optics experiments using an ensemble of cold Rydberg atoms, where we have studied the properties of the quantum light emitted by these atoms. First, we demonstrated nonlinearities at the single-photon level. To reach this stage, we made several improvements to the previous experimental setup available in the group, of which the implementation of a dipole trap was especially relevant. We evidence quantum nonlinearity by measuring photon antibunching for the transmitted light after interacting with the Rydberg state under electromagnetically induced transparency (EIT). We also showed the generation of single photons on-demand after storing weak coherent states of light pulses as collective Rydberg excitations.

Then, we studied the variation of the light statistic throughout the output pulse after propagating through the medium as Rydberg polaritons, which are superposition states of light and Rydberg excitations. We showed that the properties at the beginning and the end of the pulse

were different from those of the steady state. In particular, the light detected after the input pulse was abruptly turned off gave much stronger suppression of two-photon events. Then, we investigated how to exploit this effect to generate single photons on demand. To do this, we analyzed the quality of the single photons detected at the end of the pulse as a function of the detection probability and compared the results with those obtained by storing the input pulse as collective Rydberg excitations. We showed that the photons were generated more efficiently when increasing the detection window at the cost of deteriorating the single photons statistics.

Finally, we investigated the indistinguishability of the photons emitted by our Rydberg atomic ensemble, a crucial property for using Rydberg atoms as nodes in quantum networks. We also compared the single photons generated after storage under EIT conditions with those obtained using a two-photon Raman excitation to the Rydberg state. We measured the indistinguishability by making them interfere with weak coherent states of light in a Hong-Ou-Mandel experiment. And we showed that, although we obtained better photon statistics under EIT conditions, the indistinguishability from those obtained with Raman excitation was significantly higher.

Resume

Els fotons són bons candidats per transportar informació quàntica perquè són partícules molt estables: interaccionen dèbilment amb el medi i, amb prou feines, entre ells. Això també presenta inconvenients quan es vol processar la informació perquè, en aquest cas, és preferible tenir interaccions fotó-fotó. Per exemple, per a aplicacions en repetidors quàntics, aquestes interaccions permetrien mesuraments deterministes d'estats de Bell, produint un augment de la velocitat de distribució de l'entrellaçament entre dos nodes remots. Fer que dos fotons interactuïn entre ells de manera eficient requereix mapejar-los en un medi no lineal a nivell d'un sol fotó, és a dir, un medi que reacciona de manera diferent quan interactua amb un sol fotó que quan ho fa amb dos. Una no linealitat tan forta ha estat demostrada amb àtoms de Rydberg, que són àtoms excitats a un estat amb un nombre quàntic principal alt.

En aquesta tesi hem realitzat experiments d'òptica quàntica no lineal emprant conjunts d'àtoms freds de Rydberg, on hem estudiat les propietats de la llum quàntica emesa per aquests àtoms. En primer lloc, vam demostrar no linealitats a nivell d'un sol fotó. Per arribar a aquest estat, vam realitzar diverses millores a la configuració experimental anterior disponible al grup, de les quals va ser especialment rellevant la implementació d'un parany dipolar. La no linealitat quàntica es va evidenciar mesurant el desagrupament dels fotons de la llum transmesa després d'interactuar amb l'estat de Rydberg sota transparència induïda electromagnèticament (TIE). També vam comprovar la generació de fotons individuals sota demanda després d'emmagatzemar estats coherents febles de polsos de llum com excitacions col·lectives de Rydberg.

A continuació vam estudiar la variació de l'estadística de la llum al llarg del pols de sortida després de propagar-se a través del medi com a polaritons de Rydberg, que són estats de superposició de llum i ex-

citacions de Rydberg. Es va demostrar que les propietats al principi i al final del pols eren diferents a les de l'estat estable. En particular, la llum detectada després que el pols d'entrada s'apagués abruptament va donar una supressió molt més gran dels esdeveniments de dos fotons. Tot seguit, vam investigar com aquest efecte podria usar-se per generar fotons individuals sota demanda. Per a fer-ho, vam analitzar la qualitat dels fotons individuals detectats a la fi del pols en funció de la probabilitat de detectar-los i vam comparar els resultats amb els obtinguts emmagatzemant el pols d'entrada com excitacions col·lectives de Rydberg. D'aquesta manera, vam poder comprovar que els fotons es van generar més eficientment quan vam augmentar la finestra de detecció a costa de deteriorar l'estadística dels fotons individuals.

Finalment, vam investigar la indistingibilitat dels fotons emesos pel nostre conjunt atòmic de Rydberg, una propietat crucial per utilitzar àtoms de Rydberg com a nodes de xarxes quàntiques. També vam comparar els fotons individuals generats després de l'emmagatzematge en condicions de TIE amb els obtinguts emprant una excitació Raman de dos fotons a l'estat de Rydberg. La indistingibilitat es va medir fent-los interferir amb estats coherents febles de llum en un experiment de Hong-Ou-Mandel. I vam demostrar que, tot i que vam obtenir millors estadístiques dels fotons en condicions de TIE, l'indistingibilitat dels obtinguts amb excitació Raman resultava significativament més gran.

Resumen

Los fotones son buenos candidatos para transportar información cuántica porque son partículas muy estables: interaccionan débilmente con el medio y apenas entre ellos. Sin embargo, esto presenta inconvenientes cuando se quiere procesar la información porque, en este caso, es preferible tener interacciones fotón-fotón. Por ejemplo, para aplicaciones en repetidores cuánticos, tales interacciones permitirían mediciones deterministas de estados de Bell, aumentando la velocidad de distribución del entrelazamiento entre dos nodos remotos. Hacer que dos fotones interactúen entre sí de manera eficiente requiere mapearlos en un medio no lineal a nivel de un solo fotón, es decir, un medio que reacciona de manera diferente cuando interactúa con un solo fotón que cuando lo hace con dos. Una no linealidad tan fuerte ha sido demostrada con átomos de Rydberg, que son átomos excitados a un estado con un número cuántico principal alto.

En esta tesis hemos realizado experimentos de óptica cuántica no lineal utilizando conjuntos de átomos fríos de Rydberg, donde hemos estudiado las propiedades de la luz cuántica emitida por estos átomos. En primer lugar, demostramos no linealidades a nivel de un solo fotón. Para llegar a este estado, realizamos varias mejoras a la configuración experimental anterior disponible en el grupo, de las cuales fue especialmente relevante la implementación de una trampa dipolar. La no linealidad cuántica se evidenció midiendo un desagrupamiento de los fotones de la luz transmitida después de interactuar con el estado de Rydberg bajo transparencia inducida electromagnéticamente (TIE). También comprobamos la generación de fotones individuales bajo demanda después de almacenar estados coherentes débiles de pulsos de luz como excitaciones colectivas de Rydberg.

A continuación, estudiamos la variación de la estadística de la luz

a lo largo del pulso de salida después de propagarse a través del medio como polaritones de Rydberg, que son estados de superposición de luz y excitaciones de Rydberg. Se demostró que las propiedades al principio y al final del pulso eran diferentes a las del estado estable. En particular, la luz detectada después de que el pulso de entrada se apagara abruptamente dio una supresión mucho mayor de los eventos de dos fotones. Seguidamente, investigamos cómo este efecto podría usarse para generar fotones individuales bajo demanda. Para ello, analizamos la calidad de los fotones individuales detectados al final del pulso en función de la probabilidad de detectarlos y comparamos los resultados con los obtenidos almacenando el pulso de entrada como excitaciones colectivas de Rydberg. Pudimos así comprobar que los fotones se generaron más eficientemente cuando incrementamos la ventana de detección a costa de deteriorar la estadística de los fotones individuales.

Finalmente, investigamos la indistinguibilidad de los fotones emitidos por nuestro conjunto atómico de Rydberg, una propiedad crucial para usar átomos de Rydberg como nodos de redes cuánticas. También comparamos los fotones individuales generados después del almacenamiento en condiciones de TIE con los obtenidos empleando una excitación Raman de dos fotones al estado de Rydberg. La indistinguibilidad se midió haciéndolos interferir con estados coherentes débiles de luz en un experimento de Hong-Ou-Mandel. Y demostramos que, aunque obtuvimos mejores estadísticas de los fotones en condiciones de TIE, la indistinguibilidad de los obtenidos con excitación Raman resultaba significativamente mayor.

A mi madre,

Acknowledgements

I want to start by thanking my thesis supervisor, Hugues de Riedmatten, for giving me this opportunity and not regret it later (I hope). Thank you very much for being so patient and understanding and for always being available to discuss about the experiment. And thanks to the committee members for taking some time to read this work, evaluate it, and provide good feedback. I also want to thank all the people who have worked with me over these years and without whom this would not have been possible. Emanuele, thank you for teaching me practically everything I know about this experiment, for trusting me and taking all my ideas seriously. Thanks to your help, I was able to gain more confidence and overcome (at least a little) the impostor syndrome. David, thank you for introducing me to the experiment, patiently answering my questions, and caring about me. Pau, thank you for your friendship, for helping me with the experiment when Ema left and for all those fruitful discussions in which you always turned out to be right. Jan, thank you for being my support in the last months in the lab and for being our chocolate supply in the office. Klara, thank you for your help, especially with the articles, and for the conversations in the lab.

Many thanks to all the QPSA people, those who left and those who are still here, for being my second family in Barcelona. I feel very lucky to have been part of such a friendly group with such a supportive environment. Thanks to everyone who passed by: Georg, for practicing your Spanish with me, Marguerita, for caring about me, Eliza, Bernardo, Nicolas (please come back!). And thanks to everyone who is still here: Ale, for always making me smile, Lukas, for teaching me more than what I taught you, Samuele, for sharing my party spirit, Darío, Chetan, Jelena, Stefano and those who arrived recently: Edu, Soeren, I hope you enjoy like me. Infinite thanks!

Thanks to the people of ICFO, to my colleagues from the summer fellow who also returned later: Irene, for your advice, Marcos, for the talks on the bus and Sandra, for infecting me with your joy when I needed it most. Thanks to all the ICFO staff for making things easier for me. Special thanks to the staff of the electronics workshop and the mechanical workshop for not rolling their eyes when I said it was urgent, and to the outreach team, especially to Fede, for organizing such beautiful experiences that have made me discover a new passion.

Y finalmente, gracias a toda mi familia, a la que se elige y a la que no. Gracias especialmente a mi madre Ángeles y a mi hermana Trini, por lidiar con mis nervios e inseguridades. Y a mi padre, mis tíos y mis primos, por creer en mi. Gracias a mi novio Jaime, por su apoyo incondicional (sin ti, nada de esto hubiera sido posible) y a toda su familia, por hacerme sentir una más. Gracias a mi amiga Nati, por ser una fuente de inspiración y conocerme más que yo misma y a Seni, por convertirse en uno de mis principales apoyos en Barcelona. Gracias también a mis amigas Geral y Mel. Gracias a todos los que estaban cerca a pesar de la distancia.

Publication list

Publications arising from this work

- Auxiliadora Padrón-Brito, Roberto Tricarico, Pau Farrera, Emanuele Distante, Klara Theophilo, Darrick Chang, and Hugues de Riedmatten. *Transient dynamics of the quantum light retrieved from Rydberg polaritons.* arXiv:2011.12585 [quant-ph] (2020).

- Auxiliadora Padrón-Brito, Jan Lowinski, Pau Farrera, Klara Theophilo, and Hugues de Riedmatten. *Probing the indistinguishability of single photons generated by Rydberg atomic ensembles.* arXiv:2011.06901 [quant-ph] (2020).

Related publications

- Emanuele Distante, Auxiliadora Padrón-Brito, Matteo Cristiani, David Paredes-Barato and Hugues de Riedmatten. *Storage enhanced nonlinearities in a cold atomic Rydberg ensemble.* Phys. Rev. Lett., **117**, 113001, (2016).

- Emanuele Distante, Pau Farrera, Auxiliadora Padrón-Brito, David Paredes-Barato, Georg Heinze, and Hugues de Riedmatten, *Storing single photons emitted by a quantum memory on a highly excited Rydberg state.* Nat. Commun., **8**, 14072, (2017).

Contents

List of Figures

List of Tables

Chapter 1

Introduction

1.1 Quantum information and communication

Quantum information science makes use of quantum mechanical systems to perform information processing and communication tasks. One of the advantages with respect to classical computing is that quantum computing may be able to efficiently solve hard computational problems in classical computing, such as factorization of large numbers [1]. The reason is that conventional computers perform calculations on fundamental pieces of information called bits, which can take the value 0 or 1. Instead, quantum computers use objects called quantum bits, or qubits [2], which can represent both 0 and 1 at the same time due to the superposition principle. Notwithstanding, this threatens the foundation of our current encryption system, which is based on the complexity to factorize large numbers. Fortunately, quantum mechanics also gives us tools to devise a new more secure encryption system [3, 4, 5] in the form of quantum key distribution (QKD), which allows us to transmit a secret key without the risk of undetected eavesdropping [6, 7, 8, 9].

In analogy to the classical information, quantum information can be transmitted between physically separate quantum systems using quantum networks, which are composed of quantum nodes linked by quantum channels [10]. Quantum information is generated, processed, and stored in quantum nodes and transmitted with high fidelity from one node to another through a quantum channel. The best candidates to transmit the information are photons [11] since they are highly-stable particles in the sense that they do not interact with each other and weakly with

the environment. They can be transmitted along moderate distances (of order 100 km) in optical fibers, with an attenuation length of around 22 km at telecommunication wavelengths, which allows the use of existing infrastructure for quantum communication. Moreover, they can be efficiently manipulated using simple devices like mirrors and beamsplitters [1]. However, distributing photons over long distances (of order 1000 km) is an important challenge in quantum communication, since loss and decoherence are significant in this case (the transmission of a 1000 km-long optical fiber is 10^{-20}). In classical communication, we use amplifiers to overcome this problem but, due to the no-cloning theorem [12, 13], this is not possible in the quantum regime. In this case, we can exploit a very important quantum resource: entanglement [14]. Two particles are entangled when it is not possible to describe them individually, i.e. the system state cannot be defined as a product state of particles 1 and 2. Then, the outcomes of measurements performed on entangled particles are correlated, regardless of the distance that separates them. If two distant nodes are entangled, we can use the help of a classical communication channel to transmit quantum information between them, in a process known as quantum teleportation [15]. Two distant nodes can be entangled without the need to physically send an entangled photon the entire distance, using complex devices called quantum repeaters [16, 17, 18, 19, 20].

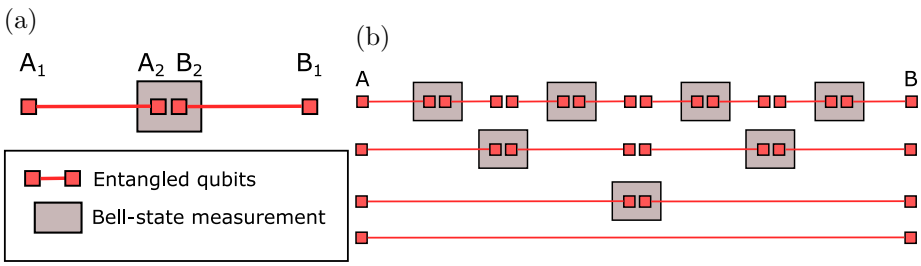

Figure 1.1: Graphical representation of the operation of quantum repeaters.

The operation of a quantum repeater is schematically represented in figure 1.1a. Consider two entangled pairs A_1A_2 and B_2B_1, where A_2 and B_2 are in the same place located midway from A_1 to B_1. A joint measurement of A_2 and B_2 in the Bell-states basis projects the

pair A_1B_1 in an entangled state, even though A_1 and B_1 do not have a common past. This process is known as entanglement swapping [21, 22]. This can be done using linear optics, e.g. using beamsplitters, but the success probability in this case is bounded by 50% per swapping operation [23, 24], limiting the entanglement distribution rate achievable in quantum repeaters. By successive operations over short-distance links, one can share entanglement over two nodes A and B separated by a long distance (see figure 1.1b).

In the quantum nodes, the information processing is carried out by quantum logic gates, which are unitary operations on the qubits [1]. These can act on a single qubit or on multiple ones. The most common two-qubit gate is the controlled-unitary gate, where a unitary operation is applied to a second qubit depending on the state of the first one. It can be shown that this type of two-qubit gate together with single-qubit gates form a universal set of quantum logic gates, so any quantum computation can be expressed in terms of those gates [1]. A two-qubit quantum gate can be used to perform a deterministic (instead of probabilistic) Bell-state measurement [25, 26, 27], thus highly increasing the distribution rate of entanglement in quantum repeater operations [28, 29].

When quantum information is encoded in photons, a two-qubit quantum gate involves a photon-photon interaction. However, as mentioned above, photons do not interact with each other, so this is a major challenge in quantum information processing [10]. Fortunately, photon-photon interactions can be mediated by a medium showing nonlinearity at the single-photon level. Such a strong nonlinearity can be seen in this way: a first photon interacts with the medium and modifies its way of interacting with a second photon (see figure 1.2). Therefore, its response to a light pulse containing a single photon should be very different from its response when the pulse has two or more photons [11]. This is very difficult to achieve since common media typically have a very weak nonlinearity, far from the quantum regime. A strong nonlinearity can be addressed by using a single particle, e.g. an atom, as an interface. A single atom interacts resonantly with no more than a single photon at a time. However, since the interaction probability between a photon and an atom is usually very weak, the atom must be strongly coupled to a high-finesse cavity [30], which involves many technical challenges

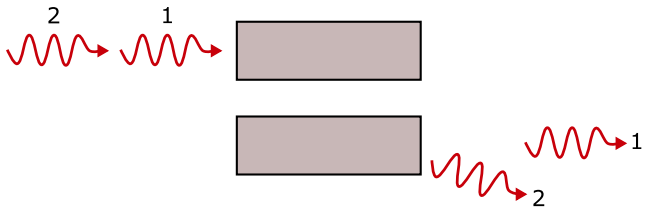

Figure 1.2: Graphical representation of the interaction of a nonlinear medium at the single-photon level with two input photons. The response of the medium to the first photon is different than for the second photon.

[31, 32, 33]. A different approach is to use a large ensemble of atoms instead of just a single one, such as the light-matter interaction depends on the optical depth of the ensemble. Hence, no high-finesse cavity is necessary to ensure strong light-matter interactions. However, in the weak excitation regime, an ensemble of atoms normally does not display strong nonlinearity. Then, the challenge is to make the ensemble of atoms behave as if they were only one. In this case, the atoms would act collectively and a single photon would interact with all of them at the same time [11, 34]. Rydberg atoms, which are atoms excited to a state with a high principal quantum number provide a powerful tool to strongly increase the interactions in the medium [35, 11], enabling us to reach nonlinearities at the single-photon level [36]. Although strong light-matter coupling is normally achieved near an optical resonance, where it is accompanied by absorption, this destructive process can be avoided with electromagnetically induced transparency (EIT). EIT is a coherent optical phenomenon in which a medium, originally opaque due to its resonant interaction with light, becomes transparent over a narrow window within an absorption line [37].

Nonlinear systems at the single-photon level, such as a cloud of Rydberg atoms, can also be exploited to generate single photons on demand. Having photon sources that emit only one photon is extremely important in implementing many of the quantum information protocols [38]. For applications in quantum repeaters, photons must also be indistinguishable so that a Bell-state measurement projects them into a maximally entangled state [22, 39, 40]. Furthermore, since the interfaces used for storage and processing of quantum information transmitted by photons are based on atomic systems, photons must match the spectrum of the atomic transitions, which is usually in the order of MHz [41, 40]. Fi-

nally, photons should be generated on demand. On-demand sources emit a single photon in a specific time interval after a trigger signal. This is important to be able to synchronize multiple sources. Therefore, single-photon sources must meet many requirements: they must not only be fast and efficient, but they must generate pure, indistinguishable, and narrow-bandwidth photons on demand. On-demand single-photon sources can be implemented from a variety of systems, including single emitters, such as single atoms, ions or molecules [42, 43, 44, 45, 46]; solid-state systems [47, 48, 49] or ensembles of atoms, such as Rydberg atoms [50, 51].

1.2 Rydberg atoms for quantum information

Nonlinearity in Rydberg atoms normally occurs with a phenomenon called dipole blockade. Highly excited Rydberg atoms show strong long-range dipole-dipole interactions [52], which shift the energy required to excite multiple atoms to a Rydberg state. In this way, only one photon from a resonant input field will be able to excite an atom to the Rydberg state. A second photon, however, will not be on resonance with the transition. This results in a nonlinear response of the medium at the single-photon level, which is a key ingredient for applications in quantum information, as explained in the previous section. Since the interaction between two Rydberg atoms depends on their relative distance, there is a maximum distance at which dipole blockade occurs, which is called the blockade radius [52].

The use of electromagnetically induced transparency (EIT) with Rydberg atoms [53] provides an efficient way to map photons onto Rydberg states, therefore enabling photon-photon interactions. EIT can render an opaque medium transparent within a narrow window around resonance employing a two-photon transition controlled by a coupling field. Photons within this transparency window propagate through the medium as quasiparticles called dark-state polaritons (DSP) with a velocity much lower than the one of light in vacuum [54, 55]. Besides, it is possible to control the velocity of the DSP by controlling the intensity of the coupling field, even decreasing it to zero, which enables the storage of information in the medium. When we use EIT to excite atoms to Rydberg states, the dipole blockade prevents more than one

atom from being excited within the blockaded region. Therefore, only one photon within this region can propagate through the medium. A second photon cannot interact with the medium under EIT conditions and therefore sees it opaque. The probability that a second photon can also be transmitted depends on the optical depth within the blockaded region. Therefore, this is an important parameter in the nonlinearity of the system. The phenomenon of dipole blockade and EIT will be explained in more detail in Chapter 2.

Rydberg atomic ensembles have been used to mediate interactions between photons in quite a lot of experiments in the last years [11, 56, 57]. The first demonstration of strong nonlinearities in the output light under Rydberg EIT conditions was made by Pritchard et al. in 2010 [58]. A nonlinearity at the single-photon level was demonstrated in a similar system two years later by Peyronel et al. [36]. At the same time, other experiments also demonstrated nonlinearity at the single-photon level: Dudin and Kuzmich generated single photons by using off-resonant (Raman) excitation to a Rydberg state [59] and Maxwell et al. achieved it by storing and retrieving under EIT conditions [60]. These last two experiments constitute the first realization of a single-photon source based on Rydberg atoms. Dispersive nonlinearities at the single-photon level have also been demonstrated, showing exotic states of light as a two-photon bound state [61], three-photon bound state [62] and repulsive photons [63]. The first demonstration of a single-photon source using Rydberg atoms in a room-temperature vapor was made by Ripka et al. in 2018 [51]. In general, Rydberg atoms have been proposed and used so far to generate single photons in a quasi-deterministic fashion [64, 65, 50], contrary to ground state ensembles which usually rely on probabilistic or heralded schemes [39]. A photon-photon interaction mediated by Rydberg atoms located in two different atomic ensembles was demonstrated by Busche et al. in 2017 [66].

There are many proposals to exploit Rydberg interactions for quantum information processing applications [57]. Some examples are photon-photon gates [67, 68, 69, 70], optical switches and transistors [71], building blocks for quantum repeaters [72, 73], among others. The first single-photon switch and transistor were demonstrated in 2014 [74, 75, 76], followed by some improvements [77, 78, 79]. The first experimental demonstration of a photon phase gate with a π phase shift based on Ry-

dberg EIT was reported in 2019 [80]. Other experimental applications exploit the strong interactions of Rydberg atoms to manipulate and generate quantum states in a quasi-deterministic way. Some examples are: a quantum memory loaded with one single atomic excitation [81], entanglement between light and atomic excitation [82, 28] and manipulation of two collective atomic excitations [64]. Furthermore, some experiments have shown building blocks for quantum repeaters applications [83].

Another approach is to use the strong interaction between two individual Rydberg atoms to manipulate quantum information stored in atoms [84, 85, 86, 87] with a high fidelity [88, 89, 90]. In this way, the first quantum gate was demonstrated by Isenhower in 2010 [91] and several have come later [92, 93]. Other applications as entanglement generation [94, 95, 89] and quantum simulation [96, 97, 98, 99, 100] have been demonstrated.

1.3 Motivation and contents of the thesis

The general goal of this thesis is to experimentally study the properties of an ensemble of Rydberg atoms for applications in quantum non-linear optics, quantum information and computation. As a starting point, we already had a cloud of cold atoms, a laser system to prepare and excite them to Rydberg states in a controlled way, and a system to detect and analyze the output photons [101].

The ambitious long-term goal of this project is the implementation of building blocks for applications in quantum repeaters. The idea is to exploit the strong nonlinearities of Rydberg atoms to build a two-qubit quantum gate. This will allow deterministic Bell-state measurements, increasing the entanglement distribution rate. To this end, we realized an experiment in 2017 in which we connected our Rydberg cloud of atoms to an existing DLCZ quantum memory in our laboratory [83]. In this experiment, we stored a true single photon as a Rydberg collective excitation and observed that the non-classical correlations of the single photon persisted after retrieval from the cloud. However, the nonlinearity in the ensemble of Rydberg atoms was far from the single-photon level, which is an essential element for building a two-qubit gate, as we have already mentioned. Therefore, the first objective of this thesis has

been to increase the nonlinearity of the medium to the single-photon level and, also, the efficiency of the light-matter coupling. The process carried out and the characterization of the nonlinearity in each step is explained in Chapter 3.

After achieving nonlinearity at the single-photon level, we have conducted two experiments to study the properties of the quantum light generated in our cloud of atoms. In the first one, we have studied the propagation of weak coherent pulses of light in an ensemble of Rydberg atoms under EIT conditions. In particular, we have observed that the quantum statistics of the transmitted light strongly varies during the transients parts of the pulse. Although the transmission of continuous-wave (CW) weak-coherent states of light has been investigated before [36], the use of CW light makes challenging the efficient creation of single photons localized in time, i.e. on-demand [102]. It has been shown that single localized photons can be created by using an off-resonant excitation to Rydberg states [59, 81, 64] or by storing single photons through EIT [60, 103]. However, this represents an additional experimental complexity and source of inefficiency. The use of the transients of transmitted pulses (without storage) in Rydberg EIT may therefore lead to the generation of localized single photons with higher efficiencies. This study is shown in Chapter 4.

In the second experiment, we have studied the indistinguishability of single photons generated in the Rydberg ensemble. As mentioned before, probing indistinguishability is important for the implementation of quantum networks using collective Rydberg excitation as quantum nodes, where a crucial next step is to generate entanglement between remote nodes. So far, only a few experiments have probed the indistinguishability of single photons emitted by Rydberg ensembles [50, 104, 82], but most of the experiments considered only a small part of the single-photon pulse. Moreover, all experiments realized so far used single photons generated by off-resonant excitation to Rydberg states. In our study, we have realized a Hong-Ou-Mandel experiment, where the single photons interfere with a weak coherent state of light, demonstrating a good overlap between them. Furthermore, we have compared the overlap obtained using photons generated by off-resonant excitation with those generated by EIT. The results of this study are shown in Chapter 5.

Chapter 2

Quantum optics with Rydberg atoms

In this chapter, we will make a summary of the fundamental theoretical concepts necessary to understand this thesis work. We will start introducing the general properties of Rydberg atoms, especially the dipole-dipole interactions, which convert them in interesting systems for quantum information applications. In this work, Rydberg atoms are mainly used as a single-photon source. Therefore, we will continue by introducing two important figures of merits of single-photons quality: the second-order correlation function and the indistinguishability. After this, we will describe two techniques which can be used to generate high-quality single photons from ensembles of Rydberg atoms: the electromagnetically-induced transparency, more oriented for using Rydberg atoms to engineer photon-photon interactions, and the off-resonant excitation technique. Finally, we will discuss the processes involved in the decoherence and dephasing of Rydberg atoms.

2.1 Rydberg atoms

A fairly complete and detailed reading of the application of Rydberg atoms in the field of quantum information can be found in the review by Saffman et al (2010) [52] and the more recent reviews by Murray et al. (2016) [105] and Adams et al. (2019) [57]. The writing of this section has been based primarily on these reviews.

Atoms with a valence electron in a highly-excited state are called

Rydberg atoms [35, 52, 57]. The energy of these states can be calculated with a simple Bohr model, where a valence electron is bound to a positive-charged nucleus by the Coulomb force.

$$E_{nlj} = -\frac{Ry}{n^2} \tag{2.1}$$

where n is the principal quantum number and Ry is the Rydberg constant. This model works well for alkali atoms, where internal electrons form closed shells, and for states with a high orbital momentum quantum number l. However, for states with low l, it is possible to find the valence electron near the nucleus and, therefore, interaction with internal electrons needs to be taken into account. This is done by introducing the so-called quantum defect δ_l, so that the effective principal quantum number is $n^* = n - \delta_l$ [52, 57].

The interaction between Rydberg atoms can be 12 orders of magnitude larger than the interaction between ground state atoms [52]. This arises from the scaling of their properties with n (see table 2.1), which allows to control the strength of the interaction by changing n. Especially important is the dipole moment between adjacent states, which scales with n^2 and can become huge for large n, allowing the interactions to be significant even at long distances of the order of 10 μm. Moreover, Rydberg atoms are metastable with lifetimes going from tens to hundreds of μs [52], which together with the strong and controllable interactions make them attractive candidates for applications in quantum technologies [52, 105, 57].

Property	Scaling
Binding energy	n^{-2}
Energy spacing	n^{-3}
Orbital radius	n^2
Polarizability	n^7
Transition dipole moment from ground state	$n^{-3/2}$
Transition dipole moment between adjacent states	n^2
Radiative lifetime	n^3

Table 2.1: Scaling of the properties of Rydberg atoms with n.

2.1.1 Dipole-dipole interactions

The dipole-dipole interaction between two alkali atoms separated by a distance long enough to neglect spatial overlap is schematically represented in figure 2.1 and described by the potential operator

$$V_{dd} = \frac{1}{4\pi\epsilon_0 R^3}\left(\vec{\mu_1}\cdot\vec{\mu_2} - 3\left(\vec{\mu_1}\cdot\hat{R}\right)\left(\vec{\mu_2}\cdot\hat{R}\right)\right), \tag{2.2}$$

where $\vec{\mu}_{1(2)}$ is the dipole transition operator associated with each atom $\vec{\mu}_{1(2)} = e\vec{r}_{1(2)}$, R is the relative distance between atoms and $\hat{R}$ the unitary vector in this direction [52, 106].

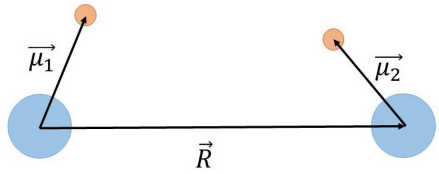

Figure 2.1: Simple schema of two one-electron atoms. Blue circles are representation of atomic nuclei and orange ones are electrons. This is a valid representation for alkali atoms.

One may think that dipole-dipole interactions are only possible if both atoms have permanent dipole moments, such that the interaction can be pictured out as in figure 2.1. However, one can observe non-negligible effects due to dipole-dipole interactions, even if the individual atoms are presumably in a non-degenerate state, where $\langle n, l, j|\vec{\mu}|n, l, j\rangle = 0$. These effects become apparent when we treat the system in the two-atom state basis. To simplify this problem, we consider the case where only one state $|r', r''\rangle$ contributes to the interaction (see figure 2.2). We can see that, although the diagonal elements of V_{dd} are zero $\langle r, r|V_{dd}|r, r\rangle = \langle r', r''|V_{dd}|r', r''\rangle = 0$, the off-diagonal elements $\langle r', r''|V_{dd}|r, r\rangle$ are different from zero, as long as $|r\rangle$ is dipole-coupled with $|r'\rangle$ and $|r''\rangle$ (see figure 2.2c). Therefore, if the potential energy of the interaction is comparable to the energy defect $\delta = E_{|r,r\rangle} - E_{|r',r''\rangle} = 2E_{|r\rangle} - E_{|r'\rangle} - E_{|r''\rangle}$ (fig. 2.2b), the system should be described in a superposition of both states $|r, r\rangle$ and $|r', r''\rangle$, hence it is no longer separable. That is, we cannot describe it as a product of the individual atomic states and its associated energy is different from the sum of the

individual atomic energies. A clear explanation can be found in the review by Browaeys and Lahaye (2016) [107].

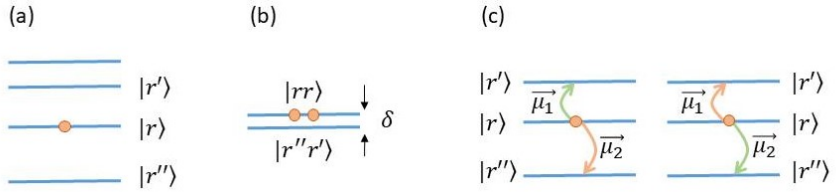

Figure 2.2: (a) Level structure representation in the one-atom basis, (b) level structure in the two-atom basis. δ is the energy separation between both levels [108]. (c) Schematic representation of dipole-dipole interaction in Rydberg atoms. The dipole transition moment $\vec{\mu_1}$ of an atom interact with $\vec{\mu_2}$ of another atom.

The eigenenergies and eigenstates of the system can be calculated by solving the Schrödinger equation $H|\psi\rangle = E|\psi\rangle$ where the interacting Hamiltonian in the basis $\{|r,r\rangle, |r',r''\rangle\}$ is

$$\begin{pmatrix} \delta & \langle r,r|V_{dd}|r',r''\rangle \\ \langle r',r''|V_{dd}|r,r\rangle & 0 \end{pmatrix}. \tag{2.3}$$

It can be shown that the solutions depend on the interatomic distance R. For $R \to \infty$, the interaction potential vanishes and the eigenstates tend to the separable ones, with eigenenergies $E_{|r,r\rangle}$ for $|r,r\rangle$ and $E_{|r',r''\rangle}$ for $|r',r''\rangle$. For smaller R, the eigenenergies are shifted due to the interaction. For the $|r,r\rangle$ state, this energy shift is [52]

$$\Delta_{r,r}(R) = \frac{\delta}{2} - sign(\delta)\sqrt{\frac{\delta^2}{4} + \frac{C_3^2}{R^6}D_{r,r}}, \tag{2.4}$$

where $D_{r,r}$ is the van der Waals eigenvalues, which account for the angular part of the interaction and usually lies between 0 and 1 and $C_3 = e^2 \langle r'|\hat{r}|r\rangle \langle r''|\hat{r}|r\rangle$, where $\hat{r}$ is the position operator. Note that, since the transition dipole moment between adjacent states scales with n^2 (see table 2.1), C_3 scales with n^4. From the above equation, we can find two different regimes:

- For $\delta < \langle r',r''|V_{dd}|r,r\rangle$, which happens for small interatomic distances: The potential is able to couple $|r,r\rangle$ and $|r',r''\rangle$. This can

be seen as if the atoms were continuously going from one state to another dipole-coupled one, exchanging virtual photons in the process. This is called a dipole-dipole type interaction, because the interaction occurs at the first order of the perturbation theory [109]. The energy shift in this limit is $\Delta_{r,r} \sim -sgn(\delta)C_3\sqrt{D_{r,r}}/R^3$, which increases with n^4.

- For $\delta > \langle r', r''|V_{dd}|r, r\rangle$, which happens for longer interatomic distances: The energy potential is not able to couple the two states and dipole-dipole interaction appears in the second-order of the perturbation theory [109]. This can be seen as a two virtual-photon process, in contrast to the single virtual-photon process for small δ. This interaction produces an energy shift $\Delta_{r,r} \simeq C_6/R^6 \propto C_3^2/(\delta R^6)$, which increases with n^{11} ($C_3 \propto n^4$ and $\delta \propto n^{-3}$ from table 2.1) and is called a Van der Waals-type interaction.

The distance that marks the transition from the dipole-dipole to Van der Waals interaction is called the critical distance R_c and is defined from $\delta = C_3\sqrt{D_{r,r}}/R_c^3$. Note that if $\delta = 0$, $R_c = \infty$ and we can excite the atoms to the degenerate state no matter how far they are, leading to a so-called Förster resonance.

As we said before, the angular part, included in the term $D_{r,r}$, also plays a role in the interaction. Working with spherically symmetric S orbitals as Rydberg states has the advantage of having almost spherically symmetric interactions. Another advantage is that the energy defect is negative and hence, the interaction is repulsive, which prevents Rydberg-Rydberg collisions creating dephasing.

2.1.2 Dipole blockade

An important effect arising from the strong interactions between Rydberg atoms is the dipole blockade [84, 85]. It prevents the Rydberg excitation of two atoms if they are closer than a distance called the blockade radius r_b. It occurs because, at this distance, the energy shift Δ_{rr} is greater than the excitation linewidth. For Van der Waals-type interactions where the excitation linewidth is limited by the linewidth of the laser field $\hbar\Omega$, r_b is defined as

$$r_b = \sqrt[6]{\frac{C_6}{\hbar\Omega}}, \tag{2.5}$$

what gives that $r_b \propto n^{11/6}$, since $C^6 \propto n^{11}$. Usual experimental conditions gives a blockade radius of the order $\sim 10\ \mu m$. A schematic representation of the Rydberg blockade is shown in figure 2.3a.

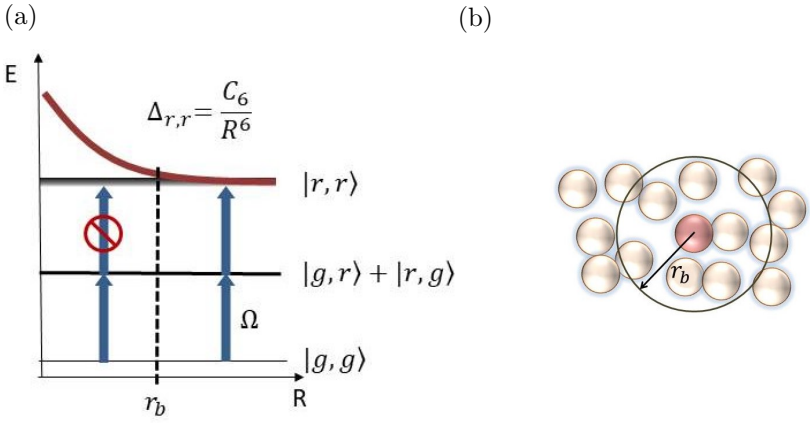

Figure 2.3: (a) Level scheme of the double excitation. For interatomic distances closer than r_b, the blockade prevents the excitation of both atoms to the Rydberg state. (b) Schematic representation of a blockade sphere. A single Rydberg excitation is shared among all the atoms inside this volume.

This can be generalized for atomic ensembles with a number of atoms $N \gg 2$. For atoms confined within a volume smaller than r_b^3, dipole blockade ensures that no more than a single Rydberg excitation can be created. Hence, the system is driven from the state $|G\rangle = |g_1, g_2, ..., g_N\rangle$, where all the atoms are in the ground state, to the collectively excited state $|R\rangle$, which is called a Rydberg spin-wave, defined by

$$|R\rangle = \frac{1}{\sqrt{N}} \sum_{j=1}^{N} |g_1, ..., r_j, ..., g_N\rangle \tag{2.6}$$

This means that the entire medium acts as a two-level system, often called a superatom. Due to the collective behavior of the atoms, the

Rabi frequency is enhanced to $\sqrt{N}\Omega$.

For larger atomic clouds, dipole blockade results in spatial correlations between Rydberg excitations within the cloud, since the distance between them should be greater than r_b. Due to finite cloud extension, dipole blockade set a maximum number of Rydberg excitations that can be present in the cloud. In this case, each excitation is enhanced by the number of atoms inside a blockade sphere, defined by the blockade radius (see figure 2.3b).

For applications in quantum processing, the dipole blockade, or generally the strong interaction of a Rydberg pair, can be exploited to engineer photon-photon interactions and single-photon sources. In order to characterize the photons generated from a Rydberg ensemble, two important figure of merits are the second-order correlation function and the indistinguishability.

2.2 Statistics of quantum light

This section is inspired by the book of Mark Fox [38].

The second-order correlation function gives the temporal coherence of the light and is defined as

$$g^{(2)}(t,\tau) = \frac{\left\langle a^\dagger(t)a^\dagger(t+\tau)a(t+\tau)a(t)\right\rangle}{\left\langle a^\dagger a\right\rangle^2} \tag{2.7}$$

where $a^\dagger(t)(a(t))$ is the creation (annihilation) operator for the transmitted light mode at time t. The second-order correlation function usually does not depend on t so $g^{(2)}(t,\tau)$ is simply written as $g^{(2)}(\tau)$. There are three types of light statistics, depending on the value of $g^{(2)}(0)$ (see figure 2.4):

- Bunched light: $g^{(2)}(0) > 1$. This means that the probability of detecting two photons separated by a short τ is higher than for a longer τ. In a stream of photons, they are all clumped together in bunches. It is the case of thermal light.
- Coherent light: $g^{(2)}(0) = 1$. The probability of finding two photons for $\tau = 0$ is the same as for larger values of τ. It correspond to a

stream of photons with completely random time intervals between them.

- Antibunched light: $g^{(2)}(0) < 1$. The probability of finding two photons at short τ is lower than the probability when $\tau \to \infty$. Then, it consists of a stream of photons with a minimum time interval between them.

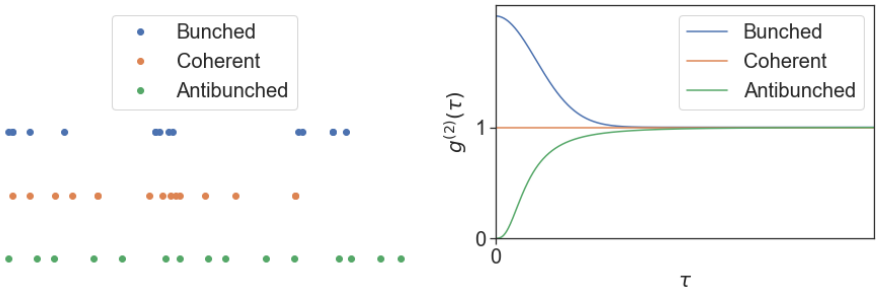

Figure 2.4: In the left, simple representation of three photon streams with the different type of statistics. In the right, the corresponding second-order correlation function feature.

It can be shown that the classical theory of light satisfies

$$g^{(2)}(0) \geq 1 \tag{2.8}$$

and

$$g^{(2)}(0) \geq g^{(2)}(\tau) \tag{2.9}$$

Then, the observation of photon antibunching is a purely quantum effect with no classical counterpart [38]. For a photon number state $|n\rangle$, the second-order correlation function at zero-delay time is $g^{(2)}(0) = (n-1)/n$. As a consequence, for single-photon states ($|1\rangle$), it gives $g^{(2)}(0) = 0$. The first demonstration of photon antibunching was made by Kimble et al. using the light emitted by sodium atoms [110].

The second-order correlation function can be obtained with a Hanbury-Brown and Twiss experiment [111, 112, 113], where the input photons go through a 50:50 beamsplitter (BS) and are detected by two single-photon avalanche detectors (SPD), as shown in figure 2.5. The arrival times of the photons in each detector are recorded so we can measure

the number of coincidences when there is a click event in SPD_1 at time t and a click in SPD_2 at time $t+\tau$. Finally, the second-order correlation function is obtained by normalizing the number of coincidences by the expected one in the uncorrelated case. That is

$$g^{(2)}(t,\tau) = \frac{\langle n_1(t) n_2(t+\tau)\rangle}{\langle n_1(t)\rangle \langle n_2(t+\tau)\rangle}, \tag{2.10}$$

where $n_{1(2)}(t)$ is the number of photons registered by the first(second) detector at time t. The symbol $\langle ...\rangle$ indicates the average value found after many repetitions of the experiment [38].

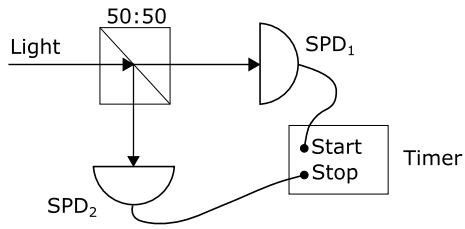

Figure 2.5: Simple setup representation of HBT experiment.

As we said before, $g^{(2)}(t,\tau)$ usually does not depend on t and a click in the first detector can be used to define the start ($t = 0$). Then, a histogram with the number of coincidences as a function of the delay time τ can be produced. In figure 2.6, we show two kinds of histograms obtained in a Hanbury-Brown and Twiss experiment, for the case of antibunched light. In the left, we show the case of a continuous beam of light with photons separated by a minimum time interval of average t_p. In this case, the probability to detect two photons at the same time should be zero, hence $g^{(2)}(0) = 0$ and the time-width of the antibunching dip is related to t_p. Therefore, we can say that the source generating such a light beam is a source of single photons. However, they are delocalized inside the light beam, in the sense that we cannot know at which time we will detect a photon, we only know that they should be separated by a time $\sim t_p$.

As discussed in the introduction, for applications in quantum information and quantum computing, we need a source able to emit a single photon in response to a trigger pulse. In the right of figure 2.6, we show a simple representation of this case. The time separation between trig-

ger pulses (represented as vertical lines) will be denoted by $t_{trigger}$ and the averaged time needed for the source to emit a single photon after a trigger pulse by t_{em}. If $t_{trigger} > t_{em}$, the emission is then controlled by the trigger pulse and the single-photon generation time is known. The histogram of the number of coincidences detected by a Hanbury-Brown and Twiss experiment will show no coincidences around $\tau = 0$, which means that the probability to detect two photons generated by the same pulse is zero, what gives $g^{(2)}(0) = 0$. A bunch of coincidences around $\tau = m \cdot t_{trigger}$ should be detected, where m is an integer, corresponding to coincidences between two photons generated in different trigger pulses.

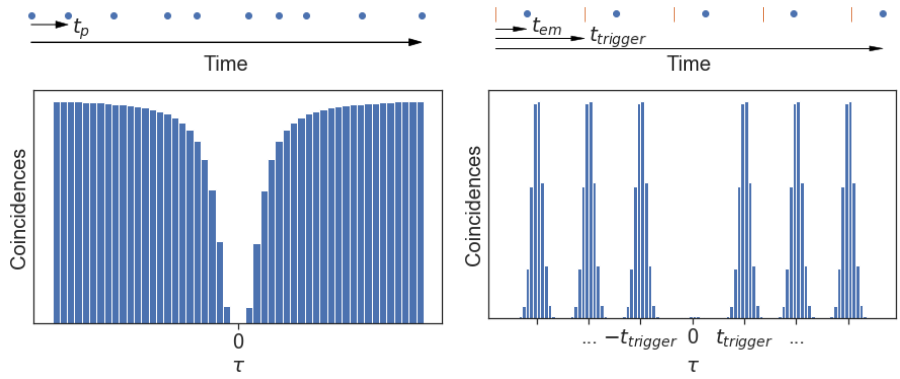

Figure 2.6: Simple representation of two single-photon sources with the corresponding coincidences histogram feature. In the left, photons are delocalized inside a light beam. In the right, they are localized after a trigger pulse.

2.3 Photon indistinguishability

The indistinguishability of two photons can be tested by means of the Hong-Ou-Mandel (HOM) effect [114]. This is a two-photon interference effect, which occurs when two identical photons impinge on a 50:50 beamsplitter, one per input mode. The four output possibilities are represented in figure 2.7. Since a photon has 50% of probability of being reflected or transmitted, both photons could in principle leave the beamsplitter in the same output port (first and fourth cases of figure) or in

different ports (second and third cases). If the photons are identical, i.e. same polarization, spatio-temporal mode and frequency, there is a destructive interference between the second and third possibilities and they cancel each other. Hence, photons can only leave the beamsplitter in the same output mode.

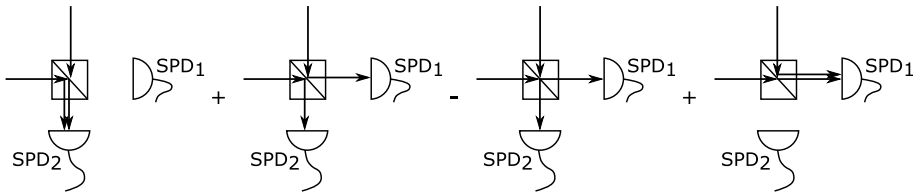

Figure 2.7: Representation of the HOM effect. Each plot represent an output possibility. The sum and minus sign come from the relative phase between terms for the case of identical photons.

This effect can be mathematically described from the transformation relation of the beamsplitter. If the input optical modes are characterized by the annihilation (creation) operators $a(a^\dagger)$ and $b(b^\dagger)$, the output modes $c(c^\dagger)$ and $d(d^\dagger)$ can be obtained from

$$\begin{pmatrix} a \\ b \end{pmatrix} \rightarrow \frac{1}{\sqrt{2}} \begin{pmatrix} 1 & 1 \\ 1 & -1 \end{pmatrix} \begin{pmatrix} c \\ d \end{pmatrix}, \tag{2.11}$$

where the -1 can be physically interpreted as the reflection from one surface of the beamsplitter inducing a relative phase shift of π with respect to the reflection from the other side.

Therefore, if two identical photons enter the beamsplitter, one on each side, the double-mode state becomes $|1,1\rangle_{ab} = a^\dagger b^\dagger |0,0\rangle_{ab}$ which gives

$$\begin{aligned} \frac{1}{2}\left(c^\dagger + d^\dagger\right)\left(c^\dagger - d^\dagger\right)|0,0\rangle_{cd} &= \frac{1}{2}\left(c^{\dagger 2} - d^{\dagger 2}\right)|0,0\rangle_{cd} \\ &= \frac{|2,0\rangle_{cd} - |0,2\rangle_{cd}}{\sqrt{2}}, \end{aligned} \tag{2.12}$$

obtaining that both photons exit the beamsplitter in the same output mode.

The HOM effect is observed by measuring the photon events arriving to the photodetectors placed after the two beamsplitter output ports (see figure 2.7). The probability to record a coincidence is zero when the two input photons are perfectly indistinguishable. In the non-ideal case, the degree of indistinguishability between photons can be obtained by comparing the probability to have a coincidence when they are sent in the same mode p_{indis} with the probability when the two photons are sent in different modes p_{dis} (for example, by sending them in different times). The HOM visibility $V = (p_{dis} - p_{indis})/p_{dis}$ gives the information about how indistinguishable the two photons are, which is directly related with the purity of single photons [48].

Since this effect relies on the existence of photons, it can not be fully explained by classical optics. When two coherent states interfere at the beamsplitter, the maximum visibility which can be obtained under normal conditions is 1/2 [115]. As a consequence, a visibility higher than 0.5 is a proof that the interference happens in the quantum regime.

2.4 Electromagnetically-induced transparency

This section is primarily based on the review of Fleischhauer et al. (2005) [37].

Strong coupling between light and an ensemble of atoms is typically found when light interacts resonantly with the medium, what is usually accompanied by strong absorption and dispersion. However, the electromagnetically induced transparency (EIT) technique allows a coherent light-matter coupling (without loosing photons) [37], what makes it ideal for using Rydberg atoms as a quantum interface for photons.

In a ladder-type three-level system, EIT appears when a weak *probe* beam couples the ground state $|g\rangle$ to an intermediate excited state $|e\rangle$ and a strong *coupling* beam couples $|e\rangle$ to a metastable state $|r\rangle$ (see figure 2.8a). Let us consider first the case where Rydberg interactions are either negligible or nonexistent. For example, when $|r\rangle$ is a low-lying Rydberg state with the blockade radius smaller than the average interatomic distance. In the absence of the coupling beam, the probe field interacts with the two-level system $\{|g\rangle, |e\rangle\}$. If the probe field is sent on resonance with the $|g\rangle \rightarrow |e\rangle$ transition, it is absorbed and

rapidly scattered due to spontaneous emission from the state $|e\rangle$ with a rate Γ_{eg}. When the coupling beam is applied, quantum interference appears, leaving the medium transparent to the probe. This effect can be qualitatively described taking into account that $\Omega_c \gg \Omega_p$, where Ω_c and Ω_p are the Rabi frequencies of the coupling and probe field, respectively, defined as $\Omega = \vec{\mu}\vec{E_0}/\hbar$, where $\vec{\mu}$ is the transition dipole moment and $\vec{E_0}$ the electric field amplitude. If the beams are sent in resonance with the two-photon transition $|g\rangle \rightarrow |r\rangle$, the two possible pathways in which probe light can be absorbed ($|g\rangle \rightarrow |e\rangle$ and $|g\rangle \rightarrow |e\rangle \rightarrow |r\rangle \rightarrow |e\rangle$) interfere and cancel each other. The atoms are driven to a so-called dark state, which is a superposition state of $|g\rangle$ and $|r\rangle$ in the dressed-state picture [37]. As a consequence, atoms cannot be promoted to $|e\rangle$, leading to a vanishing light absorption within a very narrow transparency frequency window.

The response of the medium can be quantitatively described using a semiclassical analysis. From the atomic master equation, we obtain the following expression for the susceptibility [56]:

$$\chi^{(1)} = \frac{\mathrm{OD}\gamma_{eg}}{k_p L} \cdot \frac{i\gamma_{rg} + 2\delta}{(\gamma_{eg} - 2i\Delta)(\gamma_{rg} - 2i\delta) + \Omega_c^2}, \tag{2.13}$$

where γ_{eg} and γ_{rg} are the rates of decoherence, including spontaneous emission and dephasing processes from $|e\rangle$ and $|r\rangle$, respectively, $\Delta = \omega_p - \omega_{ge}$ and $\delta = (\omega_p + \omega_c) - \omega_{gr}$ are the single and double-photon detunings, where ω_p is the probe field frequency, ω_c is coupling field frequency and ω_{gr} and ω_{ge} are the transitions frequencies. The normalization factor is written in terms of the optical depth of the medium to the probe beam, which can be obtained from the transmission in the absence of the coupling beam as $T = e^{-\mathrm{OD}}$. Then, $k_p = 2\pi/\lambda_p$ is the probe wavevector and L is the medium length. The feature of the real and imaginary part of the susceptibility is represented in figure 2.8b, in the presence (blue line) and absence (orange line) of the coupling field.

The imaginary part of the susceptibility governs absorption happening in the medium, so that the transmission under EIT conditions (when the coupling beam is applied) can be obtained as $T = e^{-k_p \cdot L \cdot \mathrm{Im}[\chi^{(1)}]}$. The transmission at the two-photon and single-photon resonances ($\delta = \Delta = 0$) is

$$T_{EIT} = exp\left(-OD\frac{\gamma_{eg}\gamma_{rg}}{|\Omega_c|^2 + \gamma_{eg}\gamma_{rg}}\right). \tag{2.14}$$

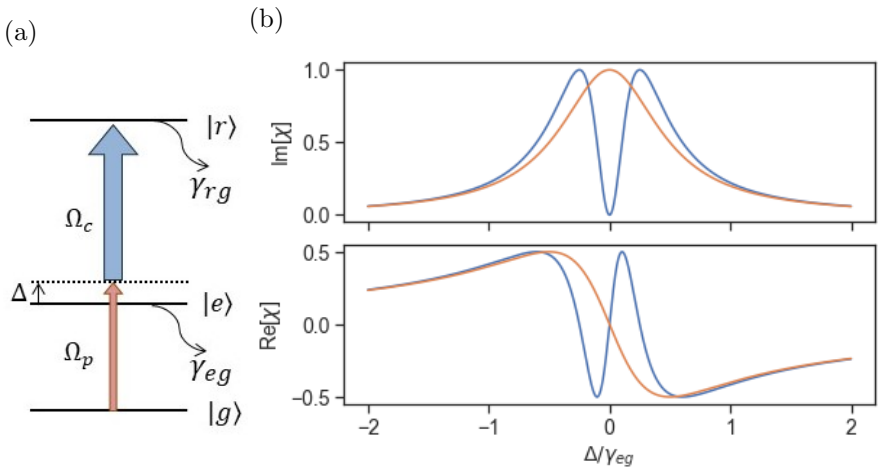

Figure 2.8: (a) Level structure of a ladder-type three-level system interacting with probe and coupling fields. The probe detuning from $|g\rangle \rightarrow |e\rangle$ transition is represented by Δ, while the two-photon transition $|g\rangle \rightarrow |r\rangle$ is on resonance. Decoherence rates from states $|r\rangle$ and $|e\rangle$ are represented by γ_{rg} and γ_{eg}, respectively. (b) Linear susceptibility as a function of probe detuning Δ (in units of γ_{eg}): top, $\mathrm{Im}[\chi^{(1)}]$, related to absorption; bottom, $\mathrm{Re}[\chi^{(1)}]$ determines the refractive index. For the plot: $\gamma_{rg} = 0$ and $\Omega_c = 0.5\gamma_{eg}$. Note that for $\gamma_{rg} \neq 0$, $\mathrm{Im}[\chi^{(1)}] \neq 0$ for $\Delta = 0$ and therefore the transmission within the EIT window is not perfect.

Around resonance, it is a Gaussian with width

$$\Delta_{EIT} = \frac{\Omega_c^2}{\sqrt{\Gamma_{eg}\gamma_{eg}}} \frac{1}{\sqrt{OD}}, \tag{2.15}$$

where Γ_{eg} is the total spontaneous emission rate out of state $|e\rangle$, as defined before.

The real part of the susceptibility is related to dispersion and determines the refractive index of the medium as $n = \sqrt{1 + \mathrm{Re}[\chi^{(1)}]}$. Then, a probe pulse traveling through the medium experiences a change in its group velocity compared to that in vacuum c. The group velocity as a

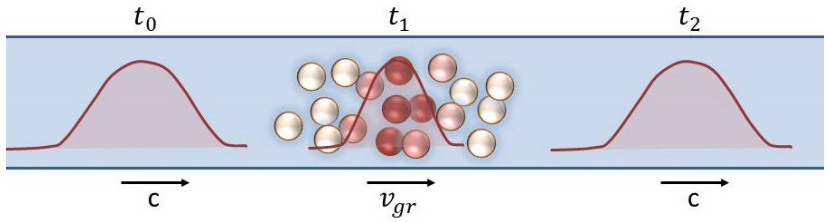

Figure 2.9: Graphical representation of the propagation of a probe pulse under EIT conditions. The pulse travels through the medium as a polariton, which is a coupled state of light and atomic excitation. The reduced group velocity leads to a spatial compression of the pulse during propagation.

function of the refractive index is:

$$v_{gr} = \frac{c}{n + \omega_p \frac{dn}{d\omega_p}}. \tag{2.16}$$

Since the slope of n in the regime of transparency is positive and steep (see figure 2.8b), the resulting group velocity of the probe pulse is strongly reduced $v_{gr} \ll c$ [116] (however phase velocity is c). This phenomenon is called *slow-light* [116]. The group velocity at resonance ($\delta = \Delta = 0$) as a function of experiment parameters is

$$v_{gr} = \frac{c}{n_{gr}}; \quad n_{gr} = 1 + \frac{OD \cdot c}{L} \frac{\Gamma_{eg}}{\Omega_c^2 + \gamma_{eg}\gamma_{rg}}. \tag{2.17}$$

This effect leads to a spatial compression of the probe pulse when it propagates through the medium (see figure 2.9). The propagation can be described in a mathematical formalism employing a quasiparticle known as *dark-state polariton* (DSP) [55], which is a coherent superposition of electromagnetic and atomic excitations.

Since v_{gr} depends on Ω_c in the way that decreasing Ω_c leads to lower v_{gr} (see equation 2.17), it is possible to reduce the group velocity to zero by switching off the coupling beam. This process is known as *light storage* [117, 54, 118, 119]. Reducing v_{gr} to zero also changes the character of the polariton to a pure excitation (see figure 2.10). By increasing Ω_c back to its initial value, the probe pulse can be retrieved from the medium. Then, the time after which the pulse leaves the medium is not only dependent on the group velocity v_{gr} (as in *slow light*), but on the

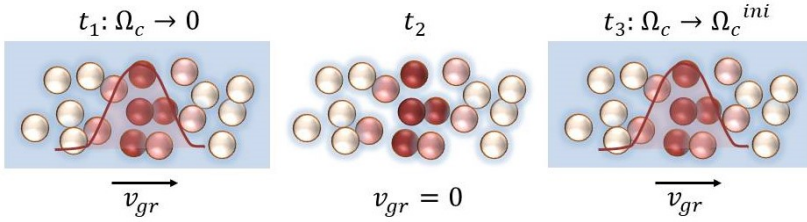

Figure 2.10: Graphical representation of the storage of a probe pulse under EIT conditions. When the pulse is traveling through the medium as a polariton, the control field is switched off (t_1). This leads to a vanishing of the light component of the polariton and the information is stored as atomic excitation (t_2). After a storage time $t_{stor} = t_3 - t_1$, the control field is switched on again and the light component of the polariton is recovered, being able to continue its propagation through the atomic medium.

time interval between switching off and on the coupling beam , which we call storage time t_{stor}. Note that a pulse can be stored entirely only if its compressed length is shorter than the atomic cloud length. Otherwise, only the part which is traveling through the medium when Ω_c is decreased to zero can be stored, which leads to a limitation in the storage efficiency.

Note that the light component of the polariton allows it to propagate through the medium in a coherent way while the atomic excitation component makes it sensitive to interactions between atoms. This makes EIT a good strategy for light-matter coupling that can be used to effectively achieve photon-photon interactions.

2.4.1 Electromagnetically-induced transparency with Rydberg atoms

When the long-range interactions between Rydberg atoms are strong enough to cause dipole blockade, the propagation of the probe field under EIT is affected. In this regime, the blockade radius is found when the interaction-induced shift equals the EIT linewidth $\Delta_{EIT} = \frac{\Omega_c^2}{2\gamma_{eg}}$, which is set by the EIT transparency width of a single atom [120] (see equation 2.15 and figure 2.3a)

$$r_b = \sqrt[6]{\frac{2C_6\gamma_{eg}}{\hbar\Omega_c^2}} \propto n^{11/6}. \tag{2.18}$$

When a probe photon interacts with an atom via EIT, it creates a Rydberg polariton which propagates through the medium with velocity v_{gr}. Due to the dipole blockade, the excitation of one atom to a Rydberg level shifts the Rydberg levels of atoms closer than r_b such that the coupling beam light is not on-resonant any more. Therefore, subsequent probe photons inside the blockaded region interact with two-level atoms, instead of three-level ones.

In the so-called dissipative regime, the probe field is sent on resonance ($\Delta = 0$) with the $|g\rangle \rightarrow |e\rangle$ transition. This ideally means that, although photons undergoing EIT are transmitted through the medium, blockaded photons are absorbed and scattered due to spontaneous emission from $|e\rangle$ state. That is to say, the dipole blockade in the dissipative regime leads to photon losses. This effect was first reported by Pritchard et al. as a suppression of the probe transmission as a function of the input probe photon rate [58] (see figure 2.11). Under ideal conditions, the time between two consecutive output photons is the *blockade time* $\tau_b = r_b/v_{gr}$, where v_{gr} is the group velocity, defined in equation 2.17.

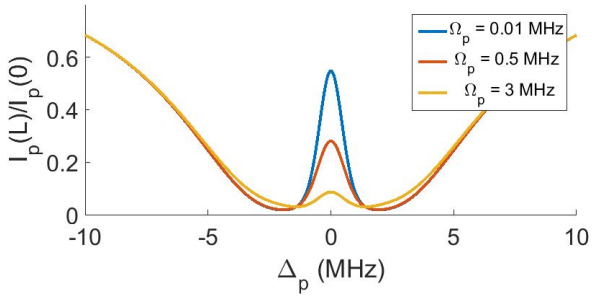

Figure 2.11: Reduction in probe transmission due to dipole blockade, for different number of input photons (or values of Ω_p). This simulation uses the model proposed by Petrosyan et al. [121].

The quantum regime is achieved when the probability of finding two output photons closer than a blockade time τ_b is strongly reduced. In this case, the output light is antibunched, as shown in figure 2.12. Note

that it is a feature of the EIT propagation which allows us to map the spatial correlation between two Rydberg polaritons (they cannot be closer than r_b) into time correlations of the output photons, which cannot be closer than τ_b. This change in the statistics of the output light was first demonstrated by Peyronel et al. [36]. In order to achieve this, a one-dimensional medium with a large OD per blockade radius OD_b is required. For the first, the transversal size of the interaction region (effectively two times the waist of the probe beam) should be smaller than r_b, so the parallel propagation of two Rydberg polaritons is negligible. The second can be explained because a nonlinearity at the single-photon level is reached when the probability that a blockaded photon is transmitted, which goes with e^{-OD_b}, is much lower than the transmission of a photon undergoing EIT. Otherwise, a significant amount of photons interacting with a two-level system can be found at the output, where it is not possible to distinguish them from the photons propagating through EIT.

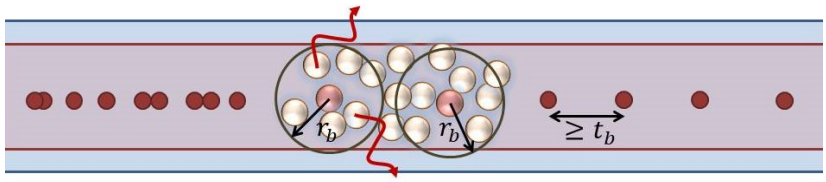

Figure 2.12: Graphical representation of the generation of antibunched light with Rydberg EIT. Dipole blockade does not allow the creation of two Rydberg polaritons closer than r_b, which leads to photon scattering (represented by the curved red arrows). The spatial correlations between Rydberg polaritons are mapped into time correlations of the output photons, due to the propagation feature of EIT.

As discussed previously in the introduction, the interaction between two photons needs to be mediated by a nonlinear medium at the single-photon level. That is, the response of the medium to a second photon should be different than the response to a first one. In the case of Rydberg EIT, we want a second photon to interact with a two-level system, while a first photon interacts with a three-level system. This is the case when the input pulse can be compressed within a blockade radius. The dissipative case is schematically represented in figure 2.13, where the

second photon is scattered while the first photon is transmitted. This behavior can be generalized for an input state with an arbitrary number of photons $|n\rangle$ as well as a weak-coherent state $|\alpha\rangle$. Therefore, this Rydberg EIT medium acts as a single-photon source, since we obtain a single photon at the output, localized within a pulse (see section 2.2).

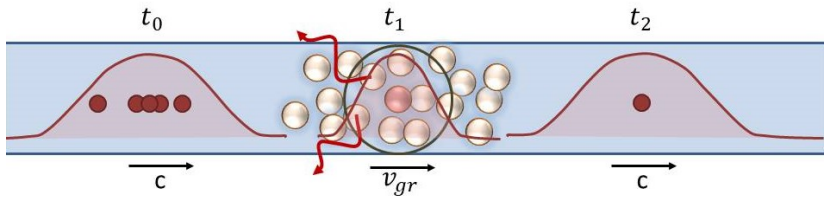

Figure 2.13: Graphical representation of the generation of a localized single photon after a probe pulse propagation under Rydberg EIT. If the probe pulse can be compressed within a blockade radius, only one photon can be transmitted while successive ones are scattered.

Therefore, strong experimental requirements should be fulfilled in order to have an efficient nonlinear medium at the single-photon level: the time-width of the probe pulse should be shorter than the blockade time, in order to prohibit more than one Rydberg excitation within the pulse. At the same time, the narrow EIT window imposes a limit to the minimum time-width of the probe pulse to fit within the EIT bandwidth. Moreover, we need $\mathrm{T_{EIT}}$ to be close to one, a large OD in order to have an $\mathrm{OD}_b \gg 1$ and a transversal size of the interaction region smaller than r_b.

Another method to exploit the nonlinearity in Rydberg EIT is found in the storage process [122]. In this case, the nonlinearity does not rely in the different transmission between a first and a second photon, but in the different retrieval times. Therefore, such severe OD_b conditions are not necessary. In a fully blockaded medium, the photon interacting with a three-level system can be stored as a collective Rydberg excitation, also called Rydberg spin wave, and be retrieved after a storage time t_{stor}, much longer than the time it takes for the other photon to travel through the medium length, in case is not absorbed. This behavior is schematically represented in figure 2.14. Furthermore, for a larger medium where two or more atoms can be excited to the Rydberg state, storage allows to increase the interaction time, which can lead to the de-

phasing of the higher-order excitation terms, as we will see in section 2.6.

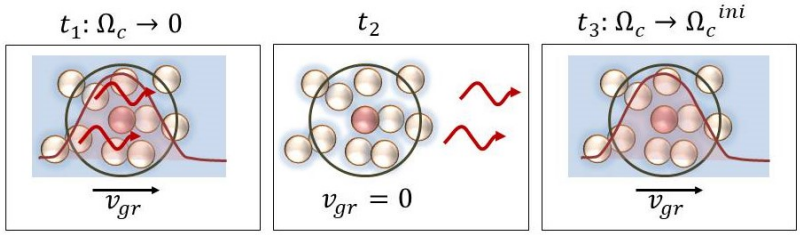

Figure 2.14: Graphical representation of the storage nonlinearity, for the case where the probe pulse is compressed within a blockade radius. Due to dipole blockade, only one photon interacts with a three-level system and hence, propagates through the medium as a Rydberg polariton with group velocity v_{gr} (t_1). Other photons, represented by curved red arrows, either interact with a two-level system and are scattered or escape the medium faster. As the Rydberg polariton can be stored as a Rydberg spin-wave (t_2), it can be retrieved after a much longer time $t_{stor} = t_3 - t_1$.

In this thesis, we focus on achieving a sufficiently strong nonlinearity in a Rydberg EIT system in order to obtain single photons at the output. Although dissipation and propagation effects are an important source of nonlinearity in a Rydberg EIT system, they can have detrimental effects on the output single photons. For example, the scattering due to dipole blockade can lead to lower indistinguishability of the single photons [123], to worse single-photon generation efficiency [124, 102] or to the creation of Rydberg pollutants, which are Rydberg excitations which cannot be retrieved in the probe mode but prevent the generation of single photons due to blockade effect [102, 50]. These effects must be taken into account when Rydberg EIT is used as a source of single photons. In order to study these effects, we can compare the single photons generated through EIT with those generated by an off-resonant (also called Raman) excitation process, where there is ideally no propagation or dissipation.

2.5 Off-resonant excitation to a Rydberg state

Another way to generate single photons is by means of a two-photon excitation to a Rydberg state with a large probe detuning Δ compared to Γ_{eg}. In the following, we will call this type of scheme off-resonant excitation, although it is also often referred to in the literature as Raman excitation. Consider an atomic ensemble with a size smaller than the blockade radius, so dipole blockade allows no more than one Rydberg excitation within the atomic cloud. Therefore, a single collective Rydberg excitation, also called Rydberg spin-wave, can be generated. This excitation process is schematically represented in figure 2.15a. Due to the large Δ, the population of the intermediate state can be neglected and the two-photon Rabi frequency for a single atom is given by $\Omega = \Omega_p\Omega_c/(4\Delta)$ [52]. The collective behavior of the excitation enhance the single-atom Rabi frequency by $\sqrt{N}\Omega$, as pointed out before. The state of the Rydberg spin-wave right after the excitation is

$$|R\rangle = \frac{1}{\sqrt{N}} \sum_j c_j(\vec{r_j}) e^{i(\vec{k}_p+\vec{k}_c)\vec{r_j}} |g_1, ..., r_j, ..., g_N\rangle, \tag{2.19}$$

where $\vec{r_j}$ is the position of the j^{th} atom, $\vec{k}_{p(c)}$ is the wavevector of the probe(coupling) laser fields and $c_j(\vec{r_j})$ is an amplitude coefficient, mainly given by the field amplitudes at $\vec{r_j}$. Note that these phases are also present in the Rydberg spin wave created by storage in EIT, although we have not explicitly written them down.

A single photon can be retrieved from the Rydberg spin-wave by using the coupling laser to transfer the excitation into the intermediate excited state. Due to the collective behavior of the excitation, the amplitudes and the phase terms $e^{i(\vec{k}_p+\vec{k}_c)\vec{r_j}}$ give information of the spatial mode of the input photons and hence, ensure the retrieval in its original mode (see figure 2.15b). Single photons generated through this method were first demonstrated by Dudin and Kuzmich in 2012 [59], while a high quality source has been demonstrated very recently [50].

In principle, it is possible to coherently transfer population from the ground to the Rydberg state by means of well-defined pulse areas with duration $t = \pi/|\Omega|$. However, several potential sources of errors should be taken into account [52]. For example, detuning errors due to Doppler broadening, AC Stark shifts caused by the excitation lasers and

energy shifts of the Rydberg state due to external magnetic or electric fields. Moreover, partial population of the intermediate state results in decoherence. Some excitation schemes, using a counter-intuitive pulse sequence where the coupling laser is applied before the probe, has also been used to increase excitation probabilities [125].

2.6 Dephasing and decoherence

The coherence time of a Rydberg spin-wave is usually limited by the relative motion of the atoms. The phase acquired by each atom after a time δt is $e^{i(\vec{k}_p+\vec{k}_c)(\vec{r_j}+\vec{v_j}\delta t)}$ where $\vec{v_j}$ is the velocity of the j^{th} atom [126]. The more different the relative phase is between the atoms, the less likely it is to retrieve the photon in its original mode. Note that δt correspond to t_{stor} for Rydberg EIT, and the time delay between the writing and the retrieving process for the off-resonant excitation scheme. Therefore, assuming a Boltzmann distribution of velocities, a low temperature of the cloud is necessary. Moreover, a low value of $\vec{k}_p + \vec{k}_c$ can be achieved by sending counter-propagating *probe* and *coupling* beams, so that $\vec{k}_p + \vec{k}_c = (k_p - k_c)\hat{x}$, where $\hat{x}$ denotes the unitary vector in the direction of the probe beam. However, since the wavelength of the coupling and probe lasers are very different, there is still a mismatch. Recently, new theoretical proposals to suppress the dephasing have been presented [127]. The decoherence rate of the $|g\rangle$ to $|r\rangle$ transition is usually limited by the excitation laser linewidth, which is difficult to decrease below the fundamental limit set by the radiative lifetime of Rydberg atoms, which is of the order of hundreds of microseconds. There are another several sources of dephasing, such as fluctuations of the external electric and magnetic field [128], blackbody radiation from environment [129, 130], interaction with ground-state atoms [131], radiation trapping [132, 124, 102], molecular formation [133].

Another source of error is the creation of pollutants [102, 50], which are Rydberg excitations that cannot be retrieved in the probe mode but prevent subsequent Rydberg excitations and hence the generation of single photons due to the blockade effect. This results in bunching of the second-order correlation function [102, 50]. Long-lived pollutants can be formed when atoms decay to another Rydberg level not coupled to the coupling field or when they move out of the region of the coupling beam.

These contaminants can then block the creation of Rydberg excitations over several trials, generating bunching between consecutive trials. Furthermore, in dissipative EIT, the presence of scattering constitutes an additional source of pollutants, which are formed by the reabsorption of scattered photons. Since these contaminants are in resonance with the coupling field, they can be removed from one trial to the next and are therefore short-lived. However, these could also decay to another Rydberg level, leading to long-lived pollutants.

For mediums with more than one Rydberg excitation, dipole-dipole and Van der Waals interactions are sources of dephasing [134, 135]. A Rydberg atom pair acquires an interaction-induced phase $e^{-i\Delta_{ij}t}$, where $\Delta_{ij} \simeq C_6/R_{ij}^6$ is the energy shift, where R_{ij} is the relative distance between i^{th} and j^{th} atoms. Since R_{ij} is not a constant value, the accumulated phase decouples the double excitation component from the phase-matched mode during the retrieval process. This interaction-induced dephasing happens for all the components with more than one excitation. For example, the component with three excitations acquires an interaction-induced phase of $e^{-i(\Delta_{ij}+\Delta_{ik}+\Delta_{jk})t}$. Therefore, the dephasing is normally greater for higher number of Rydberg excitations, which effectively enhanced the non-linearity [122] and can be used to generate single photons [59]. A schematic representation of the interaction-induced dephasing is shown in figure 2.16.

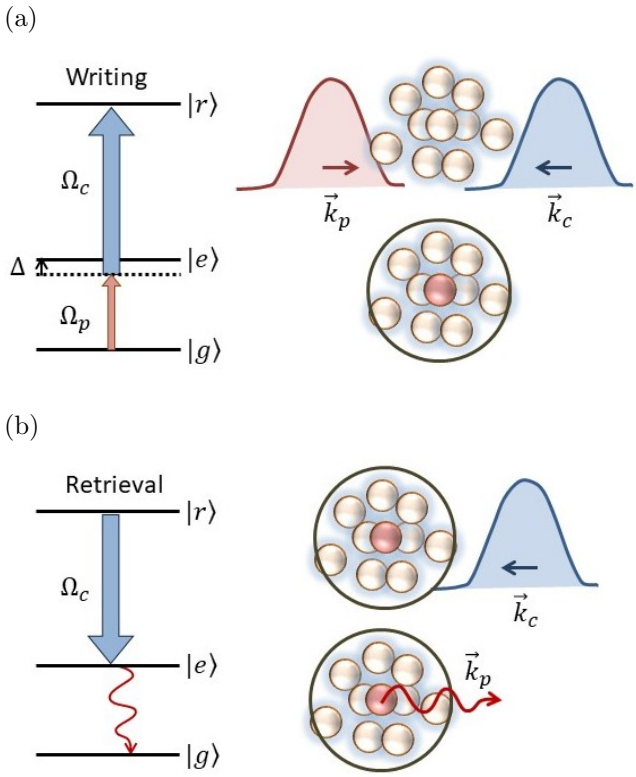

Figure 2.15: Schematic representation of the generation of a single photon by means of off-resonant excitation to a Rydberg state. In the top, a probe and a coupling pulse with well-defined areas are sent towards a small atomic ensemble. Due to dipole blockade, a collective Rydberg excitation is created with a phase given by the fields momentum $\vec{k}_p + \vec{k}_c$. In the lower plot, a resonant coupling pulse transfers the excitation to the excited state, forcing a probe photon to be emitted in the phase-matched direction.

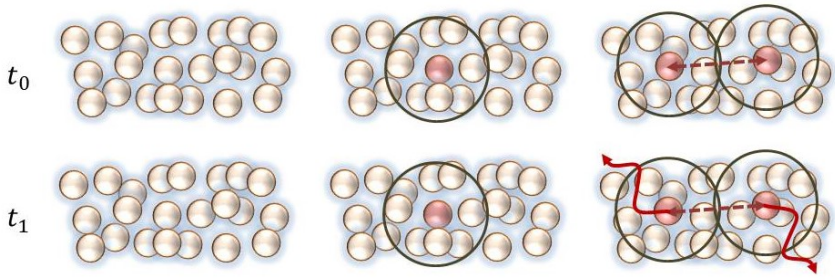

Figure 2.16: Schematic representation of dephasing due to Rydberg interactions, for the case where a maximum of two Rydberg excitations can be created in the medium. The initial state of the system is represented in the row with t_0. Given the limited atomic cloud size, it is a superposition of none (left), one (middle) or two (right) Rydberg excitations. Since only the double excitation component is affected by the dipole-dipole interactions, after a sufficiently long time $t_1 - t_0$, the probability to retrieve the double excitation in the phase-matched mode is strongly reduced. This is shown in the double-excitation component (right) of the t_1 row, where the curved red lines represent the photon loss.

Chapter 3

Experimental setup

3.1 General description

Experiments with Rydberg atoms require a complex experimental setup. In addition to the common apparatuses used in experiments with cold atoms, such as a vacuum chamber and a controllable system of frequency stabilized lasers, there are other requirements that must be fulfill to achieve nonlinear effects at the level of a single photon. First, a strong light-matter coupling with an optical depth OD$\gg 1$ is required. Second, the probe beam must be focused with a diameter smaller than the blockade radius, i.e. smaller than ~ 10 μm, to prevent the propagation of more than one polariton at a time such that we can assume that the medium is one-dimensional. In addition, atoms should be strongly confined, so that only few blockade spheres can be fitted within the interaction region of the atomic ensemble. In Rydberg EIT experiments, we also need small linewidths of the excitation lasers and a coupling Rabi frequency strong enough to obtain good EIT transparency. Finally, a system for the detection and characterization of output photons is necessary.

In our experiment, we achieve a dense and small atomic cloud of ^{87}Rb atoms by loading them into a dipole trap from a magneto-optical trap. This will be described in section 3.4. To excite the atoms to a Rydberg level, the dipole beam is turned off and the probe beam is sent with a counter-propagating coupling beam. The excitation can be carried out under EIT conditions or by means of an off-resonant excitation. The different sequences will be described in section 3.5. Finally, the re-

trieved photons are sent to the detection and analysis setup, presented in section 3.6.

Most of the experimental setup, such as the laser system, the magneto-optical trap and the setup for the atomic excitation and the detection of photons, was already built at the beginning of my PhD project. Although some minor changes and improvements were also made, the main change was the implementation of the dipole trap. Therefore, we will describe its setup in more detail (see section 3.4.4). A more in-depth explanation of the previous experimental setup, as well as detailed references to the equipment that was already in place, can be found in Dr. Emanuele Distante's thesis [101].

3.2 Laser system

Our laser system is composed of four different lasers called trap, repumper, coupling and dipole trap, according to their purposes, as we will see later.

- **Trap laser:** It has a wavelength of 780 nm and addresses transitions from the hyperfine ground state $|5^2S_{1/2}, F = 2\rangle$ of the D_2 line of ^{87}Rb $|5^2S_{1/2}\rangle \rightarrow |5^2P_{3/2}\rangle$. It is a Toptica TA-pro, a tunable external-cavity diode laser (ECDL) used in another experiment of our laboratory, where its frequency is actively stabilized by saturation absorption spectroscopy [136]. Then, a seed is sent to our experiment, where it is amplified by a Toptica BoosTA Amplifier and divided into four lines that pass through four different acousto-optic modulators (AOM) in a double-pass configuration. The intensity and frequency of the light at the output depends on the RF signals sent to the AOMs, which are generated by a field-programmable gate array (FPGA)-based arbitrary waveform generator from Signadyne. Each of the lines is destined for a different process, which are generally: trap the atoms in the magneto-optical trap, generate the probe light, optically pump the atoms to the $|5^2S_{1/2}, F = 2, m_F = 2\rangle$ Zeeman state and stabilize the frequency of the coupling laser.

- **Repumper laser:** It also has a wavelength of 780 nm, but addresses transitions from the $|5^2S_{1/2}, F = 1\rangle$ hyperfine state of the

D_2 line. The repumper laser is based on a distributed feedback diode laser (DFB) from EagleYard. Its frequency is actively stabilized using the frequency of the trap laser as a reference by means of light beating spectroscopy [101]. The repumper frequency and intensity is also controlled by an RF signal sent to an AOM.

- **Coupling laser:** It connects the intermediate excited state to the Rydberg state $|5^2P_{3/2}\rangle \rightarrow |r\rangle = |nS_{1/2}\rangle$ and has a wavelength of around 480 nm, which can be slightly changed to address different Rydberg states. It is a commercial Toptica TA/DL SHG pro laser, which consists of a tunable external-cavity diode laser at 960 nm, an amplifier and a second-harmonic generation (SHG) cavity, where the frequency of the light is doubled. It is also stabilized with respect to the trap laser frequency, by searching for EIT signals in a Rb cell at room temperature [101]. The coupling light is also sent through an AOM in double-pass configuration in order to control the intensity and frequency of the beam sent to the atoms. The combined linewidth of both trap and coupling lasers is estimated to be a few hundreds kHz, based on laser data sheets.

- **Dipole trap laser:** It has a wavelength of 852 nm, far-detuned with respect to any resonance of the two D lines of ^{87}Rb atoms. The dipole trap laser is based also on a distributed feedback diode laser from EagleYard. An output power of 40 mW acts as a seed of a Toptica BoosTA pro Amplifier system, after which we obtain a power of 2.6 W. Since it is not on resonance with any atomic transition, the dipole trap laser does not need frequency stabilization. An AOM in single-pass configuration is used, in this case, to control the intensity of the beam, so that we are able to turn it on and off quickly.

3.3 Experimental sequence

The experimental sequence, shown schematically in figure 3.1, is composed of many different processes, which can be grouped in two general ones: the preparation of the atomic ensemble and the realization of the experiment itself, i.e. the excitation of atoms and detection of the retrieved photons. The loading of the atoms in the dipole trap lasts 2.05 s and requires different steps, which will be explained in more detail in sections 3.4.1-3.4.4. Once the loading is completed, the time available

to perform the experiment is limited by the lifetime of the dipole trap. In our case, the number of atoms and, therefore, the optical depth is acceptably high (OD ~ 5) for 200 ms. However, the dipole trap potential results repulsive for Rydberg atoms and leads to AC Stark shifts. Then, the dipole trap must be turned off during excitation to Rydberg levels. This can be done without losing atoms if the dipole trap is modulated with a frequency higher than the frequency associated to the trap. In this way, every time the dipole trap is turned off, we can make an excitation trial. This reduces the available experimental time to slightly less than half, i.e. less than 100 ms (see figure 3.1). In addition, an upper bound in the modulation frequency, that limits the number of trials, is given by the time we need to perform an excitation and retrieval of the photons, which is $\sim 2-5\ \mu s$. When the sequence ends, the cloud loading process can start again.

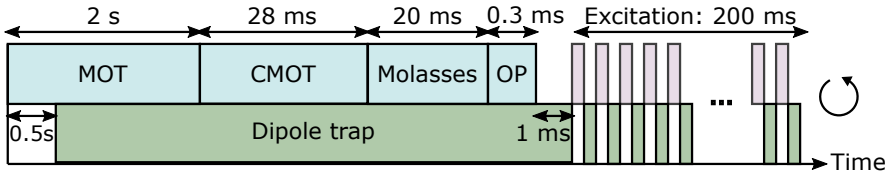

Figure 3.1: Scheme of the experimental sequence. MOT: magneto-optical trap, CMOT: compressed magneto-optical trap, OP: optical pumping.

3.4 Loading of the atoms

As mentioned before, the loading of the atoms in the dipole trap involves many different processes with lengths shown in figure 3.1. In the following sections, we will describe each of these processes, emphasizing the dipole trap.

3.4.1 Magneto-optical trap

Atoms are initially loaded into a magneto-optical trap (MOT) [137], which consists of an ultra-high vacuum chamber; three red-detuned laser beams, located almost perpendicular to each other and reflected backwards; and two magnetic coils in anti-Helmholtz configuration, as can be seen in figure 3.2. The two coils create a magnetic field gradient that

is zero at the intersection point of the three beams.

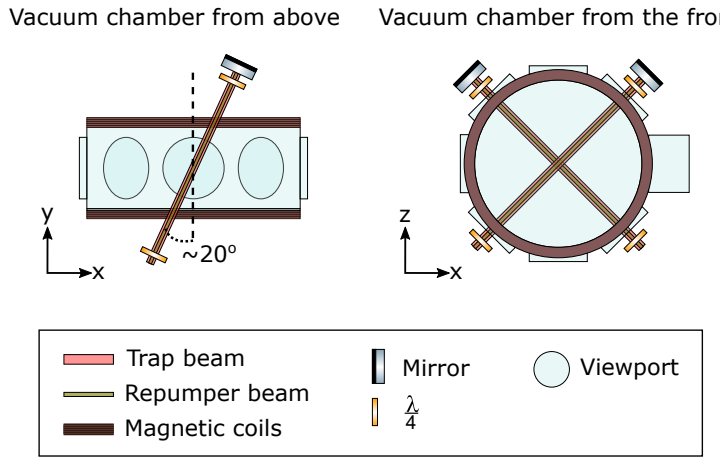

Figure 3.2: Experimental scheme of the vacuum chamber and MOT beams (the trap and repumper beams overlap) [138].

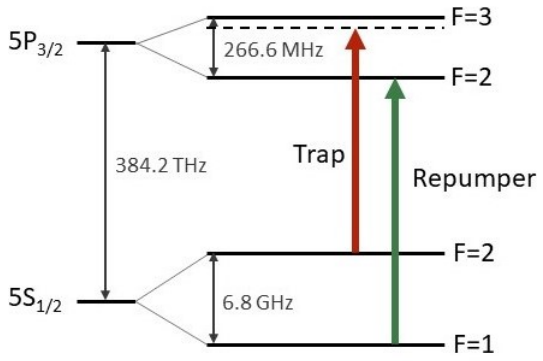

Figure 3.3: Transitions used for the MOT

In an MOT, atoms are slowed down due to momentum kicks given by unidirectional absorption of photons followed by emission in a random direction. The Doppler effect makes only the atoms moving towards the red-detuned laser beams to see the photons in resonance and, therefore, be able to absorb them. Due to momentum conservation, the absorption of photons pushes the atoms towards the point of intersection of the

three beams. The radiation forces from the laser beams balance each other only for a stationary atom, reducing the atomic velocity and therefore the temperature of the system. This technique is known as optical molasses. In addition to cooling the atoms, we can also confine them at the intersection point thanks to the magnetic field gradient and a correct polarization of the laser beams. The magnetic field gradient produces a Zeeman shift that depends on the position of the atom. If the light is circularly polarized with the correct handedness, the probability of absorption is greater when the atom is farther from the center. The atoms entering the intersection region of the laser beams are slowed down due to the optical molasses and the position-dependent force pushes the cold atoms toward the center of the trap. Therefore, the MOT provides a good source of atoms for loading the dipole-force trap [139].

To implement the MOT, we use the closed transition $|5S_{1/2}, F = 2\rangle \rightarrow |5P_{3/2}, F = 3\rangle$, coupled by the trap laser (see figure 3.3). Although the decay to the state $|5S_{1/2}, F = 1\rangle$ has a very low probability, this can happen because many excitation cycles are needed to reduce the momentum of the atoms. To pump the atoms back to the closed transition, we apply a repumper beam, co-propagating with the trap beam, resonant with the transition $|5S_{1/2}, F = 1\rangle \rightarrow |5P_{3/2}, F = 2\rangle$. The total peak intensities of the trap and the repumper during the MOT are $I_{trap} \approx 2$ mW·mm^{-2} and $I_{rep} \approx 4$ mW·mm^{-2} and the detuning of the trap is $\Delta_{trap} = -19$ MHz $\approx -3\Gamma$. The detuning is defined as $\Delta = \omega_{transition} - \omega_{beam}$ to be consistent with how it is normally written in the literature.

3.4.2 Compressed magneto-optical trap

The compressed magneto-optical trap (CMOT) method allows us to increase the atomic density above that obtained in the steady state of the MOT without significantly increasing the temperature [140]. For that purpose, the gradient of the magnetic field is increased by a ramp, along with the detuning of the trap beam. These changes are combined with a decrease in the intensity of the trap and repumper beams in order to reduce the radiation pressure.

The increase in the current sent to the magnetic coils is done with a controllable current source with a fast slew rate from Servowatt. It allows the variation of the magnetic field gradient with a ramp dura-

tion of 18 ms. The trap detuning goes from $\Delta_{trap} = -19$ MHz to $\Delta_{trap} = -53$ MHz $\approx -9\Gamma$ in the same time interval, while the trap and repumper peak intensities are reduced with respect to the MOT stage, but kept constant during the ramp time at $I_{trap} \approx 0.3$ mW·mm^{-2} and $I_{rep} \approx 1.5$ μW·mm^{-2}. After the end of the ramp, all parameters remain constant for an additional 10 ms. A scheme of the relative detunings and intensities with respect to the MOT and molasses processes can be seen in figure 3.4.

3.4.3 Molasses and optical pumping

The molasses phase is applied to reduce the temperature of the atomic cloud. During this process, the magnetic field gradient is turned off and only Doppler cooling is performed. The intensities of the trap and the repumper in this phase are $I_{trap} \approx 0.1$ mW·mm^{-2} and $I_{rep} \approx 0.2$ μW·mm^{-2}; and the detuning of the trap is $\Delta_{trap} = -63$ MHz $\approx -10\Gamma$. The temperature of the atoms after this stage is $T \sim 50$ μK, measured by imaging the atomic cloud for different time of flights [101] without the dipole trap.

Later, we prepare the atoms in the initial state $|g\rangle = |5S_{1/2}, F = 2\rangle$ by applying the repumper at maximum intensity for 200 μs.

3.4.4 Dipole trap

The density of the atomic cloud can be increased and the size decreased by optically trapping the atoms using a highly focused far-detuned laser beam [141, 142]. As the intensity of such a beam has a steep gradient in space, this generates a Stark shift in the atom that depends on its position. For a negative detuning $\Delta_{dt} < 0$, this shift creates an attractive force on the atoms towards the point of maximum intensity. If Δ_{dt} is sufficiently large, a Gaussian beam with peak intensity I_0 and beam waist ω_{dt} produces a transversal force $F \propto I_0/(\Delta_{dt}\omega_{dt}^2)$ [143].

The wavelength of our dipole trap is 852 nm. This wavelength was chosen such that it is compatible with the anti-reflection coating of the vacuum chamber viewports and, at the same time, generates a negligible scattering in the atoms (see figure 3.5a). As mentioned before, the dipole trap laser system is composed by a distributed feedback diode laser and

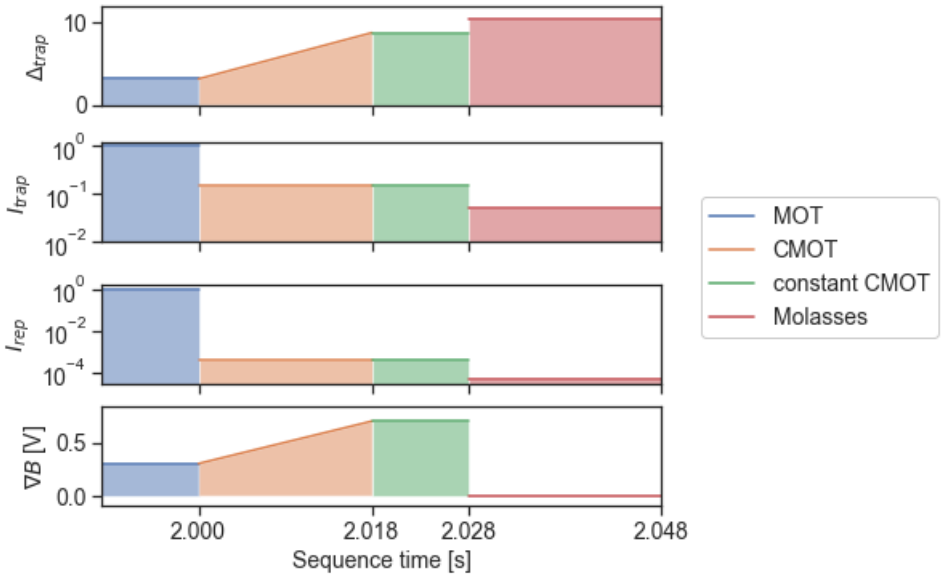

Figure 3.4: Scheme for relative intensities, trap detuning and magnetic field gradient inside the different loading processes. The intensities are normalized with respect to the intensity sent in the MOT process (note that they are shown in logarithmic scale). The detuning of the trap laser is in units of Γ and the gradient of the magnetic field is, in fact, voltage sent to the magnetic coils current supply.

an amplifier, which gives an output power of 2.6 W. This is sent through an AOM in single-pass configuration, where part of the power is lost. The maximum value, measured close to saturation in the first order, is around 1.6 W. After that, the light is sent towards the vacuum chamber by coupled it into a single-mode fiber from Schäfter+Kirchhoff. The dipole trap power at the vacuum chamber is around 1.2 W and it is focused with a beam waist of $\omega_{dt} \approx 27$ μm, which leads to a peak intensity of $I_0 \sim 1$ kW/mm^2. The experimental setup for the dipole trap can be seen in figure 3.5b. We calculate a trap depth of $U_{dt} \approx \frac{3\pi c^2}{2\omega_{ge}^3}\frac{\Gamma}{\Delta_{dt}} \cdot I_0 \sim 0.45$ mK, where ω_{ge} is the transition frequency of the D2 line of ^{87}Rb. We can see that the obtained trap depth is much higher than the average temperature of the atoms after molasses. The scattering rate is $R_{scatt} \approx \frac{\Gamma}{\hbar\Delta_{dt}} U_{dt} \sim 10$ photons per atoms per second and the frequency of the trap in the radial direction is calculated to be 15 kHz.

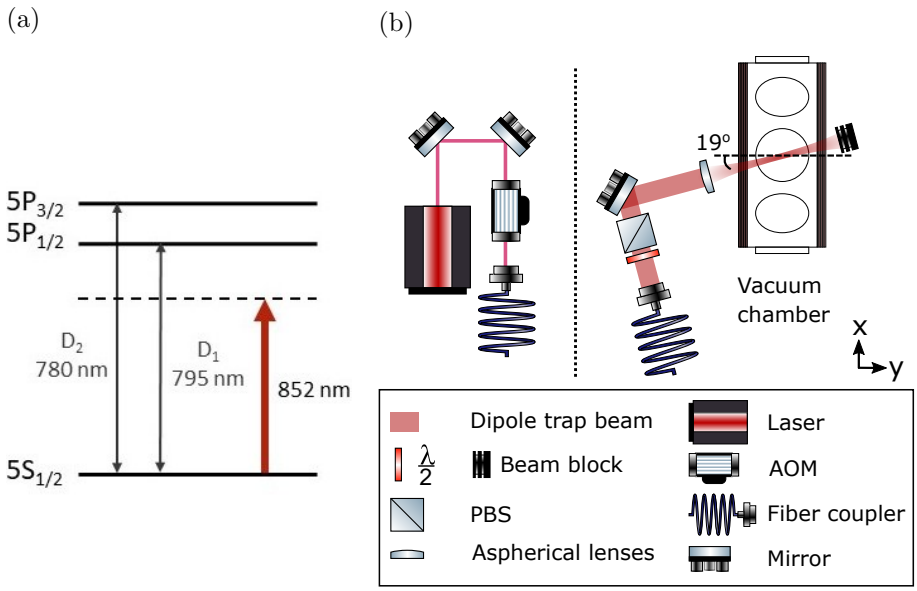

Figure 3.5: **(a)** Dipole trap detuning with respect to the D lines transitions of ^{87}Rb (not to scale). **(b)** Experimental scheme of the dipole trap [138].

The characterization of the atomic cloud loaded in the dipole trap is done through absorption imaging. A beam resonant with the transition $|5S_{1/2}, F = 2\rangle \rightarrow |5P_{3/2}, F = 3\rangle$ is focused in the atomic cloud as can be seen in the setup scheme of figure 3.6. Then, a telescope consisting of two lenses with focal lengths 100 mm and 200 mm magnified by two the image of the beam obtained by a CCD camera. The beam transmission in the pixel located at the position (x, y) is

$$T(x,y) = \frac{i_{atoms}(x,y) - i_{background}(x,y)}{i_{no\ atoms}(x,y) - i_{background}(x,y)}, \tag{3.1}$$

where $i_{atoms}(x, y)$ correspond to the image of the beam through the cloud, $i_{no\ atoms}(x, y)$ to the image of the beam without the atoms and $i_{background}(x, y)$ to the background image. The size of the atomic cloud can then be obtained by a $2D$ Gaussian fit to the transmission, shown in figure 3.7. The result gives a transverse length of $\omega_{trap} = 34\ \mu$m.

The optical depth of each pixel $OD(x, y)$ can be calculated from the

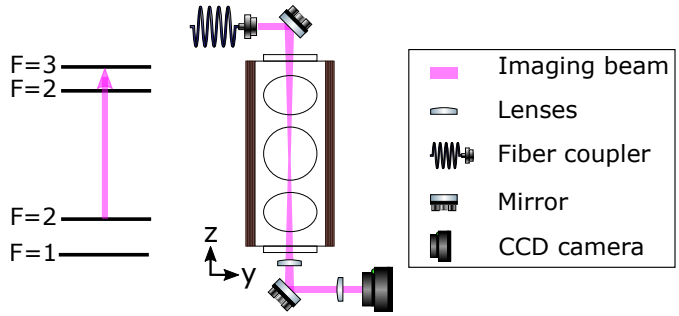

Figure 3.6: Experimental scheme of the absorption imaging used to characterized the atomic cloud [138]. The imaging beam is sent on resonance with the transition $|5S_{1/2}, F = 2\rangle \rightarrow |5P_{3/2}, F = 3\rangle$.

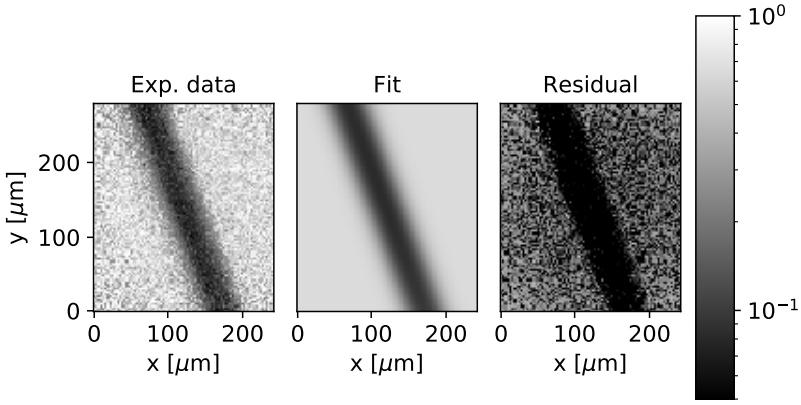

Figure 3.7: Gaussian fit to the transmission for obtaining the transversal size of the dipole trap. The plot in the left shows the transmission obtained from the images, in logarithmic scale. The plot in the middle shows the $2D$ Gaussian fit to the experimental data and the third plot shows the residual, which correspond to the experimental data minus the fit.

transmission using the equation

$$T(x, y) = e^{-OD(x,y)}(1 - e^{-OD_{sat}}) + e^{-OD_{sat}}, \tag{3.2}$$

where OD_{sat} is the maximum value of the optical depth that we can measure. Then, we can estimate the atomic density in each pixel using $\rho(x, y) = OD(x, y)/(\sigma\omega_{trap})$, where σ is the absorption cross section of the atoms and ω_{trap} the transversal size of the dipole trap previously

obtained. Within a small region of 20×10 pixels in the center of the cloud, corresponding to 703 μm^2, we calculate an averaged atomic density of $\sim 3 \cdot 10^{11}$ cm^{-3}.

Given the calculated value of R_{scatt}, the time required to heat the atoms out of the dipole trap by photon scattering is more than 50 s. Therefore, we expect the lifetime of the dipole trap to be limited by collisions with the background gas. The decay time of a dipole trap due to collisions is described by the equation [142]

$$\frac{dN}{dt} = -\alpha N - \beta N^2 - \gamma N^3, \tag{3.3}$$

where the first term refers to the background losses, the second to two-body losses and the third to three-body losses. Since the dominant term corresponds to background losses, the lifetime of the dipole trap can be defined as $\tau = 1/\alpha$, which corresponds to the time it takes to reduce the number of atoms to $1/e$.

To calculate the lifetime of our dipole trap, we take images of the atomic cloud at different times after the molasses (see figure 3.1), which is when the atoms are trapped only by the dipole trap. We call this time the trapping time. In each image, the number of atoms is calculated within the small region of 20×10 pixels previously defined. The amount of atoms the beam goes through in each pixel can be estimated using $N(x, y) = OD(x, y)A_{pixel}/\sigma$, where A_{pixel} is the real area associated with a pixel (in our case $A_{pixel} \approx 1.87$ μm) and $OD(x, y)$ is obtained from equation 3.2. On the left of figure 3.8, the transmission of the atomic cloud is shown after 60 ms of trapping time. On the right, we show the number of atoms obtained for different trapping times together with the fit to equation 3.3, from which we obtain $\alpha \approx 2.2 \cdot 10^{-3}$ Hz, $\beta \approx 4 \cdot 10^{-11}$ Hz/atom and $\gamma = 0$ is fixed. This results in a lifetime of $\tau \approx 0.46$ s.

3.5 Excitation of atoms

During the process of excitation of atoms to Rydberg levels, the dipole trap is turned off to eliminate all AC-Stark shifts and prevent the loss of Rydberg atoms due to the repulsive potential of the dipole trap.

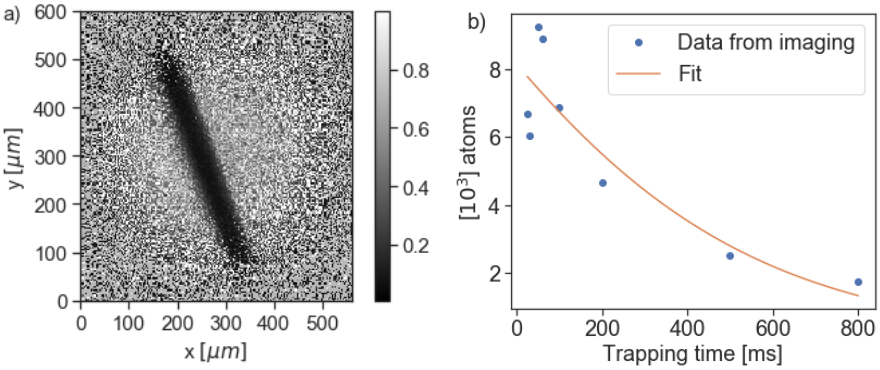

Figure 3.8: Characterization of the dipole trap. **(a)** Transmission of the atomic cloud obtained by absorption imaging, for a trapping time of 60 ms. **(b)** Evolution of the number of atoms calculated in a small region in the centre of the atomic cloud for different trapping times. A fit to this data gives a lifetime of $\tau \approx 0.46$ s.

As mentioned before, atoms are initially prepared in the ground state $|g\rangle = |5S_{1/2}, F = 2\rangle$. The excitation is done by sending a probe light, which couples the transition $|g\rangle = |5S_{1/2}, F = 2\rangle \rightarrow |e\rangle = |5P_{3/2}, F = 3\rangle$, together with a counter-propagated coupling beam, which couples the intermediate state with the Rydberg state $|e\rangle = |5P_{3/2}, F = 3\rangle \rightarrow |r\rangle = |nS_{1/2}\rangle$. The probe beam is sent perpendicularly to the vacuum chamber viewport, but at an angle of 19^o with respect to the dipole trap beam. Before the chamber, the probe beam passes through an aspheric lens that focuses it on the center of the atomic ensemble with a beam waist of $w_p \approx 6.5$ μm. The strong dipole-dipole interaction of Ryberg atoms leads to blockade and only a Rydberg excitation is allowed per blockade sphere. The experimental scheme of the excitation process can be seen in figure 3.9.

The OD of the medium is obtained from a fit to the transmission for different detuning of the probe beam Δ, in absence of the coupling beam. In a separate measurement, the coupling beam is turned on, which opens a transparency window in the probe transmission by means of EIT, as mentioned in section 2.4. We can obtain some important parameters such as Ω_c from a fit of the transmission for different detuning Δ of the probe light. An example of this measurement for the Rydberg state $|r\rangle = |70S_{1/2}\rangle$ is shown in figure 3.10, where we obtain OD ≈ 6 and

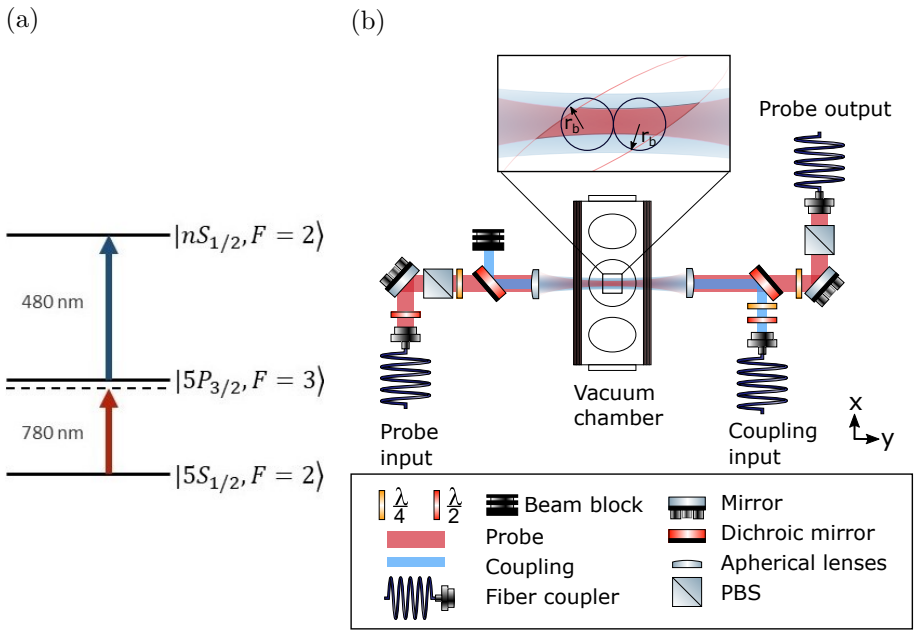

Figure 3.9: **(a)** Transitions involved in the excitation of the atoms to the Rydberg state. **(b)** Experimental scheme of the excitation process [138].

$\Omega_c = 10.61 \pm 0.05$ MHz.

The FPGA boards (Signadyne) that are used to control the RF signal sent to the acousto-optic modulators include an arbitrary wave-function generator (AWG) that allows us to fully control the amplitude envelope of the RF signal. This functionality enables to send probe and coupling pulses with different shape, amplitude and duration towards the atomic cloud.

When we excite the atoms under EIT conditions, the probe and the coupling light are sent in resonance with the intermediate state ($\Delta = 0$). In this case, the blockade effect produces scattering of photons. The experiment is performed by sending weak-coherent pulses of probe light to the medium. If the coupling field is on, these pulses propagate coherently in the form of Rydberg polaritons with a group velocity v_{gr} much smaller than the velocity of light in vacuum c. To perform storage, we

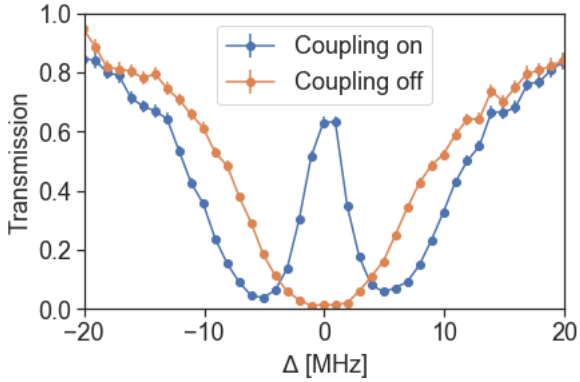

Figure 3.10: Transmission of a probe beam for different detunings with the transition $|g\rangle = |5S_{1/2}, F = 2\rangle \rightarrow |e\rangle = |5P_{3/2}, F = 3\rangle$ with (in blue) and without (in orange) a coupling field resonant with the transition $|e\rangle = |5P_{3/2}, F = 3\rangle \rightarrow |r\rangle = |70S_{1/2}\rangle$. The input rate of probe photons is 0.3 MHz. A fit to this data gives $OD \approx 6$ and $\Omega_c = 10.61 \pm 0.05 MHz$.

turn off the coupling beam when polaritons are propagating through the medium. After an arbitrary time, we can retrieve the probe photons by turning on the coupling beam again. An example of the optical pulses for the probe and coupling fields for storage and retrieval through EIT, together with the measured probe pulses, is shown in figure 3.11. The optical pulses are obtained by estimating the response of the AOMs to the arbitrary-wave functions that we generate.

We can also excite the atoms to Rydberg levels by sending probe and coupling pulses in the off-resonant excitation configuration, i.e. the optical fields are detuned with respect to the intermediate state, so that the interaction with it is negligible. Specifically, the detuning is set to $\Delta = -40$ MHz for the probe and $\Delta_c = 40$ MHz for the coupling beam. In addition, the time widths of both pulses and the amplitude of the coupling one are optimized so that the probability of excitation is greater. In this way, collective Rydberg excitations are created within our atomic cloud. After an arbitrary time, these excitations can be mapped into probe photons by sending a new coupling pulse to the medium. This coupling pulse can be sent in resonance with the intermediate state, which will change the frequency of the retrieved photons to be in resonance with the $|g\rangle \rightarrow |e\rangle$ transition due to energy conservation. An

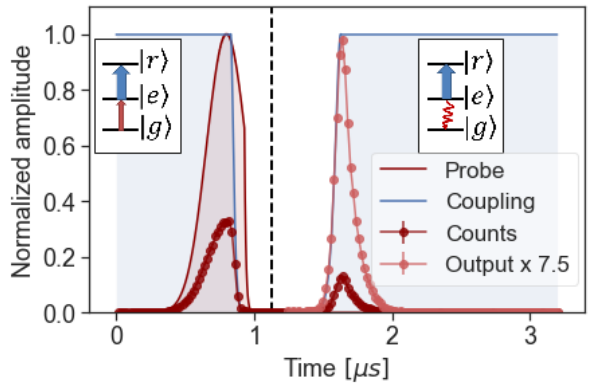

Figure 3.11: Optical pulses for excitation of atoms under EIT conditions. In this case, both probe and coupling beam are sent on resonance with the intermediate state. The detected probe counts (red dots) are also shown, normalized by the input pulse. The probe counts detected for Time < 1 μs correspond to the part of the slow-light pulse retrieved from the medium before the coupling beam is turned off (note that we cannot compress the entire input pulse inside the medium).

example of the optical pulses used to generate the collective excitation, together with the measured temporal distribution of the probe counts, is shown in figure 3.12.

3.6 Photon detection

Probe photons are detected by two single-photon avalanche detectors, one from Excelitas (model SPCM-AQRH-14-FC) with $\sim$ 100 Hz of dark counts and the other from Laser Components (model COUNT-10C-FC) with $\sim$ 10 Hz of dark counts. The signals generated from the detection clicks are sent to a time-to-digital converter (TDC) from Signadyne, which has a resolution of 320 ps.

As mentioned in 2.2, the second-order correlation function can be measured by sending the retrieved photons through a 50:50 beamsplitter from Thorlabs with the two outputs connected to the two single-photon avalanche detectors, as shown in figure 3.13. This configuration is known as the Hanbury-Brown and Twiss experiment. The signals

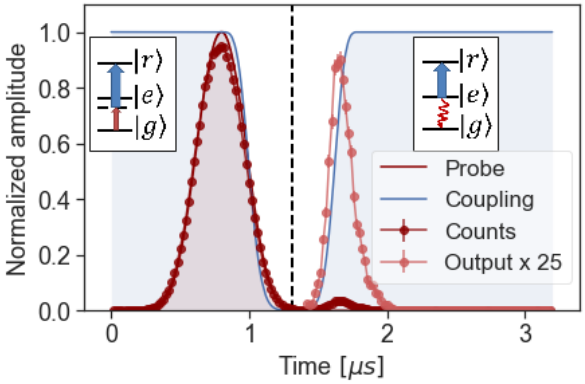

Figure 3.12: Optical pulses used for off-resonant excitation to the Rydberg level. In this case, probe is sent with a detuning of -40 MHz with respect to the intermediate state. Probe counts are also shown, normalized by the input pulse.

from both detectors, together with a TTL signal that marks the start of an excitation trial, are sent to the TDC. The resulting times are saved in timestamp files, which are subsequently analyzed to obtain the statistics associated with the output photons.

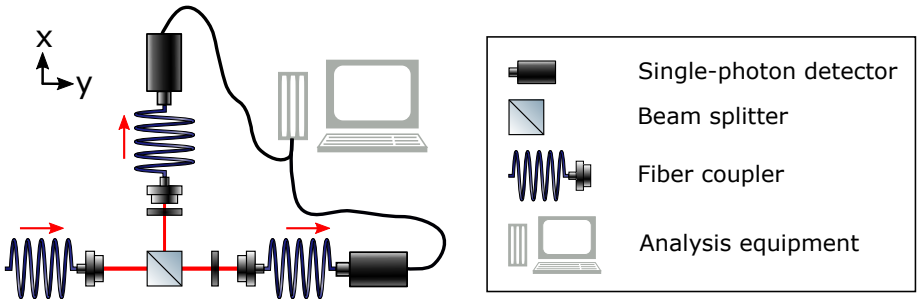

Figure 3.13: Experimental scheme of the Hanbury-Brown and Twiss experiment [138].

Chapter 4

Towards single-photon nonlinearity

4.1 Introduction

As mentioned in section 1.1, a medium with nonlinearity at the single-photon level is a key requirement for processing quantum information carried by single photons. In simple words, such a medium has a different response when it interacts with a single photon than when it interacts with more than one. Such a nonlinearity enables the quasi-deterministic generation of single photons and the realization of photonic quantum processing, e.g. photon-photon gates.

It has been demonstrated that a medium made of Rydberg atoms excited under EIT conditions can show nonlinearity at the single-photon level, as we have discussed before in section 2.4.1. For the dissipative case, this nonlinearity is translated as a minimum separation between photons propagating through the medium, which means that only a single photon can leave the medium at a time. For quantum communication purposes, this medium should generate single-photon pulses located within a pulse, when weak-coherent states of light are sent as an input.

However, at the beginning of this PhD project, our cloud of Rydberg atoms was only showing nonlinear effects when pulses with more than sixty input photons of average were sent to the medium. Reaching the quantum regime, i.e. nonlinearity at the single photon level, was therefore a first major goal of this PhD work. Since then, we have im-

plemented many improvements in the way we load the atomic cloud and excite the atoms. In this section, we review all the changes done to the experiment that allowed us to reach single-photon nonlinearity. We also present a characterization study of the nonlinearity in three different stages of the project: at the beginning, to define the starting point; just before implementing the optical dipole trap and at the final stage. This characterization was done following two different methods, depending on how far we were from the quantum regime. All of the measurements presented in this chapter were carried out under EIT conditions.

4.2 Characterization of optical nonlinearity in Rydberg EIT

In general, the nonlinearity is assessed by sending weak coherent pulses into the Rydberg medium and measuring the output light. For a weakly-blockaded medium, the photon statistics at the output are very similar to that of the weak coherent state. As a consequence, a measurement of the second-order correlation function gives values very close to the classical one ($g^{(2)}(0) = 1$). In this case, the nonlinearity is assessed by measuring the number of input photons at which the number of output photons saturates. For a strongly-blockaded medium, the second-order correlation function can be used to characterize the output light statistics, since it shows values much smaller than one.

4.2.1 Weakly-blockaded medium

If the interactions between Rydberg atoms are negligible, the mean number of output photons has a linear relation with the mean number of input photons, given by the transmission $T = n_{out}/n_{in}$. However, when interactions between Rydberg atoms become important, the output number of photons n_{out} saturates when n_{in} increases, due to the Rydberg blockade effect. The saturation value is described by the parameter N_{max}, which gives the maximum number of output photons corrected by the linear transmission T. The relation between n_{out}, n_{in} and N_{max} can be simply described by the equation [76]

$$n_{out} = N_{max} \cdot T \left(1 - e^{\frac{-n_{in}}{N_{max}}}\right). \tag{4.1}$$

In our experiment, n_{in} and n_{out} are obtained from the number of detection events recorded in a single-photon avalanche detector per trial, cor-

rected by the detection efficiency. In the absence of atoms, the obtained value correspond to n_{in}. When the pulse is retrieved after propagation or storage in a Rydberg medium, we obtain n_{out}. By sending input pulses with different amplitudes, we can obtain N_{max} by fitting the data to the equation 4.1, as will be shown in the next sections. Ideally, in a medium with single-photon non-linearity, $N_{max} = 1$.

4.2.2 Strongly-blockaded medium

For a strongly-blockaded medium, the output light shows quantum statistics, which can be measured with the second-order correlation function. The definition can be found in the equation 2.7 of section 2.2. Ideally, we expect the light retrieved from a Rydberg EIT medium with nonlinearity at the single-photon level to show antibunching ($g^{(2)}(0) < 1$) with a time-width related to the blockade time $\tau_b = r_b/v_{gr}$, where v_{gr} is the group velocity of the polaritons in the medium.

The second-order correlation function is obtained by sending the output light through a Hanbury-Brown and Twiss experiment, consisting on a beamsplitter and two single-photon avalanche detectors (see section 3.6). The arrival times of the photons for each detector, together with trigger times for each trial, are saved in a time-stamp file. First, we select a detection window with starting time t_0 after the trigger and a duration Δt. Then, $g^{(2)}(t, \tau)$ is obtained from the equation 2.10, where t is the starting time of the detection window in the first detector ($t \equiv t_0^{(1)}$) and $t + \tau$ is the starting time of the second detector ($t + \tau \equiv t_0^{(2)}$). To measure the statistics of the whole pulse, we select detection windows in both detectors with $t_0^{(1)} = t_0^{(2)} = 0$ and a Δt longer than the pulse duration Δt_{pulse}, such that the detection windows take into account the whole retrieved pulse. In this case, the second-order correlation function $g^{(2)}(0, 0)$ is labeled as $g^{(2)}_{\Delta t}(0)$. A perfect single photon located within a pulse should give a zero probability to obtain two clicks within the same pulse and then a $g^{(2)}_{\Delta t}(0) = 0$. To obtain a time-resolved $g^{(2)}(\tau)$, Δt is taken to be much shorter than Δt_{pulse} and $g^{(2)}(t, \tau)$ is integrated over all the possible values of $t \equiv t_0^{(1)}$. The coincidence histogram obtained, similar to figure 2.6 of section 2.2, will have a resolution given by a bin size of $2\Delta t$. Figure 4.1 shows an example for a bin size of 50 ns. This measurement was taken for a Rydberg state with $n = 90$ and a weak long input pulse. In the upper plot, the range of τ taken to calculate

the coincidences is longer than the separation between different trials $t_{trial} = 16\ \mu s$. Then, the bunches shown in this plot correspond to coincidences between different trials. In the lower plot, we have zoomed around the central peak, corresponding to coincidences detected in the same trial. Here, we can see the characteristic time correlations appearing in dissipative Rydberg EIT systems, where the probability to detect two photons close to each other is strongly suppressed due to dipole blockade (see section 2.4.1). The normalization factor is obtained

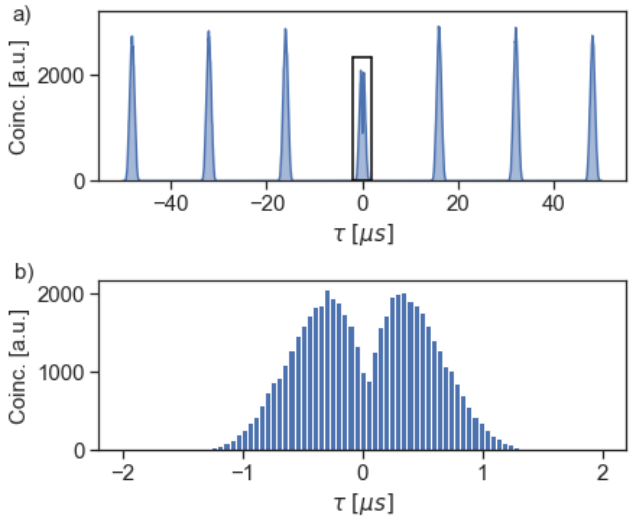

Figure 4.1: Coincidences as a function of the delay time, with a bin size of 50 ns. (a) For $\tau \gg t_{trigger}$. (b) Zoom of the upper plot for $\tau < t_{trigger}$.

either from the number of coincidences between non-correlated trials or directly from the single-photon detection probabilities.

4.3 Starting point

As the starting point of the nonlinearity measurements, we present here the results published in 2017 [83]. In this experiment, a magneto-optical trap was used to load the atoms, leading to a Gaussian distribution of atoms with $\sigma \approx 0.8$ mm and a peak density of $\rho_0 \approx 3.2 \cdot 10^{10}$ cm^{-3}. The atoms were initially prepared in the state $|g\rangle = |5S_{1/2}, F = 2\rangle$. A probe beam resonant with the transition $|g\rangle \rightarrow |e\rangle = |5P_{3/2}, F = 2\rangle$ was

focused in the center of the cloud with a beam waist of $\omega_p \approx 6.5$ μm, giving a OD ≈ 6. A counter-propagating coupling beam resonant with $|e\rangle \rightarrow |r\rangle = |60S_{1/2}\rangle$ was focused with $\omega_c \approx 13$ μm, giving a Rabi frequency of $\Omega_c \approx 5$ MHz, fulfilling the conditions for EIT. The values of OD and Ω_c were extracted from a fit to the transmission for different detuning of the probe light, as previously presented in section 3.5. With these parameters, we can infer a blockade radius of $r_b \approx 6.4$ μm from the equation 2.18.

For the characterization of the nonlinearity, Gaussian-shaped probe pulses were sent with a FWHM ≈ 400 ns, optimized to obtain the highest possible storage efficiency. When the pulse was traveling through the medium, the coupling beam was switched off to perform storage. After a storage time $t_{stor} = 4$ μs, the probe light was retrieved with a maximum efficiency of $\eta_0 = n_{out}/n_{in} \approx 0.005$, measured for $n_{in} \approx 5$ photons, and detected with an avalanche photo-detector. The mean number of output photons, corrected by the linear transmission T, as a function of n_{in}, is shown in figure 4.2. The value of N_{max} obtained from the fit to equation 4.1 shows a nonlinear effect at the level of ~ 60 input photons. This represents the best value obtained before we implemented the next changes in the experiment, described in sections 4.5-4.6.

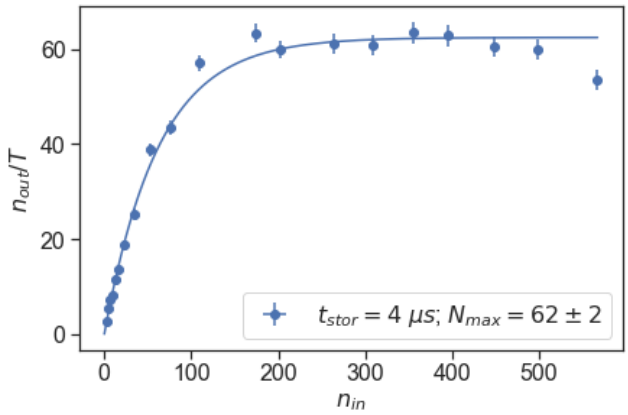

Figure 4.2: Mean number of output photons retrieved after a storage time of 4 μs at $|r\rangle = |60S_{1/2}\rangle$, divided by the linear transmission T, as a function of the mean number of input photons. The saturation level gives $N_{max} = 62 \pm 2$. Error bars correspond to one s.d.

4.4 Parameters to improve

The second-order correlation function of the light after propagation in a Rydberg EIT medium in steady state conditions, i.e. for an uniform input rate of photons, was characterized by Peyronel et al. in 2012 [36]. In their model, they obtain an analytical expression of $g^{(2)}(0)$ from the equations governing the two-particle amplitudes, which are obtained using the Heisenberg equations of motion for the slow-varying operators involved in the creation of a photon, an intermediate state excitation and a Rydberg excitation. In steady state conditions and after several simplifications, the $g^{(2)}(0)$ is:

$$g^{(2)}(0) \approx \frac{4(1+(\Omega_c/\Gamma)^2)}{\pi \mathrm{OD}} exp\left[-\frac{\mathrm{OD}_b}{\sqrt{1+(\Omega_c/\Gamma)^2}}\right], \tag{4.2}$$

where Γ is the decay rate of $|e\rangle$ state and OD_b is the optical depth per blockade sphere, defined as $\mathrm{OD}_b = \mathrm{OD}r_b/L$ for a one-dimensional medium. Among the approximations made to obtain this equation are: neglecting the decay of the $|g\rangle \rightarrow |r\rangle$ coherence, assuming uniform density along the propagation direction, one dimension and large OD. Therefore, although we cannot use it for quantitatively describing our problem, we can use it for qualitatively understanding it. From this equation, we can see that OD_b is a key parameter, since $g^{(2)}(0)$ drops exponentially when $\mathrm{OD}_b^2 > 1+(\Omega_c/\Gamma)^2$. The general OD of the medium also influences, but in a linear way ($\propto 1/\mathrm{OD}$). Note that $g^{(2)}(0)$ also depends on Ω_c, in a way that decreasing it leads to lower $g^{(2)}(0)$. However, for a medium where $\gamma_{rg} \neq 0$, decreasing Ω_c also leads to lower EIT transparency (see equation 2.14 of section 2.4). Therefore, we will work with the greatest value of Ω_c possible, which usually lies between $0.8\Gamma - 1.7\Gamma$.

Having a one-dimensional medium is key to achieve nonlinearity at the single-photon level, since it is related to the probability to find two parallel polaritons. A one-dimensional medium can be assumed if the transversal size of the interaction region is much smaller than r_b at all positions, which is not the case of the experiment presented in section 4.3, due to the huge cloud length. In this case, the previous definition of OD_b as $\mathrm{OD}r_b/L$ is not precise and possibly gives a greater value of the optical depth per blockade sphere. In the following, we will write $\mathrm{OD}_b < ODr_b/L$ for conditions where one-dimensionality

cannot be assumed. From the experimental parameters, we obtain $\mathrm{OD}_b < OD r_b/L \approx 0.048$.

Another parameter that we should consider when we aim for obtaining a single photon located within a pulse is the maximum number of excitations which can be fitted inside the medium. This is specially important when storage is performed. For a general case where the dimension can be greater than one, we can estimate it as $N_b = V_{IR}/r_b^3$, where V_{IR} is the volume of the interaction region. However, for a one-dimensional medium, a better estimation is $N_b = L/r_b$. In an ideal case, $N_b \lesssim 1$. For the initial configuration of the experiment, we infer that the maximum number of excitations which can be stored in the medium is $N_b \sim 3200$.

When storage is performed, interaction-induced dephasing also can play a role in increasing the nonlinearity of the system (see section 2.6). The phase-shift applied to the components with more than one excitation depends on three parameters: the relative distance between excitations, the interaction coefficients ($C_6 \propto n^{11}$ and $C_3 \propto n^4$) and the storage time. Therefore, interaction-induced dephasing will normally increase for higher Rydberg levels and longer storage times.

Therefore, the nonlinearity of the medium depends on several parameters. The improvement of them, specially OD_b and N_b, can be done in several ways, which can be summarized in:

- Exciting to Rydberg levels with higher n: It increases the interaction coefficients and the blockade radius, which also increases the number of atoms per blockade sphere.
- Increasing the density of the cloud: It increases the number of atoms per blockade sphere and hence the OD_b.
- Changing the probe and coupling transitions to one with stronger dipole moment: It increases the light-atom interaction and hence the OD.
- Reducing the transverse size and volume of the interaction region by confining more the atoms.
- Storing for long times.

4.5 Towards stronger nonlinearities

The critical step in the experiment to achieve quantum statistics in the output light was to implement a dipole trap to load the atomic cloud. However, we tried many previous improvements that we present in this section. A summary of the important parameters in each of the steps can be found in the table 4.1.

	n	r_b	OD_b	N_{max}^{slow}	N_b	t_{stor}	N_{max}^{stor}
Starting point	60	6.4 μm	< 0.048	*	3200	4 μs	60
CMOT	60	6.2 μm	< 0.16	*	680	*	*
Transitions	60	6.2 μm	< 0.27	*	680	3 μs	10
Rydberg state	70	8 μm	< 0.34	*	320	3 μs	4
Optical pumping	70	8 μm	< 0.5	10	320	2 μs	3

Table 4.1: Summary of improvements made to the experiment before the dipole trap and the important parameters in each step. * indicates that no data is available. All values are approximations.

4.5.1 Compressed-magneto-optical trap (CMOT)

In order to increase the density of the atoms and decreasing the number of blockade spheres in the medium, we implemented a compressed magneto-optical trap, described in section 3.4.2. From fluorescence imaging, we estimated a peak density of $\rho \approx 6 \cdot 10^{10}$ cm^{-3} and a cloud size of $\sigma \approx 0.3$ mm.

After the implementation of the CMOT, we measured OD ≈ 16 and $\Omega_c \approx 5.5$ MHz. For the same Rydberg state $|r\rangle = |60S_{1/2}\rangle$, these parameters lead to $r_b \approx 6.2$ μm, $\mathrm{OD}_b < 0.16$ and $N_b \sim 680$.

4.5.2 Transitions

In order to increase the light-matter coupling, we also changed the transitions used in the experiment to ones with higher dipole moments. The probe, before connected with the intermediate state $|e\rangle = |5P_{3/2}, F = 2\rangle$, is now coupled with $|e\rangle = |5P_{3/2}, F = 3\rangle$. This new transition means an ideal gain in the $|g\rangle \rightarrow |r\rangle$ excitation probability of 4.7, assuming an equally-distributed population in the different Zeeman levels of the

ground state.

Experimentally, we obtained an OD ≈ 26 and $\Omega_c \approx 5.5$ MHz. Hence, the maximum bound of the OD_b was increased to $\text{OD}_b < 0.27$. At this point, we measured a $N_{max} \sim 10$ for a storage time $t_{stor} = 3$ μs. However, we obtained a second-order correlation function of $g^{(2)}(0) \approx 1$, showing no quantum statistics.

4.5.3 Change of Rydberg level

In order to increase the volume of the blockade sphere, we changed the excitation to a higher Rydberg level, specifically $|r\rangle = |70S_{1/2}\rangle$. Given the previous value of OD and a coupling Rabi frequency of $\Omega_c \approx 6.5$ MHz, the blockade radius is $r_b \approx 8$ μm, which leads to $\text{OD}_b < 0.34$ and $N_b \sim 320$. For this experiment status, we measured $N_{max} = 4 \pm 1$ for a storage time of $t_{stor} = 3$ μs. However, no quantum statistic was obtained in a second-order correlation measurement.

4.5.4 Optical pumping

Another step towards increasing the light-matter coupling was to optically-pump the atoms in the Zeeman level $|g\rangle = |5S_{1/2}, F = 2, m_F = 2\rangle$, since the transition $|5S_{1/2}, F = 2, m_F = 2\rangle \rightarrow |5P_{3/2}, F = 3, m_F = 3\rangle \rightarrow |r\rangle$ has the strongest dipole moment. In the ideal case, we expect a gain in the excitation probability of 14, comparing to the starting configuration with $|e\rangle = |5P_{3/2}, F = 2\rangle$, assuming an equally-distributed population in the Zeeman levels of the ground state.

After the implementation and optimization of the optical pumping, we measured OD ~ 40 and $\Omega_c \approx 6.5$ MHz, which leads to $\text{OD}_b < 0.5$. The characterization of the nonlinearity at this stage is shown in the next section.

4.5.5 Final results

The resulting nonlinearity of the system was characterized following the two methods described in section 4.2, i.e. by measuring the saturation level of output photons N_{max} and the second-order correlation function $g^{(2)}(\tau)$.

N_{max} measurement is shown in figure 4.3, for different storage times. We can see that the obtained values for N_{max} are more than ten times smaller than the ones obtained at the beginning (see figure 4.2), being very close to the values expected for the quantum regime. Moreover, this measurement indicates that, although the difference in N_{max} between the different storage times is in most cases inside the error bars, this difference is significant when we compare to the one obtained with slow light, corresponding to $t_{stor} = 0$ and square markers in the plot. In the top, the efficiency of the storage process is characterized for a low number of input photons ($n_{in} \approx 3$ photons), such that we can consider than the dephasing time (the characteristic time in which the retrieval efficiency decreases) is limited by atomic motion and not by Rydberg interactions. In this case, the retrieval efficiency follows a Gaussian decay with a lifetime given by the temperature of our atomic cloud [126]. A Gaussian fit to the data gives $\tau \approx 1.3$ μs. Note that the first point correspond to the slow light efficiency, so it is not included in the fit.

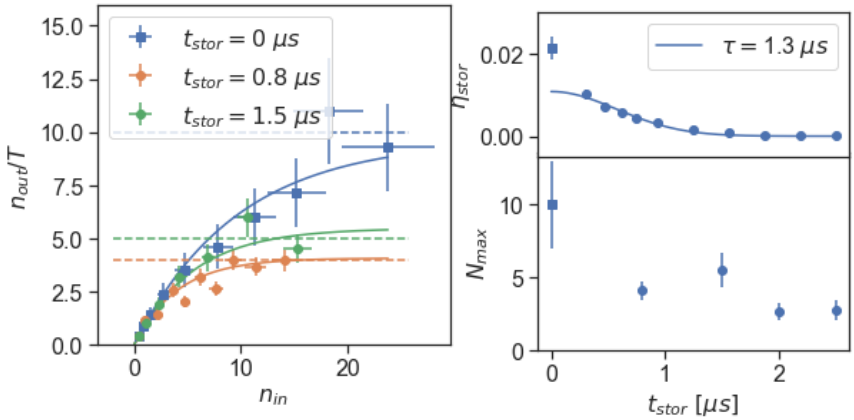

Figure 4.3: In the left, mean number of output photons, corrected by the linear transmission, as a function of the mean number of input photons, for three different storage times. In the top right, the storage efficiency for different storage times and the resulting dephasing time extracted from a Gaussian fit without including the slow light efficiency. In the bottom, N_{max} as a function of the storage time. Square marker and $t_{stor} = 0$ corresponds to slow light measurement. Error bars correspond to one s.d.

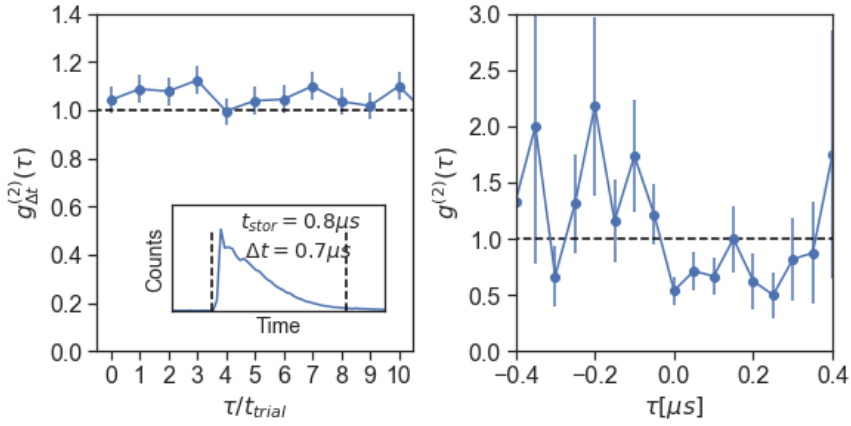

Figure 4.4: In the left, $g^{(2)}_{\Delta t}(\tau)$ between different trials, after storing the pulse for $t_{stor} = 0.8$ μs. The detection window of $\Delta t = 0.7$ μs is shown in the inset plot. The time between trials is $t_{trial} = 10.2$ μs. In the right, $g^{(2)}(\tau)$ for delay times τ between two photon events happening in the same trial, for $t_{stor} = 0.8$ μs and a bin size of 50 ns. The black dashed line indicates the classical threshold. Errors correspond to one s.d.

The measurement of the second-order correlation function of the output pulse for $t_{stor} = 0.8$ μs and $n_{in} \approx 4$ photons is shown in figure 4.4. In the left, we select a window time of $\Delta t = 0.7$ μs to take into account all the photon events arriving inside the retrieved pulse (see inset). Then, we measure the probability to have a coincidence between different trials. This value is then normalized by the classical one given by the single-photon detection probabilities $\langle n_1 \rangle \langle n_2 \rangle$ within the time window Δt, leading to $g^{(2)}_{\Delta t}(\tau)$. The value obtained within the same trial (first column) gives $g^{(2)}_{\Delta t}(0) = 1.04 \pm 0.06$, which is still classical. In the plot on the right, we show a time-resolved measurement of the $g^{(2)}(\tau)$ by taking different τ within the same trial and a bin size of $2\Delta t = 50$ ns. In this case, the classical coincidences are measured from the coincidences between one trial and the next one. At zero-delay time, we obtain a value of $g^{(2)}(0) = 0.54 \pm 0.13$, which is in the quantum regime. However, the magnitude of error bars and bin size does not allow us to see a clear antibunching dip.

We also measure the variation in the statistics of the output pulse, after a storage time of $t_{stor} = 0.8$ μs, with respect to the mean number

of input photons. Results are shown in figure 4.5 for a $\Delta t = 0.7$ μs longer than the retrieved pulse (see inset plot). For $n_{in} \gg 1$, we measure correlation between one trial and the following ones, characterized by a bunching effect lasting until the 4^{th} next trial, which correspond to a delay time between two detections of 40.8 μs. A clear understanding of this effect is difficult, since the regime of $n_{in} \gg 1$ constitutes a challenging many-body dissipative problem. A possible explanation arrives from nearly-stationary Rydberg excitations which cannot be retrieved from the cloud from one trial to another (pollutants) [102, 50]. They can be located out of the interaction region or in another Rydberg state and are more likely to be created for $n_{in} \gg 1$. The pollutants generated in one trial can blockade the storage of photons in the following trials, giving rise to long-lived correlations as the ones shown in figure 4.5.

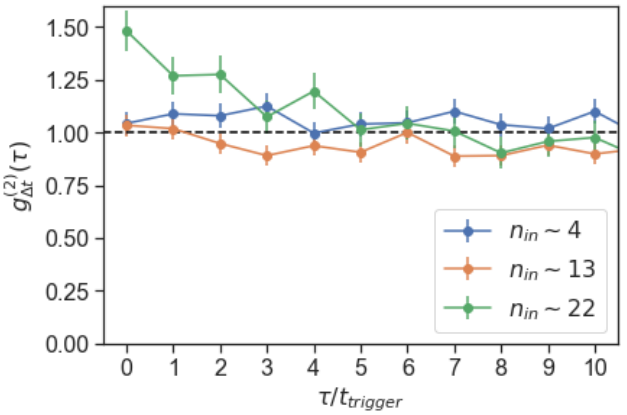

Figure 4.5: Second-order correlation function between trials, for different mean number of input photons n_{in}. The values for the same pulse are: $g^{(2)}_{\Delta t}(0) = 1.04 \pm 0.06$ for $n_{in} \sim 4$, $g^{(2)}_{\Delta t}(0) = 1.03 \pm 0.05$ for $n_{in} \sim 13$ and $g^{(2)}_{\Delta t}(0) = 1.48 \pm 0.09$ for $n_{in} \sim 22$. The black dashed line indicates the classical threshold. Errors correspond to one s.d.

The results presented here show that the obtained nonlinearity at this stage was not high enough to see clear quantum statistics in the output light. Moreover, the count rate of the experiment was very low: around 990 trials/s and 6 counts/s in each detector, giving < 150 coincidences/hour. The slow light and storage efficiency were also quite low: $\eta_{slow} \approx 0.02$ and $\eta_{stor} \approx 0.007$ for $t_{stor} = 0.8$ μs.

4.6 Nonlinearity with the dipole trap

In order to increase the nonlinearity of the medium, we implemented a dipole trap to load a smaller and denser atomic cloud, consisting of a red-detuned laser beam at 852 nm highly focused in the center of the atomic cloud. The resulting cloud had a transversal size of 34 μm and a peak density of $\sim 4{\cdot}10^{11}$ cm^{-3}. In the following experiments, no Zeeman optical pumping was performed, so the atoms were prepared in the state $|g\rangle = |5S_{1/2}, F = 2\rangle$. The probe beam was sent with an angle of 19^o with respect to the dipole trap beam (see figure 3.5b of section 3.4.4) and resonantly coupled to the state $|e\rangle = |5P_{3/2}, F = 3\rangle$, leading OD $\sim 5-7$.

4.6.1 Change of Rydberg level

In the following measurements, we excite the atoms to three different Rydberg states $|r\rangle = |nS_{1/2}, F = 2\rangle$ with $n = 70, 81, 90$. The coupling Rabi frequencies, obtained from a fit to the EIT transparency, are $\Omega_c \approx 10, 9.5, 7$ MHz for the different states, respectively. The key parameters calculated for these conditions are shown in the table 4.2.

n	r_b	One dimension	OD$_b$	N_b
70	7 μm	$r_b \ll 2\omega_p$	< 0.4	$\sim$14
81	9.3 μm	$r_b < 2\omega_p$	$\lesssim 0.5$	$\sim$6
90	12.7 μm	$r_b \sim 2\omega_p$	~ 0.7	$\sim$2-3

Table 4.2: Key parameters to characterize the nonlinearity after implementing the dipole trap, for three different Rydberg states. All the values are approximations calculated for a medium with OD= 6 and effective length $L = 104$ μm, where $L = 34/\sin(19^o)$ μm takes into account the angle between the dipole trap and the probe beam, whose waist is $\omega_p \approx 6.5$ μm.

4.6.2 Final results

With these parameters, we finally obtained quantum statistics in the output pulses, when measuring the second-order correlation function. The following measurements were obtained for Gaussian input pulses with $n_{in} \lesssim 2$ photons and FWHM$\approx$ 200 ns, unless we specify another

values.

The values of N_{max} and $g^{(2)}_{\Delta t}(0)$, after propagation under EIT and after storing for 0.5 μs are shown in figure 4.6, for the three different principal quantum numbers $n = 70, 81, 90$ and $n_{in} \lesssim 1.5$. As we can see, the higher the n, the closer to the single-photon statistics ($g^{(2)}_{\Delta t}(0) = 0$), although the values of N_{max} does not show any clear dependence. This indicates, as we have suspected from previous measurements, that N_{max} is a good indicator of the nonlinearity only for weakly-blockaded ensembles. However, it is not sufficient when the nonlinearity approaches to the single-photon regime.

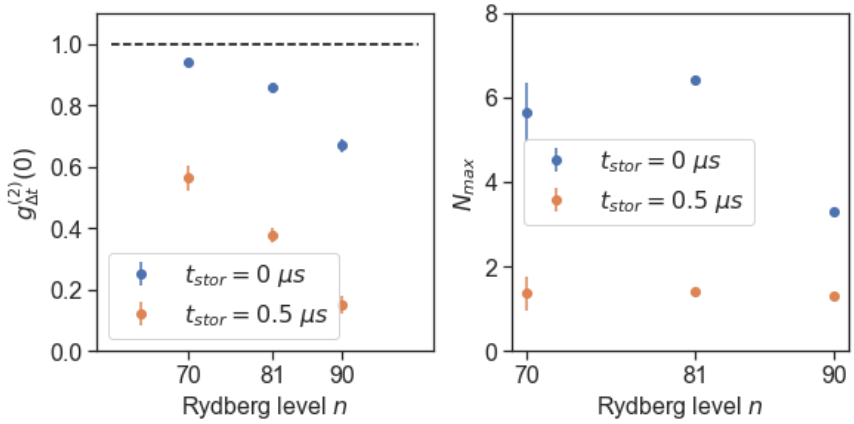

Figure 4.6: In the left, second-order correlation function $g^{(2)}_{\Delta t}(0)$ with respect to the principal quantum number of the Rydberg state, for a pulse after propagating through EIT ($t_{stor} = 0$) and after being stored for $t_{stor} = 0.5\ \mu s$. The black dashed line indicates the classical limit. In the right, N_{max} obtained for the same parameters does not show a clear correlation. Error bars correspond to one s.d. In the N_{max} measurement, systematic errors associated to the detection efficiency are also included.

An analysis of the second-order correlation function for delay times within the same pulse is shown in figure 4.7, for a bin size of $2\Delta t = 30$ ns. In the left, $g^{(2)}(\tau)$ is measured for pulses after propagation under EIT (slow light case), for the three different Rydberg states. The values at zero-delay time gives $g^{(2)}(0) = 0.84 \pm 0.03$ for $n = 70$, $g^{(2)}(0) = 0.69 \pm 0.03$ for $n = 81$ and $g^{(2)}(0) = 0.45 \pm 0.05$ for $n = 90$. Note that

these values are much higher than what we expect from the equation 4.2 ($g^{(2)}(0) \lesssim 0.1$ for $n = 90$) and are instead more similar to e^{-OD_b}, which can be due to the strong assumptions of the equation. In the right plot of figure 4.7, we show $g^{(2)}(\tau)$ for different storage times in the state $|r\rangle = |81S_{1/2}\rangle$. Although for $t_{stor} = 0$, we can see a clear dependence with τ, leading to an antibunching dip, this is not the case for a retrieved pulse after storage, where we see a $g^{(2)}(\tau)$ roughly constant with τ. The absence of clear time correlations means that two photons detected within the same pulse have the same probability to be retrieved at the same time ($\tau = 0$) than with a delay time of $\tau \approx 0.2$ μs. This may suggest that the limitation in the nonlinearity is given by the fact that the medium is not one-dimensional. Moreover, since the probability to detect two photons is low for the whole pulse duration, we can say that the output single photon is localized within a pulse. The values obtained for zero-delay time are $g^{(2)}(0) = 0.44 \pm 0.04$ for $t_{stor} = 0.2$ μs and $g^{(2)}(0) = 0.34 \pm 0.04$ for $t_{stor} = 0.5$ μs. Note that the slow light measurement is the same as the one shown in the left plot.

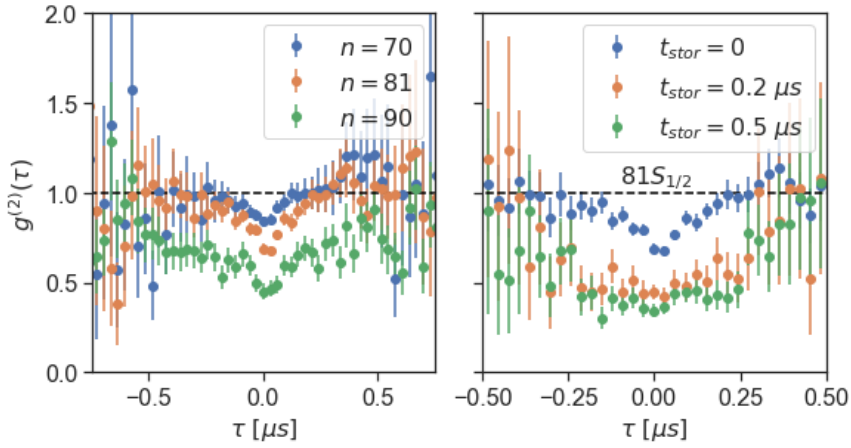

Figure 4.7: Second-order correlation function with respect to the delay time between two-photon events τ, with a bin size of 30 ns. In the left, $g^{(2)}(\tau)$ for slow light, for three different Rydberg states with $n = 70, 81, 90$. In the right, $g^{(2)}(\tau)$ after storage in the state $|81S_{1/2}\rangle$ for different t_{stor}. The black dashed line indicates the classical threshold. Error bars correspond to one s.d.

In figure 4.8, we characterize the statistics of the full pulse, i.e.

$g^{(2)}_{\Delta t}(0)$, after storing for different times. We can see that, although the change in the statistics between the case with $t_{stor} = 0$ and the cases with $t_{stor} > 0$ is evident, the difference between the different storage times is not so clear. This is in contrast with previous results obtained with atoms loaded in the magneto-optical trap [122], where there was a clear dependence with the storage time. This could be explained if we consider that the interaction-induced dephasing is stronger when there are more excitations in the cloud. The dispersion of the points suggests changes in the experimental conditions during the hours-long measurements. In the right, we show the storage efficiency for the different storage times and the dephasing time obtained from a Gaussian fit to this data.

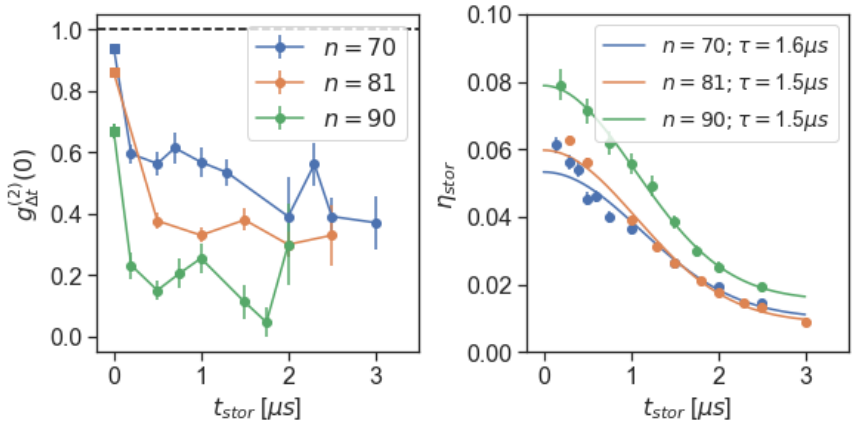

Figure 4.8: In the left, $g^{(2)}_{\Delta t}(0)$ of the whole output pulse with respect to the storage time, for different Rydberg states. The black dashed line indicates the classical threshold. At the right, storage efficiency as a function of storage time for the different Rydberg states. A Gaussian fit to the data is also shown, with the extracted dephasing time. Errors correspond to one s.d.

In figure 4.9, we show $g^{(2)}_{\Delta t}(0)$ as a function of the mean number of input photons n_{in}, for the three different principal quantum numbers $n = 70, 81, 90$, after 0.5 μs of storage time. We can see that the quantum statistics of the output photons becomes classical when $n_{in} \gg 1$. This bunching effect for higher n_{in} was also demonstrated for the case of a bigger cloud in figure 4.5. As we said in the previous case, this might

be explained by the creation of pollutants [102], even though it might also be explained by an increase in the two-excitations component, since we can store more than one photon in the cloud ($N_b > 1$).

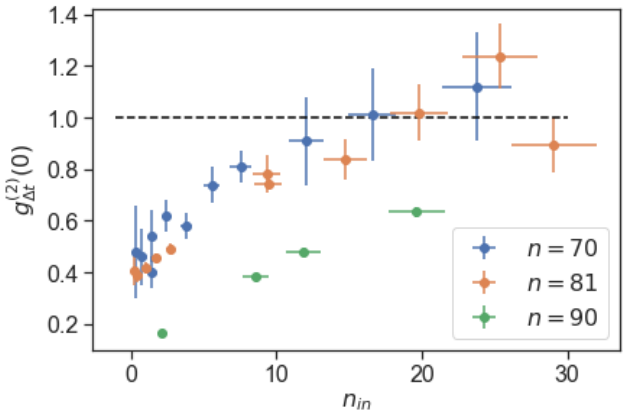

Figure 4.9: Second-order correlation function with respect to the approximated mean number of input photons, for different Rydberg states and after 0.5 μs of storage time. The black dashed line indicates the classical threshold. Error bars correspond to one s.d.

Besides the improvements in the statistics of the output photons, an increase in the experiment rate was also achieved after the implementation of the dipole trap, leading to $\sim$ 5730 trials/s. The slow light and storage efficiencies also increased, as we can see from figure 4.8, obtaining $\eta_{slow} \sim 0.5$ and $\eta_{stor} \sim 0.06$ for $t_{stor} = 0.5$ μs. Furthermore, for $t_{stor} = 0.5$ μs, we measured an average of 30 counts/s arriving to each detector, leading to $>$ 500 coincidences/hour.

4.7 Conclusion

Since the beginning of my PhD, several changes have been implemented to the experiment, leading to an increase in the nonlinearity of the medium, the light-matter coupling and the duty cycle and count rates of the experiment. The most important step was the implementation of the dipole trap, which strongly reduced the size of the atomic cloud and increased its density. Afterwards, the second-order correlation measurement of light after propagation or storage in a Rydberg EIT system was

in the quantum regime, witnessed by second-order correlation function measurements with $g^{(2)}(0) \ll 1$.

Chapter 5

Propagation dynamics of Rydberg polaritons

5.1 Introduction

As we have shown before, an ensemble of cold atoms coupled to Rydberg states by means of EIT provides an efficient light-matter interface, which allows the long-range spatial correlations between Rydberg polaritons to be mapped into time correlations of the transmitted light. In section 2.4.1 and 4.4, we have seen that OD_b plays a very important role in creating the strong nonlinearity in the slow light case [36], since it is related to the probability to detect a blockaded photon. However, reaching high values of OD_b is experimentally challenging to achieve, as it requires a high atomic density and very high Rydberg levels. Furthermore, achieving a single photon localized within a pulse, that is, reaching low values of the second-order correlation function for the entire pulse, requires compressing it ideally within a blockade sphere 2.4.1. We have shown in section 4.6.2 that single localized photons can be created by storing the light as Rydberg excitations which are later retrieved from the medium. However, the use of transmitted pulses (without storage) in Rydberg EIT could therefore potentially lead to the generation of localized single photons with higher efficiencies.

In this chapter, we study the photon statistics of weak coherent pulses propagating through Rydberg EIT. We show experimentally that the value of the second-order correlation function of the transmitted light strongly depends on the position within the pulse. In particular,

we show that the falling edge of the transmitted pulse displays much lower values than the rest of the pulse. Recently, similar results were observed by Möhl et al. [144]. Our theoretician colleagues Dr. Roberto Tricarico and Prof. Darrick Chang at ICFO derived a theoretical model which explains qualitatively our results. Finally, we used this effect to generate single photons from the atomic ensemble. We show that by selecting only the last part of the transmitted pulse, we could generate single photons localized within a part of the pulse with an antibunching parameter as low as 0.12 ± 0.05 and with a generation efficiency per trial larger than what it is possible with probabilistic generation schemes with atomic ensembles. We compare these results with single photons created by storing the light as Rydberg excitations which are later retrieved from the medium.

The main results of this chapter are described in the scientific article [145] and therefore a large part of the chapter has been taken from it.

5.2 Experiment

The atoms are loaded in the dipole trap, modulated with a period of 16 μs, which leaves a time of less than 8 μs to perform one experimental trial. This is repeated 13000 times during the dipole trap lifetime, which gives a total experimental rate of 5730 trials/s.

Atoms are excited to the Rydberg state $|r\rangle = |90S_{1/2}\rangle$ (fig. 5.1a) and the probe light propagates through the medium with an OD ≈ 10. Figure 5.1b shows the EIT transparency window of our cloud, for an input photon rate $R_{in} \approx 0.3$ MHz. The EIT width and coupling Rabi frequency obtained from a fit to the data are 2.3 MHz and 6.4 MHz, respectively. These parameters give a group velocity $v_{gr} \sim 200$ μm/μs of propagating Rydberg polaritons (see equation 2.17), much smaller than the velocity of light in vacuum c. That means that polaritons take $\mathrm{L}/v_{gr} \sim 0.5$ μs to go throughout the atomic cloud. The average number of input photons in the medium at a time results $\sim 0.2 \ll 1$, so no interaction effects are expected to dominate the transparency. As the blockade radius is $r_b \approx 13$ μm for our experimental parameters (see equation 2.18), the parallel propagation of two polaritons in our atomic cloud is unlikely. With these parameters, the optical depth per blockade radius is $\mathrm{OD}_b \approx 1.2$.

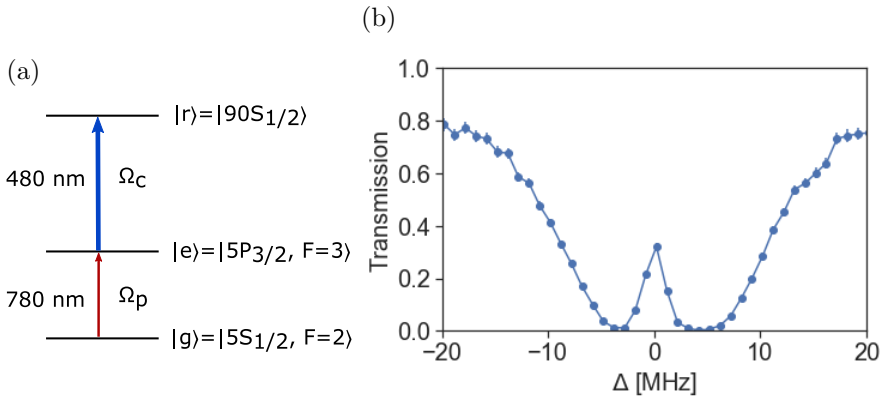

Figure 5.1: Level scheme and transitions used in the experiment and EIT transparency window.

The statistics of the light is obtained by measuring the second-order correlation function $g^{(2)}(t,\tau)$, defined in equation 2.7 of section 2.2. This is done by sending the output pulses through a Hanbury Brown and Twiss setup (see figure 2.5). The value of $g^{(2)}(t,\tau)$ is hence obtained from equation 2.10 by taking into account the detection clicks inside a window of duration Δt starting at a time t_0 after the trial trigger.

5.3 Second-order correlation of the entire pulse

In this section, we study the photon statistics of a square pulse with a mean number of photons $n_{in} \approx 1.5$ and a temporal length of 1 μs, after propagation through the Rydberg medium. In figure 5.2a, we can see the temporal shape of the input and output pulses, showing a transmission of T$= n_{out}/n_{in} = 0.285 \pm 0.016$, where $n_{out(in)}$ is the total number of clicks in the output(input) pulse. The transmission efficiency from the ensemble to the first detector is 0.23 ± 0.02, taking into account all the optical elements, and the SPAD_1 detection efficiency is 0.43 ± 0.04.

First, we consider the counts arriving in a time window of $\Delta t = 1.6$ μs, sufficiently large to include the whole output pulse, as shown in figure 5.2b. In figure 5.3a, we show the $g^{(2)}_{\Delta t}(\tau)$ for different trials, where

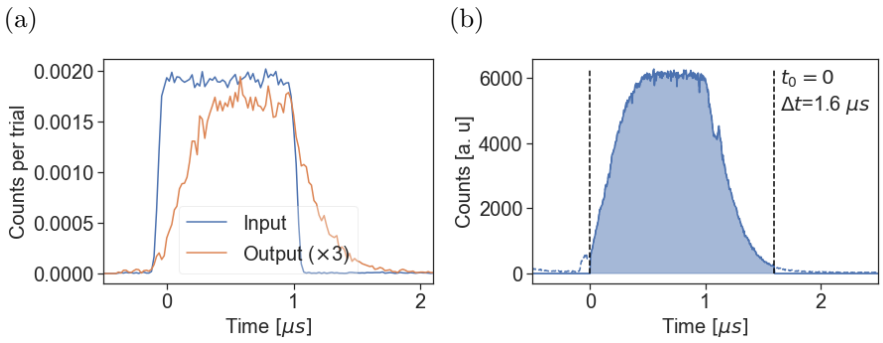

Figure 5.2: (a) Counts per trial arriving to the first detector, as a function of time after trigger (the trigger time is made 0 at the beginning of the output pulse), for a bin size of 20 ns, for the input (in blue) and output pulse (in orange). The temporal distribution of the input pulse is taken from the counts detected without loading the atomic cloud. (b) Temporal window of data analysis, with $t_0 = 0$ and $\Delta t = 1.6$ μs. The total temporal distribution is shown in dashed line.

the coincidence histogram is normalized by the coincidences measured between pulses distant at least 80 μs, where no correlation is observed. The bunching shown between close trials might be explained by the creation of long-lived pollutants, which are Rydberg excitations that cannot be retrieved from one trial to another and blockade the creation of the following Rydberg excitations [102, 50]. These pollutants can be atoms that have decayed to nearby Rydberg states or Rydberg atoms that have moved outside the coupling beam. The value obtained for $n_{trial} = 0$ leads a second-order correlation function of the entire pulse of $g^{(2)}_{\Delta t}(0) = 0.908 \pm 0.004$. This shows that while the full output pulse displays non-classical statistic, it is far from being a single photon. Note that the temporal width of the output pulse corresponds to a spatial width during propagation of $v_{gr} \cdot 1$ $\mu s \sim 200$ μm, much longer than the blockade radius. In figure 5.3b, we show a time-resolved $g^{(2)}(\tau)$ for a bin size of $2\Delta t = 10$ ns. For $\tau = 0$, we obtain $g^{(2)}(0) = 0.31 \pm 0.03$, demonstrating a strong antibunching, as shown previously by Peyronel et al. [36]. We see that $g^{(2)}(\tau)$ quickly increases to 1 for $\tau \geq 350$ ns, much shorter than the pulse duration. This increase is attributed to the fact that the propagating pulse is not compressed inside a blockade radius. The fact that this time is slightly longer than the expected blockade

time ($\tau_b = r_b/v_{gr} \sim 0.1\ \mu$s) may be due to diffusion during propagation, caused by the limited spectral width of the EIT transparency window [36]. Hence, we can intuitively conclude that we generate several photons per trial (figure 5.3a) with a minimum time separation between them (figure 5.3b). However, for applications in quantum communication, a single-photon source should generate single photons localized within a specific time interval.

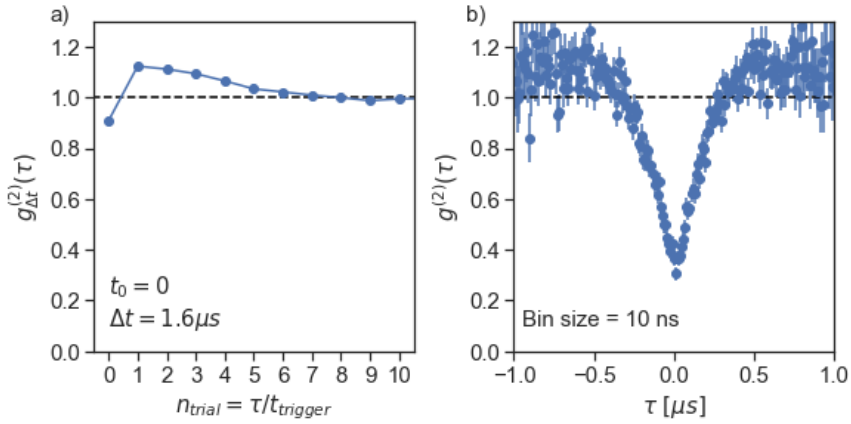

Figure 5.3: (a) $g^{(2)}_{\Delta t}(\tau)$, as a function of n_{trial}, where $\tau = n_{trial} \cdot t_{trigger}$ and $t_{trigger} = 16\ \mu$s. The value at $n_{trial} = 0$ gives $g^{(2)}_{\Delta t}(0) = 0.908 \pm 0.004$, which represents a measurement of the whole pulse statistics. (b) $g^{(2)}(\tau)$ as a function of the delay time τ between two photon events at the same trial, being the one at zero-delay time $g^{(2)}(0) = 0.31 \pm 0.03$. The bin size is 10 ns. Error bars in the plots correspond to one standard deviation (s.d.)

5.4 Second-order correlation function throughout the pulse: Transients

In order to understand better the statistics of the output photons, we perform a more detailed study of the second-order correlation function. We take a detection window with $t_0^{(1)} = t_0^{(2)} = t_0$ and Δt shorter than the pulse duration but longer than the required one used for a time-resolved measurement. Then, we calculate the second-order correlation function

at zero-delay time for different starting times t_0 along the pulse. In this chapter, $g^{(2)}(t_0, 0)$ is labeled as $g^{(2)}_{\Delta t}(t_0)$ from now on. If the photons are completely delocalized within the whole output pulse, we expect a constant $g^{(2)}_{\Delta t}(t_0)$ over t_0.

A measurement for $\Delta t = 200$ ns is shown in figure 5.4. We find that the second-order correlation function is not constant throughout the pulse duration, but decreases towards the end of the pulse. We observe three different regimes. For early times ($t_0 < 0.4\ \mu s$), a first transient is observed, exhibited by a decrease in the $g^{(2)}_{\Delta t}(t_0)$ while the output intensity increases over time. We measure $g^{(2)}_{\Delta t}(t_0) = 0.8 \pm 0.1$ for $t_0 = 0$ and $g^{(2)}_{\Delta t}(t_0) = 0.53 \pm 0.02$ for $t_0 = 0.3\ \mu$s. In the steady-state region ($0.4\ \mu s < t_0 < 1\ \mu s$), both the $g^{(2)}_{\Delta t}(t_0)$ and the output intensity are constant over time. When the input pulse is switched off ($t_0 > 1\ \mu s$), a second transient is observed. Although a decrease in the output intensity is expected, $g^{(2)}_{\Delta t}(t_0)$ follows the same behavior in the same time range, decreasing until reaching a value as low as $g^{(2)}_{\Delta t}(t_0) = 0.12 \pm 0.05$ for $t_0 = 1.4\ \mu$s. These changes of $g^{(2)}_{\Delta t}(t_0)$ along the pulse correspond to three different regimes during the propagation of Rydberg polaritons, as we will describe in the following section.

5.5 Theoretical explanation of transients

A theoretical model with a quantitative explanation of these results has been developed by Dr. Roberto Tricarico and Prof. Darrick Chang. It is a numerical "spin model" that takes advantage of the fact that the output field does not depend on the total number of atoms or on the coupling efficiency of one atom to the probe mode separately, and therefore it is possible to investigate an artificial, quasi-one-dimensional system of a much smaller, tractable number of atoms with a greater coupling efficiency to the probe, while maintaining the same OD, OD_b of the experiment. For a more detailed description, refer to the scientific article [145].

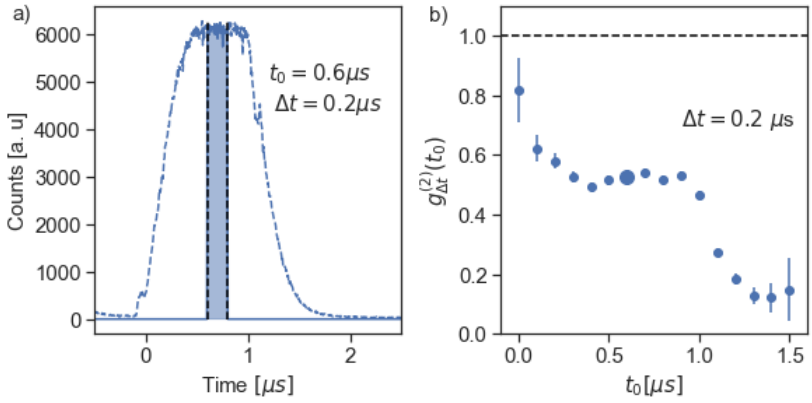

Figure 5.4: (a) Photon counts of $SPAD_1$ as a function of the arrival time with respect to the trial trigger. The temporal window is an example with $t_0 = 0.6$ and $\Delta t = 0.2\ \mu s$. Dashed line corresponds to the total pulse distribution. (b) $g^{(2)}_{\Delta t}(t_0)$ as a function of the window starting time t_0. The highlighted point correspond to the example in the left. The error bars are given by one s.d.

5.5.1 Second-order correlation function in the steady-state regime

In a simple picture of the steady-state region, photons separated by more than a blockade radius propagate in a three-level system as Rydberg polaritons. However, photons closer than a blockade radius to a Rydberg polariton interact with a two-level system and are therefore affected by absorption. However, there is a small part of photons propagating in a two-level system that does get transmitted, due to limited OD_b. In the steady-state region, these two kinds of photons are indistinguishable since they are delocalized in space-time. However, their mutual spatial correlations are mapped into time correlations, which are described by $g^{(2)}(\tau)$ [36].

If the time interval for the data acquisition Δt is smaller than the blockade time τ_b, only one polariton can be detected within this region, so the two-photon events will mainly correspond to the case where one photon has interacted with a three level medium and the other with a two level medium. Therefore, the probability of a two-photon detection is related to e^{-OD_b}. Note that this is a very simplistic model, as $g^{(2)}(0)$

actually depends on more parameters, as previously studied by Peyronel et al. in the regime of OD$\gg 1$ and one-dimensional medium (see equation 4.2) [36]. However, this simple picture is useful to show that the value of Δt influences in the measured $g^{(2)}_{\Delta t}(t_0)$, since it delimits the time range where looking for time correlations in two-photon events. That is to say, all the photons with a time delay $-\Delta t < \tau < \Delta t$ contribute to the measured $g^{(2)}(0)$. Hence, as Δt decreases, the measured $g^{(2)}_{\Delta t}(t_0)$ also decreases. This behavior is shown in the inset of figure 5.6.

5.5.2 First transient

As mentioned before, in the steady-state regime, photons retrieved from Rydberg polaritons are indistinguishable from the ones interacting with a two-level system due to Rydberg blockade. However, when the input probe field is abruptly switched on, we expect photons that propagate as Rydberg polaritons to have a group velocity $v_{gr} \ll c$ and leave the medium in a characteristic time given by L/v_{gr}, where L is the medium length.

To further understand the behavior, it is convenient to utilize an input-output relation, which express the output field operator as a sum of the input field and the field re-emitted by the atoms. In the model, the decay rate of the excited state Γ_{eg} is decomposed into the sum of Γ_{1D}, which is the emission rate into the Gaussian mode defined by the probe beam, and Γ', which is the decay rate into noncollectable directions and represents the losses. Then, the input-output relation takes the form:

$$E(t) = E_p(t) - i\sqrt{\frac{\Gamma_{1D}}{2}} \sum_{h=1}^{N} e^{ik_p z_h} \sigma^h_{ge}, \tag{5.1}$$

where $E_p(t)$ is the input probe field at time t, k_p is the probe wavevector, $\sigma^h_{ge} = |g\rangle \langle e_h|$ is the atomic lowering operator of the atom h and z_h is the position of atom h.

Right after the turn-on, there is no population in the $|e\rangle$ and $|r\rangle$ states and, since the atomic properties must evolve continuously, the action of σ^h_{ge} on the state immediately after the turn-on of the pulse is zero. From equation 5.1, this implies that the output field is the same as the input field immediately after turn-on and therefore the output pulse should give the same statistics as the input pulse $g^{(2)}(0) = 1$. This

evolves until the population in the Rydberg state reaches the steady-state value, which occurs at a time L/v_{gr}.

For our experimental conditions, we calculate $L/v_{gr} \sim 0.5$ μs, which is in good agreement with the duration of the first transient ~ 400 ns. Note that this also explain the time it takes for the output intensity to reach its maximum value.

5.5.3 Second transient

When the input probe field is abruptly switched off, the retrieval of photons from Rydberg polaritons is physically equivalent to the retrieval after storage. These photons can then be localized in time, since they leave the medium in a time scale L/v_{gr}, much longer than what it takes for photons interacting with a two-level system, which configure the two-photon events, to leave the medium. Therefore, the characteristic time of this transient should also be related to L/v_{gr}.

In figure 5.5, we show the measured $g^{(2)}_{\Delta t}(t_0)$ as a function of the starting time t_0, together with the temporal distribution of the input and output pulses. The green shadowed region shows times where no probe photons are entering the medium, which correspond to times where $g^{(2)}_{\Delta t}(t_0)$ is strongly reduced. We can see that the duration of the second transient is $\sim 0.4 - 0.5$ μs, as we expect. Note that this is a very simple picture. For better understanding of the different time scales involved in the first and second transient regime, see Dr. Roberto Tricarico's work.

Using the input-output relation of equation 5.1, we can see that the outgoing field at a time immediately following the shutoff will only be due to purely atomic emission and jump discontinuously from its value immediately before. Since under ideal EIT conditions, the $|e\rangle$ state is unpopulated, the atoms are not able to emit light instantaneously and the output intensity should be zero immediately after the shutoff. Regarding to the two-photon intensity, its value before the shutoff is close to zero due to the Rydberg blockade. This can be understood as a destructive interference between the incoming field and the field re-emited by the atoms. Therefore, if the input field is instantly extinguished, the two-photon outgoing intensity is due to a purely atomic emission which, for large OD, is almost equal in amplitude (but opposite in phase) to the incoming field. Since the single-photon output intensity is zero, this re-

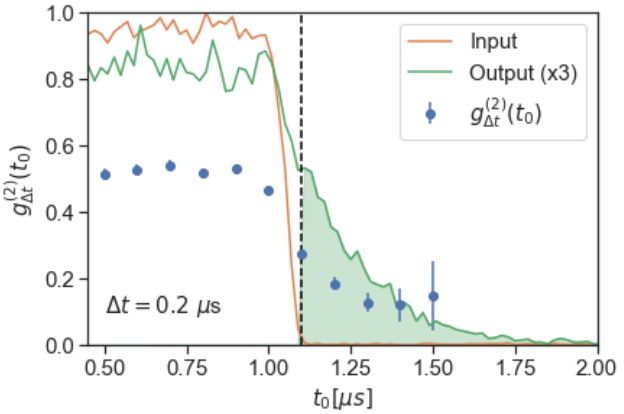

Figure 5.5: $g^{(2)}_{\Delta t}(t_0)$ as a function of the starting time t_0 (in blue) and input (orange) and output (green) pulse shapes, as a function of the arrival times to the first detector. The output counts are multiplied by a factor 3 and normalized to the maximum value of input counts. The green shadowed region correspond to times where no probe photons are entering the medium, which corresponds to a decrease in $g^{(2)}_{\Delta t}(t_0)$. Error bars correspond to one s.d.

sults in photon bunching with $g^{(2)}(0) \gg 1$ immediately after the shutoff. However, the flash of bunched output light can be seen only if the time scale of the shutoff is much faster than the time needed by the atoms to react, which is roughly Γ_{eg}^{-1}. Unfortunately, this is not our case. The results of the theoretical model for our experimental conditions is shown in figure 5.6.

5.6 Comparison with different shapes of the input pulse

To show the dependence of these transients with the shape of the input pulse, we study the propagation of triangular pulses (see figure 5.7), following the same method described above. For this measurement, OD $\approx$ 5.8 and $\Omega_c \approx$ 6.2 MHz. In the case of a triangular shape with a negative slope (figure 5.7a), the probe field is switched on abruptly but slowly switched off. Here, we observe that $g^{(2)}_{\Delta t}(t_0)$ starts with a value

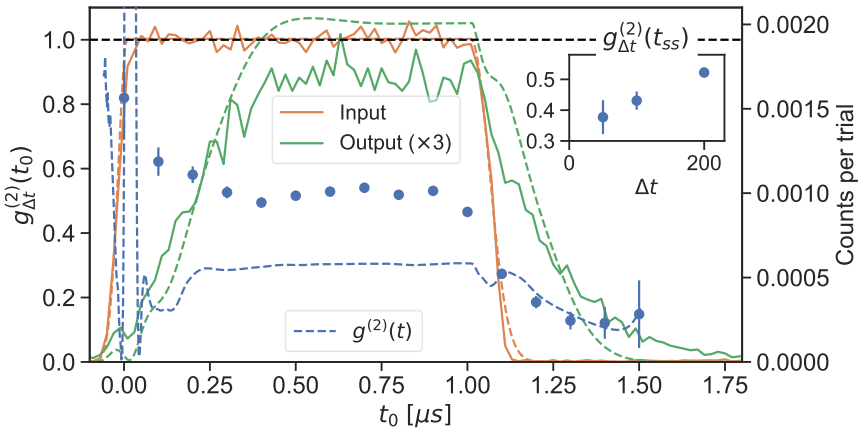

Figure 5.6: $g^{(2)}_{\Delta t}(t_0)$ as a function of the starting time t_0 (blue points, left y-axis) and counts per trial as a function of the arrival times to the first detector (orange and green solid lines, rigth y-axis). The dashed lines show the results from the theoretical simulation. Note that the theoretical $g^{(2)}(t)$ value (dashed blue line) corresponds to the case with $\Delta t \to 0$. For comparison, in the inset plot, we show that the average steady-state (ss) experimental value $g^{(2)}_{\Delta t}(t_{ss})$ tends to the theoretical $g^{(2)}(t_{ss}) \approx 0.3$ for smaller Δt. Moreover, note that using a $\Delta t > 0$ would smooth out the discontinuities seen in the simulation of the turn-on transient and could explain why they are not seen in the experimental data. Error bars correspond to one s.d.

close to 1, but then it decreases rapidly towards smaller values, remaining constant at the end of the pulse with $g^{(2)}_{\Delta t}(t_0) = 0.52 \pm 0.13$ for the last point ($t_0 = 0.8$ μs). For a triangular shape with a positive slope (figure 5.7b), i.e. slowly switched on and abruptly turned off, we only observe a clear transient at the end of the pulse, since $g^{(2)}_{\Delta t}(t_0)$ starts to decrease when the input pulse intensity goes to zero ($t_0 > 1$ μs). A value of $g^{(2)}_{\Delta t}(t_0) = 0.05 \pm 0.04$ is obtained for the last point ($t_0 = 0.8$ μs), which is much lower than observed for the triangular shape with negative slope.

These results show that the appearance of the transients depends on how the input pulse varies over time. Specifically, a first transient or very low values of $g^{(2)}_{\Delta t}(t_0)$ at the end are observed if the changes in the input probe intensity are abrupt. This can be explained from the simple picture of the physics described in the previous section. The dynamics

between photons propagating in a two-level system and Rydberg polaritons are distinguishable at the output only if the time in which the input probe field is switched on(off) is much smaller than L/v_{gr}. In this case, changes in the second-order correlation function at the beginning(end) of the output pulse will be observed.

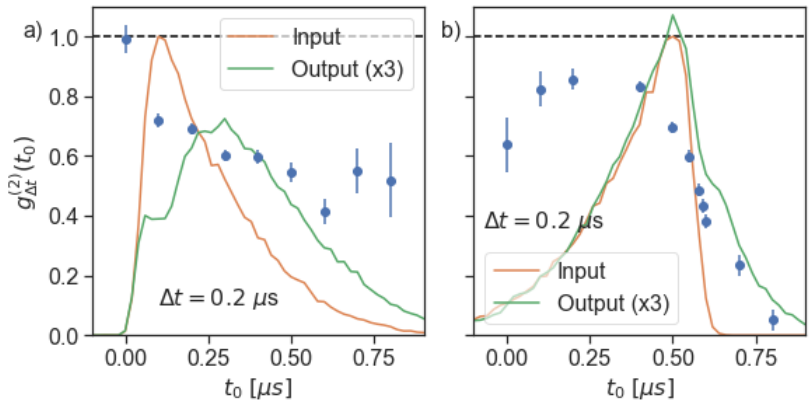

Figure 5.7: Second-order correlation function (in blue), for a time window of $\Delta t = 200$ ns inside the output pulse. The input and output counts arriving to the first detector (orange and green lines) are shown. Both are normalized to the maximum of the input counts and output is multiplied by 3. (a) Input pulse with a triangular shape and a negative slope and (b) with a positive slope. The error bars in figures represent one s.d.

5.7 Single-photon generation and storage

The second transient opens the way for possible applications related to narrowband single-photon generation. For that purpose, we could cut the output pulses and exploit the single photons arriving in the last part of the pulse. In order to analyze this proposal, we select a temporal window Δt at the end of the pulse when looking at the detector counts and coincidences. Then, we measure the statistics of the photons arriving inside this temporal window and their corresponding generation probability. The generation probability is inferred as $n_{out}(\Delta t)/\eta_{det}$, where $n_{out}(\Delta t)$ is the number of counts per trial arriving to the first detector in the selected time window and η_{det} is the detection efficiency, including

fiber coupling, transmission through all the optical elements and SPAD efficiency.

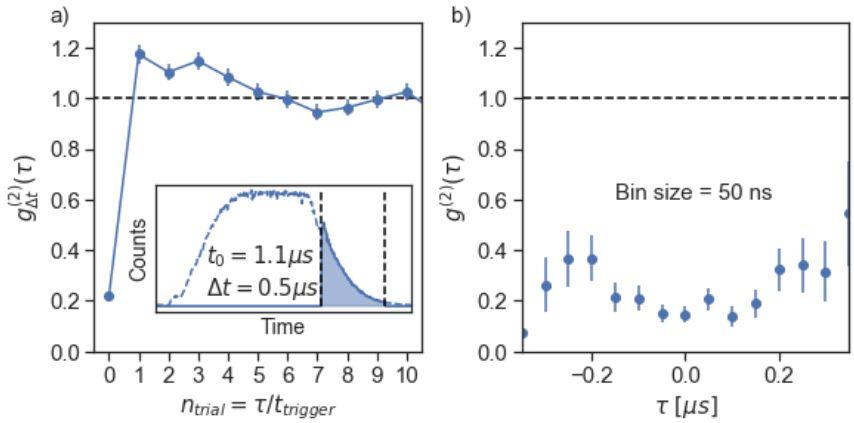

Figure 5.8: Example of single-photon generation with $\Delta t = 500$ ns and $t_0 = 1.1$ μs. (a) $g^{(2)}_{\Delta t}(\tau)$ as a function of n_{trial}, where $\tau = n_{trial} \cdot t_{trigger}$. The value at $n_{trial} = 0$ gives $g^{(2)}(0) = 0.218 \pm 0.015$, which represents a measurement of the whole-window statistics. (b) $g^{(2)}(\tau)$ for $\tau \ll t_{trigger}$, for a bin size of 50 ns. Contrary to figure 5.3, the value of $g^{(2)}(\tau)$ remains low for the whole window, confirming a localized single photon.

Figure 5.8 shows an example of single-photon generation for $\Delta t =$ 500 ns and $t_0 = 1.1$ μs. The value obtained for the whole window is shown in figure 5.8a, giving $g^{(2)}_{\Delta t}(0) = 0.218 \pm 0.015$, which is significantly lower than for $\Delta t = 1.6$ μs. Moreover, the time-resolved measurement of the second-order correlation function (figure 5.8b) shows that the values of $g^{(2)}(\tau)$ remain low for the full window, similar to what we obtain after storage (see figure 4.7 of section 4.6.2).

Figure 5.9 shows $g^{(2)}_{\Delta t}(t_0)$ for different Δt when the final time $t_{end} = t_0 + \Delta t = 1.6$ μs is fixed (see figure 5.9a), for Gaussian and square input pulses. When we increase the time window Δt, the probability to have a detection count increases, but at the expense of reducing the quality of the single photons. For the previously studied square pulse, a $g^{(2)}_{\Delta t}(t_0) = 0.48 \pm 0.01$ is obtained for $\Delta t = 0.68$ μs and a generation probability of 0.145 ± 0.014, while a $g^{(2)}_{\Delta t}(t_0) = 0.147 \pm 0.017$ is obtained for $\Delta t = 0.45$ μs and a generation probability of 0.046 ± 0.004. We

also compare the results for the square pulse with the case of a Gaussian input pulse. We see that the Gaussian pulse leads to higher value of $g^{(2)}_{\Delta t}(t_0)$ for all generation efficiencies compared to the square pulse. This confirms that switching off the input pulse abruptly is beneficial for the production of single photons.

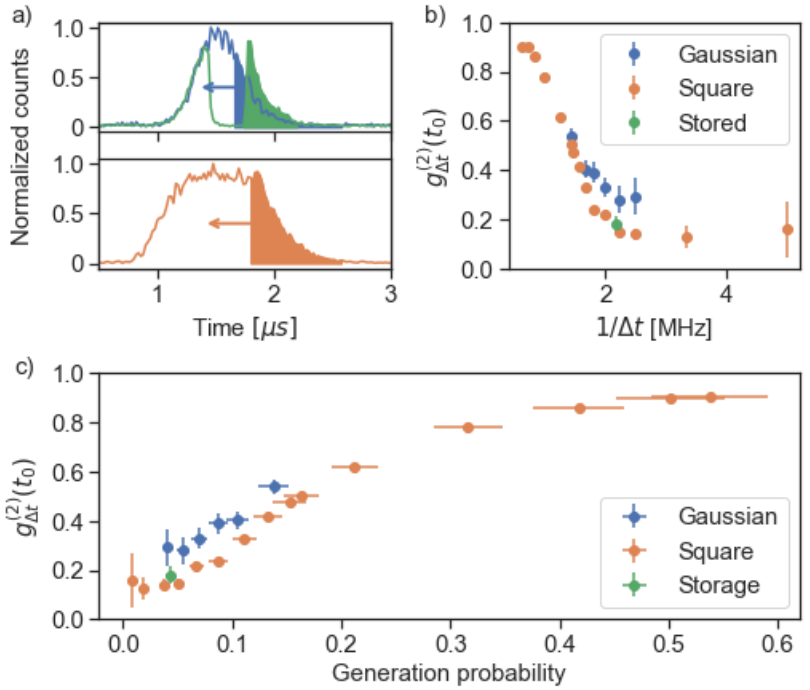

Figure 5.9: (a) Temporal distribution of a Gaussian pulse after propagation through EIT (blue) and after storage (green), and distribution of a square pulse (orange). In the slow-light case, the temporal window Δt is varied while the final time is fixed, as indicated by the shadowed region and the arrow. (b) $g^{(2)}_{\Delta t}(t_0)$ as a function of $1/\Delta t$, for an input Gaussian and square pulse and after storage. (c) $g^{(2)}_{\Delta t}(t_0)$ as a function of the probability to have a photon at the output of the cloud. Error bars correspond to one s.d.

For the Gaussian pulse, we also compare the results with the strategy consisting in storing the pulse in the Rydberg state. As the OD of our medium is limited, only a part of the pulse can be stored (green

plot of figure 5.9a). After a storage time of $t_{stor} = 500$ ns, we measure $g^{(2)}_{\Delta t}(0)$ by taking into account all the coincidences inside the whole output pulse. As we can observe in figure 5.9c, we obtain the same value of $g^{(2)}_{\Delta t}$ compared with the input square pulse, for similar or lower generation probability. For lower quality of the output photons, i.e higher values of $g^{(2)}_{\Delta t}(t_0)$, the generation probability in the transient case importantly increases. Finally, we plot $g^{(2)}_{\Delta t}(t_0)$ as a function of the inverse of Δt, which is proportional to the photon bandwidth. Values of $g^{(2)}_{\Delta t}(t_0) < 0.2$ can be achieved for $1/\Delta \sim 2$ MHz, showing that high quality, narrowband single photons can be generated with this technique.

5.8 Behavior with the number of input photons

We also studied the variation of the $g^{(2)}_{\Delta t}(t_0)$ over the pulse for different number of input photons. For that, we sent 1 μs-long square pulses in a medium with $OD \approx 5$ and coupling Rabi frequency $\Omega_c \approx 5.9$ MHz, which gives a group velocity of 400 $\mu m/\mu s$ In figure 5.10a, the temporal distribution of counts per trial arriving to the first detector is shown, for a bin size of 10 ns. Since the temporal width of the input pulse is 1 μs, $n_{in} \sim 7$ corresponds to < 2 photons in the medium at a time, still far from the saturation regime, where absorption is strong (note that the medium length is around 100 μm in the propagation direction, much longer than the blockade radius). However, some features related to scattering become evident, such as the hump appearing at early times for the highest number of input photons [124, 102]. The variation in the $g^{(2)}_{\Delta t}(t_0)$ over the pulse is shown in figure 5.10b for $\Delta t = 200$ ns. Although the three measurements are similar, the steady-state $g^{(2)}(0)$ increases with the input photon number, which is something that we have shown before in section 4.6.2, where we suggested an explanation based in the creation of pollutants [102]. Note that the second-order correlation within the same pulse can be affected by both long-lived pollutants that survive subsequent trials and short-lived pollutants that can be removed with the coupling field.

As the behavior in the second transient is not clear from the analysis of figure 5.10b, the $g^{(2)}_{\Delta t}(t_0)$ is studied by varying the temporal detection window Δt, while fixing the final time to $t_{end} = t_0 + \Delta t = 1.5$ μs.

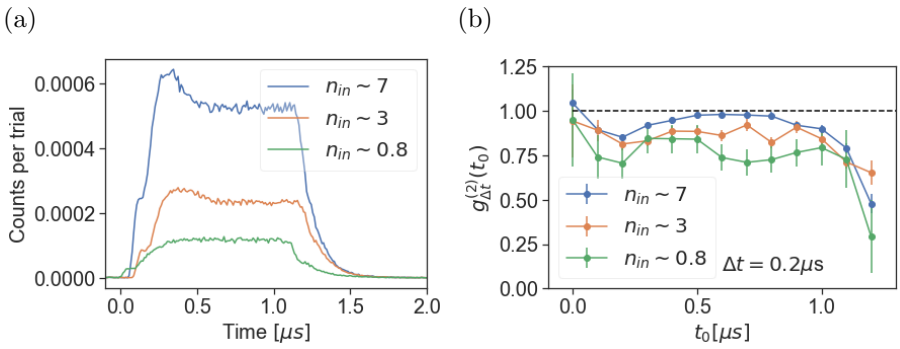

Figure 5.10: (a) Number of counts per trials as a function of the arriving time to the first detector after the trial trigger, for different values of n_{in}. Bin size is 10 ns. (b) $g^{(2)}_{\Delta t}(t_0)$ as a function of the starting time t_0, for $\Delta t = 200$ ns. $OD \approx 5$ and $\Omega_c \approx 5.9$ MHz. Note the lower counts per trial in this measurement is due to lower detection efficiency, probably due to misalignment of the detection setup. Error bars correspond to one s.d.

In the upper plot of figure 5.11, we can see that the same value of $g^{(2)}_{\Delta t}(t_0)$ is obtained for a longer Δt when the number of input photons is lower. Then, the related bandwidth increases with n_{in}. This could be explained if single photons leave the medium before when the number of input photons is higher. This could be understood from a scattering-induced projection of the Rydberg polariton wavefunction. In a simple picture, when a photon is scattered, there is a leakage of information into the environment about the position of the Rydberg polariton, which should be within a blockade time from the scattered photon. Therefore, it induces a projection of the polariton wavefunction to be inside this position range [123, 124]. In the lower plot, the value of $g^{(2)}_{\Delta t}(t_0)$ is shown as a function of the single photon generation probability. Although the differences between the three measurements is apparent for higher values of $g^{(2)}_{\Delta t}(t_0)$, where the same value is obtained with higher probability for greater n_{in}. However, for very low generation probabilities, reducing the size of the error bars of $g^{(2)}_{\Delta t}(t_0)$) is needed in order to see clear differences between n_{in}.

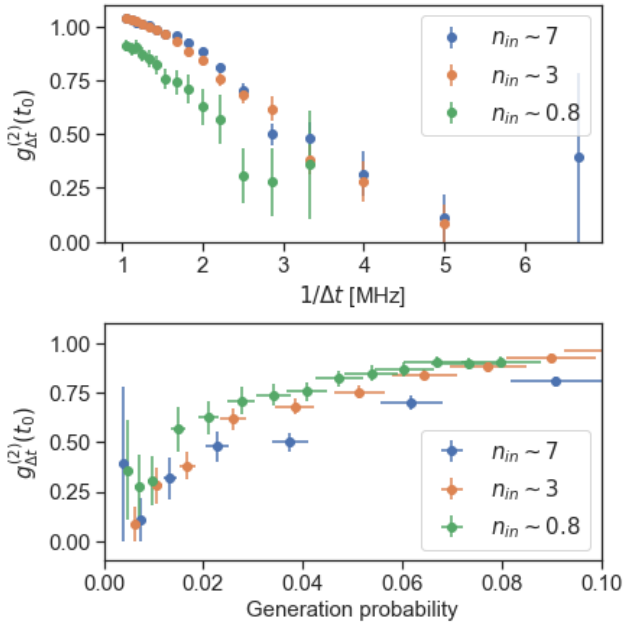

Figure 5.11: $g^{(2)}_{\Delta t}(t_0)$ obtained for different temporal window Δt at the end of the pulse, for different number of input photons. In the top, as a function of $1/\Delta t$. In the bottom, as a function of the probability to have a photon at the output of the cloud. Error bars correspond to one s.d.

5.9 Conclusions

In this chapter, we investigated the transients appearing for weak coherent pulses propagating in a cold atomic ensemble in the regime of Rydberg electromagnetically induced transparency. We found experimentally that the second order correlation function of the output pulse strongly depends on the temporal position and varies during the transient parts of the pulse. In particular, the value of $g^{(2)}_{\Delta t}(t_0)$ strongly decreases towards the end. Finally, we explored the possibility of using this effect to generate localized single photons.

As shown in section 5.5, increasing the optical depth and reducing the Rabi frequency of the coupling field results in a better separation between the two-photon dynamics and the single-photon one and therefore leads to a smaller value of $g^{(2)}_{\Delta t}$ in the turn-off transient. However, the

single photon generation efficiency is currently affected by the low value of the transmission in the EIT transparency window, which is likely limited by the decoherence rate of the $|g\rangle$ to $|r\rangle$ transition γ_{rg}, which also enforces a lower bound in the choice of Ω_c. We expect that reducing the laser linewidths (currently around 300 kHz) by active stabilization on an optical cavity would bring to a significant increase in the EIT transmission and also make lower choices of Ω_c possible. Moreover, a larger value of OD_b would allow a more efficient compression of the pulse within a blockade radius. The current values of the generation efficiency achieved (around 10%) are comparable with the values reported in single-photon generation experiments using off-resonant excitation techniques in Rydberg atoms [59]. It is informative to compare these values of efficiency with techniques of probabilistic single-photon generation with atomic ensembles, such as e.g. the Duan-Lukin-Cirac-Zoller scheme [39]. This scheme generates probabilistically photon pairs in a two-mode squeezed state with a probability per trial p, where one of the photon is stored as a collective atomic spin excitation in the ensemble. Upon detection of the first photon which provides a heralding signal, this collective spin excitation can then be efficiently transferred into a single photon in a well defined spatio-temporal mode with an efficiency η_R. The probability to generate a single photon per trial is therefore given by $P_{\mathrm{DLCZ}} = p\eta_D\eta_R$ where η_D is the probability to detect the first photon. For a perfect two-mode squeezed state and for $p \ll 1$, the second-order correlation of the retrieved photon is $g^{(2)}(0)=4p$. In the best case scenario (i.e. with unity detection and read-out efficiency), a DLCZ source could generate a photon with $g^{(2)}(0) = 0.1$ with a probability of $P_{DLCZ} = 0.025$ per trial. In practice, with finite detection and read-out efficiencies, this value will be even lower. Therefore, even though the single-photon generation efficiencies demonstrated in this chapter are quite modest and could be still largely improved, they compare favorably to probabilistic schemes.

Chapter 6

Indistinguishability of photons generated in a Rydberg ensemble

6.1 Introduction

For the implementation of quantum networks using collective Rydberg excitations as quantum nodes, a crucial next step is to generate entanglement between remote nodes. Quantum repeater architectures have been proposed, that rely on deterministic light-matter entanglement and two-qubit gates using Rydberg ensembles [72, 73]. In these architectures, distant Rydberg ensembles are entangled by a measurement induced process which involves interfering single photons emitted by the Rydberg ensembles and a Bell State Measurement. For this process to be successful, the single photons must be coherent and indistinguishable, in order to erase the information about the origin of the photons. So far, only a few experiments have probed the indistinguishability of single photons emitted by Rydberg ensembles [82, 104, 50]. In the work carried out by Li et al. (2013), they assessed the photon indistinguishability by performing Hong-Ou-Mandel experiments between a Rydberg photon and a weak coherent state [82]. In the work of Craddock et al. (2019), they interfered a Rydberg photon with another single photon created by a single ion [104]. However, in both experiments only a small part of the temporal waveform of the Rydberg single photon was probed. While this strategy allows observing high-visibility HOM dips for the selected photons and the generation of remote entanglement

by Bell state measurements, it reduces the available two-photon coincidence and entanglement rate per trial by a factor $(\Delta t/T)^2$, where Δt is the detection window considered and T is the total photon duration. The work recently carried out by Ornelas et al. (2020) [50] provided a great single-photon indistinguishability over the full photon window by interfering two Rydberg photons. Nevertheless, the works done up to date only investigated single photons generated by off-resonant (OR) two-photon excitation (also called Raman excitation) to the Rydberg state. The indistinguishability of single photons generated by Rydberg EIT, and the difference between both processes has not been investigated so far.

In this chapter, we investigate the indistinguishability of single photons retrieved from collective Rydberg excitations in cold atomic ensembles. The Rydberg spin waves are created either by off-resonant two-photon excitation to the Rydberg state or by Rydberg electromagnetically induced transparency. To assess the indistinguishability of the generated single photons, we perform Hong-Ou-Mandel experiments between the photons and weak coherent states of light. We analyze the obtained overlap as a function of the detection window and we find that the photons generated under Rydberg EIT conditions show slightly lower overlap than the ones generated by off-resonant excitation. We obtain an overlap greater than 72% in all cases reaching a value of 98% for a small detection window and off-resonant excitation to Rydberg state. These results are important for the use of Rydberg atomic ensembles as quantum network nodes.

The results shown in this chapter have been summarized in the arXiv paper [146] and hence, a large part of this chapter has been taken from it.

6.2 Single photon generation

In this experiment, we perform 37000 experimental trials per dipole trap cycle with a rate of 178 kHz during the trap lifetime. The atoms are excited to the Rydberg state $|r\rangle = |90S_{1/2}\rangle$ by means of a two-photon transition addressed by the probe and the coupling beam, as previous experiments. The optical depth of the atomic cloud for a resonant probe beam is around 5. The difference between the excitation under

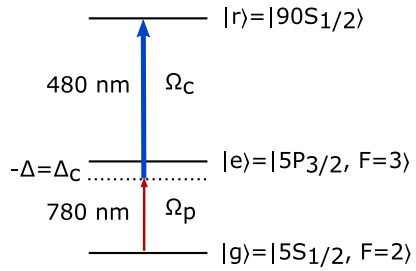

Figure 6.1: (a) Level scheme and transitions used in the experiment. The single-photon detunings of the probe (Δ) and coupling (Δ_c) beams are defined from the transition with regards to the intermediate state. In EIT conditions, $\Delta = \Delta_c = 0$.

EIT and OR conditions is mainly the one-photon detuning, defined as $\Delta = \omega_p - \omega_{ge}$ for the probe beam and $\Delta_c = \omega_c - \omega_{er}$ for the coupling, where $\omega_{p(c)}$ are the frequencies of the light fields and $\omega_{ge(er)}$ the frequencies of the corresponding atomic transitions (see figure 6.1). Under EIT conditions, $\Delta = \Delta_c = 0$ while for OR excitation, $\Delta = -\Delta_c = -40$ MHz. In both cases, the two-photon transition is sent on resonance so that $\delta = \Delta_c + \Delta \approx 0$.

The pulse sequence for the single-photon generation in our Rydberg ensemble for the OR excitation is represented in figure 3.12 of section 3.5. In this case, we send a probe and a coupling pulse[1] into the atomic medium both detuned from the $|e\rangle$ state by $\Delta = -\Delta_c = -40$ MHz, as we said before. Therefore, the interaction with $|e\rangle$ state can be neglected and the long-range interaction between Rydberg atoms allows ideally only one Rydberg excitation to be created. This excitation, usually called Rydberg spin wave, is collectively shared among all the atoms in the medium. By sending a close-to-resonant coupling pulse after a given storage time, we can retrieve a single photon under mode-matching conditions, i.e. with a frequency $\approx \omega_{ge}$ in the direction of the probe field.

The EIT sequence is represented in figure 3.11 of section 3.5. In this case, we send a weak probe pulse together with a coupling beam resonantly coupled to $|e\rangle$ state, so that $\Delta = -\Delta_c = 0$ MHz. Since the

[1]The shape of the coupling pulse at the beginning and the end of the experimental trial is given by the response time of the AOM but is optimized between the writing and retrieval.

Rabi frequency of the coupling beam is $\Omega_c \approx 6$ MHz, much higher than the probe coupling, a narrow frequency window is opened in which the medium is transparent to the probe. Due to dipole blockade, ideally only one Rydberg dark-state polariton is allowed to propagate through the medium at a time. By turning off the coupling beam, the polariton state becomes a purely Rydberg spin wave. To retrieve the excitation, the coupling field is turned back on and the polariton continues its propagation until exiting the medium, generating a single photon in the probe mode.

A study of the single photons obtained by these two methods under similar experimental conditions can reveal the differences between the physical mechanisms underlying both methods.

Note that, for our experimental conditions, we calculate a blockade radius of $r_b \approx 13$ μm for the EIT case and $r_b \approx 19$ μm for the OR excitation if we consider that the excitation linewidth is given by the laser linewidth ($\sim$ 300 kHz). Since these values are lower than the medium length L, more than one Rydberg excitation can be created in both cases. Hence, we expect interaction-induced dephasing (see section 2.6) to play a role in the single-photon generation.

6.3 Second-order correlation function

The second-order correlation function is measured by means of a Hanbury-Brown and Twiss experiment (see section 2.2 and 3.6). The detection window Δt is chosen to include the whole retrieval photon pulse. The normalization factor is the product of the single-photon detection probabilities. In figure 6.2, we show the $g^{(2)}_{\Delta t}(\tau)$ between different trials. In the left, we show the results for single photons generated by off-resonant excitation and in the right, under EIT conditions. The values at zero-delay time correspond to the second-order correlation function of the whole photon pulse. For the OR excitation case, we obtain $g^{(2)}_{\Delta t}(0) = 0.225 \pm 0.014$, which is higher than the value obtained for the EIT case $g^{(2)}_{\Delta t}(0) = 0.171 \pm 0.012$. In both cases, we can see a clear antibunching feature, which is a proof of quantum behavior and single-photon emission.

A time-resolved $g^{(2)}(\tau)$ is presented in figure 6.3, where the normal-

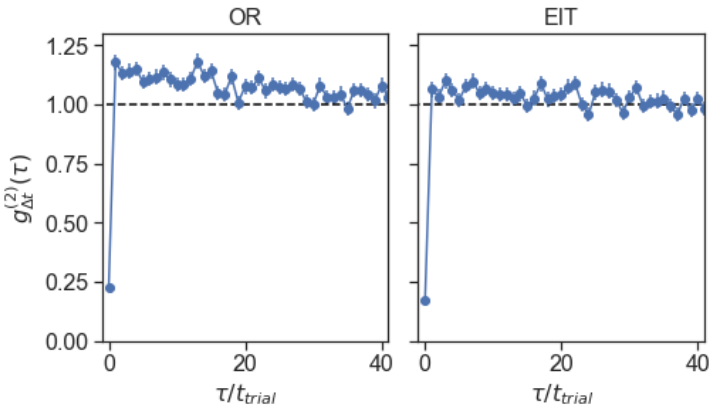

Figure 6.2: Second-order correlation function for different trials. In the left, for photons generated by means of off-resonant excitation to the Rydberg state. In the right, for photons generated by resonant Rydberg EIT.

ization factor is measured by the coincidences between distant trials. For the OR excitation scheme, $g^{(2)}(0) = 0.14 \pm 0.04$ and the variation with different τ seems higher than for the EIT case, where the second-order correlation function at zero-delay time is $g^{(2)}(0) = 0.11 \pm 0.04$. From these measurements, we observe that the quality of the single photons, considering the probability of generating two photons in the pulse, is better for EIT conditions than for the OR excitation case.

The dependency of $g^{(2)}_{\Delta t}(0)$ with the probability to generate single photons on the output is shown in figure 6.4 for the OR case. The photon generation probability is quantified by P_{SP}, defined as $P_{SP} = \frac{p_1}{\eta_{det,1}}$ where p_1 is the number of detections per trial in the $SPAD_1$ and $\eta_{det} \approx 0.07$ is the detection efficiency of the $SPAD_1$ which includes all optical losses from the atomic cloud to the detector and the $SPAD_1$ efficiency. P_{SP} is varied by controlling the mean number of input photons n_{in} of the writing probe pulse. As we can see, the source still preserve its quantum characteristic with increasing number of photons, remaining with $g^{(2)}(0) < 0.4$ for all n_{in}, with a maximal value of $g^{(2)}(0) = 0.35 \pm 0.04$ for $P_{SP} = 0.18 \pm 0.02$. The behavior of photons generated by EIT with respect to n_{in} is very different and will be discussed in section 6.4.2.

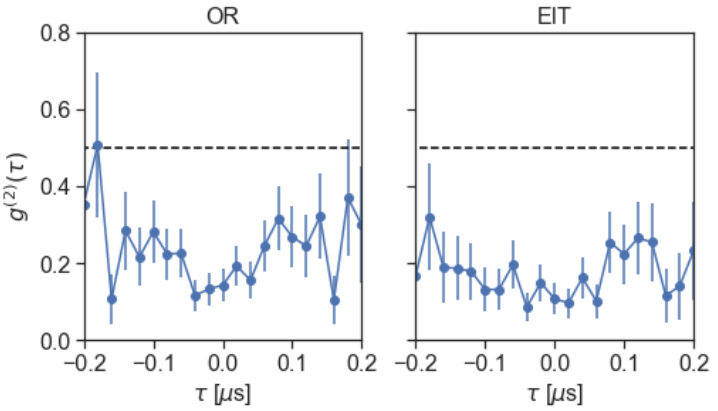

Figure 6.3: Second-order correlation function as a function of the delay time within the same pulse. In the left, for photons generated by means of off-resonant excitation to the Rydberg state. In the right, for photons generated by resonant Rydberg EIT.

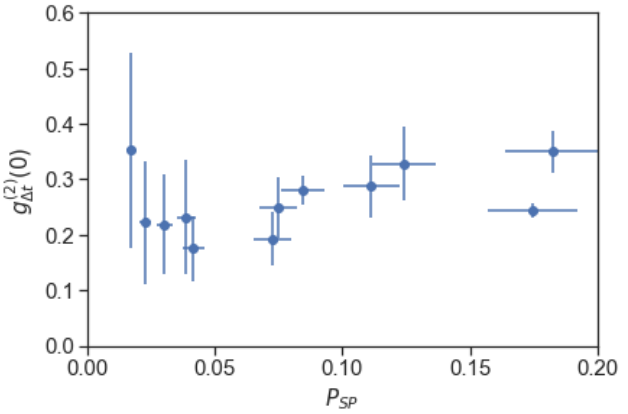

Figure 6.4: Second-order correlation function for single photons generated by means of off-resonant excitation to the Rydberg state, as a function of the single-photon generation probability.

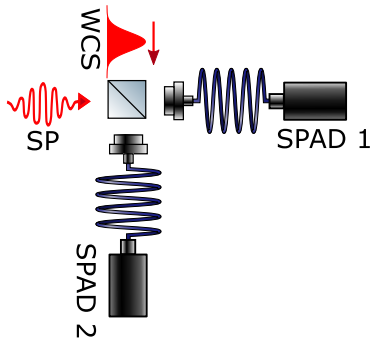

Figure 6.5: Experimental setup of the HOM measurement. The single photons generated in the Rydberg ensemble (SP) are sent to one port of a beamsplitter, while in the second port we send a weak coherent state (WCS). The outputs are sent to two single-photon detectors ($SPAD_1$ and $SPAD_2$) in order to measure the coincidence probability. Note that in the experiment, we use a fiber-based beamsplitter in order to reduce spatial mismatch.

6.4 Indistinguishability

To probe the indistinguishability of the photons emitted by the Rydberg ensemble we perform Hong-Ou-Mandel interference measurement (see section 2.3) with a weak coherent state pulse (WCS), as represented in figure 6.5. The WCS is obtained by strongly filtering a beam coming from the same laser as the probe, so that the mean number of photons per pulse is much smaller than one. We perform the HOM by sending the single photon emitted by the Rydberg ensemble to one port of a beamsplitter and the photon coming from the WCS to the second port. We then record the photon arrival times at each single-photon detector and the trial trigger times in a time stamp file. From that, we can derive the coincidences per trial in different detection windows.

The visibility of the HOM is then defined as $V = 1 - \frac{p_{ind}}{p_d}$, where p_{ind} and p_d are the number of coincidences per trial when the two photons are made indistinguishable and distinguishable, respectively. To generate the distinguishable input, we apply a delay between the WCS pulse and the retrieval time of the photon emitted by the Rydberg ensemble. For the sequence with indistinguishable inputs, WCS pulse and single photon overlap in time. Finally, we can estimate the indistinguishability

between the single photons and the weak coherent state by following the model presented by Li et al. in 2013 [82]. They calculate the probability p_{ind} as:

$$p_{ind} = \frac{p^2}{4} g^{(2)}(0) + \frac{|\bar{\alpha}|^4}{4} + (1-\eta)\frac{p|\bar{\alpha}|^2}{2} \tag{6.1}$$

where η is the mode overlap between the Rydberg photon and the WCS, p is the probability to detect the Rydberg photon, $g^{(2)}(0)$ is the second-order correlation function of the Rydberg photon and $|\bar{\alpha}|^2$ is the probability to detect a photon coming from the WCS. Then, the mean number of photons in the WCS is $|\alpha|^2 \approx |\bar{\alpha}|^2 \eta_{det}^{total}$, where η_{det}^{total} is the total detection efficiency taking into account both detectors. This simple equation makes the following assumptions:

- Three-photon coincidence events are negligible.
- The weak coherent state is weak enough so that we never have three photons in the second port.
- Imbalance ratio of the beamsplitter is negligible.

The first two conditions are mainly satisfied if $|\alpha|^2 \ll 1$. The beamsplitter is a fiber-based one from Thorlabs with a ratio 53 : 47. Accounting for the imperfect balance of the BS results in slightly higher indistinguishability factors, with a difference much smaller than the error bars [147]. Although the previous equation also assume that the detection efficiencies of both detectors are the same, these are canceled when calculating the visibility (see equation 6.3).

For completely distinguishable fields ($\eta = 0$), we obtain:

$$p_d = \frac{p^2}{4} g^{(2)}(0) + \frac{|\bar{\alpha}|^4}{4} + \frac{p|\bar{\alpha}|^2}{2}. \tag{6.2}$$

Therefore, we can compute the visibility:

$$V = 1 - \frac{p_{ind}}{p_d} = \frac{\eta p |\bar{\alpha}|^2}{\frac{p^2}{2} g^{(2)}(0) + \frac{|\bar{\alpha}|^4}{2} + p|\bar{\alpha}|^2}. \tag{6.3}$$

A high visibility would be achieved for two perfectly indistinguishable photons ($\eta = 1$). In this case, the third term of equation 6.1 would vanish and, since the first two other terms are related to two-photon events coming from the same port, they would give small contributions.

Specifically, we can extract from equation 6.3 that, in the limit of a perfect single photon ($g^{(2)}(0) \to 0$) and very small contribution of the WCS ($|\alpha|^2 \to 0$), the visibility tends to the indistinguishability factor η.

6.4.1 Photons generated by off-resonant excitation.

We first analyze the case of excitation in the OR condition. In the left plot of figure 6.6, we show an example of the pulses when they are made indistinguishable (upper plot) and distinguishable (bottom). In this case, the two photons are detected in well-differentiated time windows, labeled as SP and WCS. For the analyses of this data, we consider two different detection window durations: one with $\Delta t = 500$ ns, which contains the full pulse, and another with $\Delta t = 100$ ns, centered in the maximum amplitude. In the right plot of figure 6.6, we measure the visibility for different mean number of photons in the WCS, for both detection windows. The maximum visibility achieved is $V = 0.58 \pm 0.03$ for $\Delta t = 500$ ns and $V = 0.66 \pm 0.07$ for $\Delta t = 100$ ns. In both cases, we thus achieve a visibility higher than the 0.5 classical value expected for interference of two WCS [148, 149], attesting quantum photonic antibunching and therefore the quantum behavior of our Rydberg source. From the distinguishable measurement, we obtain the ratio $|\bar{\alpha}|^2/p$ by counting the photons arriving in the SP and WCS window and the second-order correlation function of the Rydberg photons $g^{(2)}(0) \equiv g^{(2)}_{\Delta t}(0)$ by measuring the coincidences within the SP window. We obtain $g^{(2)}_{\Delta t}(0) = 0.266 \pm 0.005$ for $\Delta t = 500$ ns and $g^{(2)}_{\Delta t}(0) = 0.22 \pm 0.01$ for $\Delta t = 100$ ns. With these values, we fit the data to equation 6.3 and extract the indistinguishability factor. For $\Delta t = 500$ ns, we find $\eta = 0.89 \pm 0.02$ and for $\Delta t = 100$ ns, $\eta = 0.98 \pm 0.01$.

We can see that reducing the window of observation leads to higher visibilities and higher indistinguishability factors, which is in accordance with previous observations [82, 104]. This is due to the fact that restricting the window of observation to values smaller than the coherence times of the retrieved photons can decrease the distinguishability between photons and therefore increase the visibility. A more extensive study of the indistinguishability with respect to Δt, by comparing to the EIT case, will be presented in section 6.4.3. We point out that we did an evaluation of the accidental coincidences due to dark counts and they do not

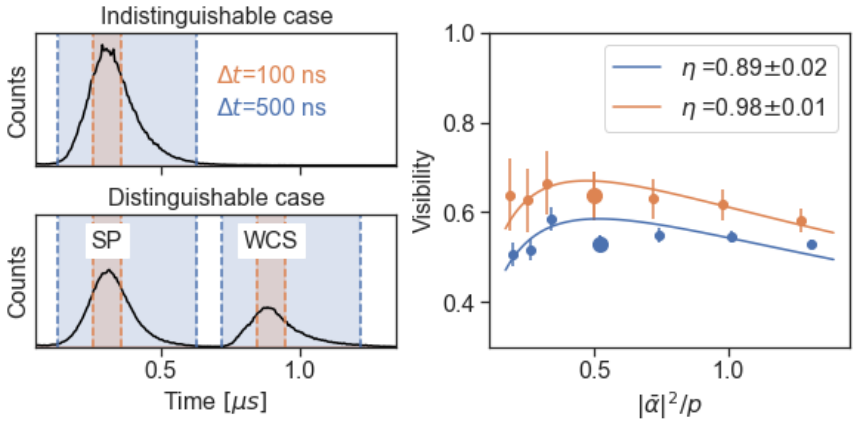

Figure 6.6: **Off-resonant excitation**: On the left, temporal distribution of photon counts for the indistinguishable (top) and distinguishable (bottom) case. Two detection temporal windows of $\Delta t = 500$ ns and $\Delta t = 100$ ns are shown. On the right, visibility is plotted as a function of the probability ratio $|\bar{\alpha}|^2/p$ for the two different detection windows of left panel. The indistinguishability is obtained from a fit to equation 6.3 (continuous lines). Error bars correspond to one s.d.

have a detrimental impact in our observations, i.e. a background correction of the data leaves results inside the error bars of the non-corrected values. Therefore, no background subtraction is performed in the data presented here.

6.4.2 Photons generated by EIT

The visibility of single photons generated by Rydberg EIT are shown in figure 6.7. We can see that these values are in general lower than in the OR excitation case, shown in figure 6.6. We observe that, when the detection window takes into account all the pulse statistics ($\Delta t = 600$ ns), the visibility remains below 0.5 for most points, with a maximum value of $V = 0.54 \pm 0.03$. However, for a detection window of $\Delta t = 100$ ns, it is over 0.5 with a maximum of $V = 0.67 \pm 0.09$. Even though the HOM visibilities are lower for EIT photons, the values of $g^{(2)}_{\Delta t}(0)$ are better than for OR photons. The measured second-order correlation function of the Rydberg photons are $g^{(2)}_{\Delta t}(0) = 0.166 \pm 0.005$ for $\Delta t = 600$ ns and

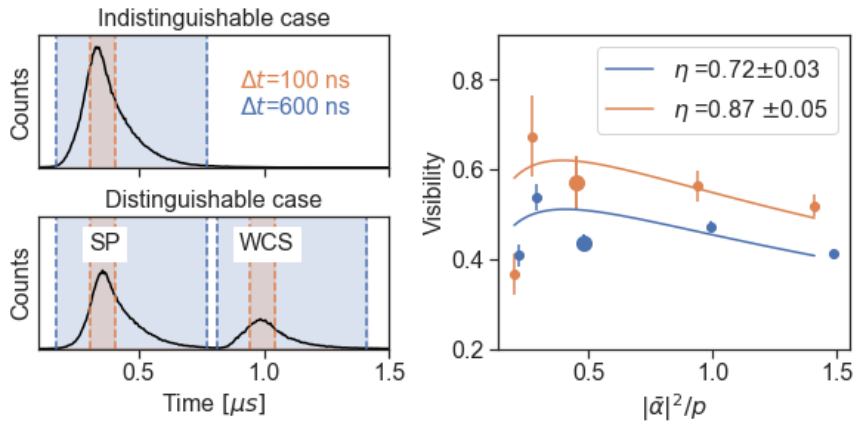

Figure 6.7: **EIT**: On the left, temporal distribution of photon counts for the indistinguishable (top) and distinguishable (bottom) case. Two detection temporal windows of $\Delta t = 600$ ns (including the whole pulse) and $\Delta t = 100$ ns (centered in the single photon) are shown. On the right, visibility as a function of the probability ratio $|\bar{\alpha}|^2/p$, for the two different detection windows of left panel. The indistinguishability is obtained from a fit to equation 6.3 (continuous lines). Error bars correspond to one s.d.

$g^{(2)}_{\Delta t}(0) = 0.16 \pm 0.01$ for $\Delta t = 100$ ns. Note that for that experiment, there was a small frequency shift of 380 kHz between the WCS and the retrieved single photon, which is expected to cause a decrease of only 3% in the indistinguishability. Also, the observation window for $\Delta t = 600$ ns is not centered at maximum amplitude, but optimized to include a larger portion of the pulse, because in contrast to the OR excitation, the pulse is not symmetric.

6.4.3 Variation with the detection window

To investigate further the effect of the observation window, we vary Δt for the OR and EIT case, as shown in figure 6.8. On those measurements, although we observe an increase in the probability to generate a photon P_{SP} with increased observation window, it is accompanied with a decrease in the indistinguishability and an increase in the second-order correlation function, implying a statistical decrease in the quality of the

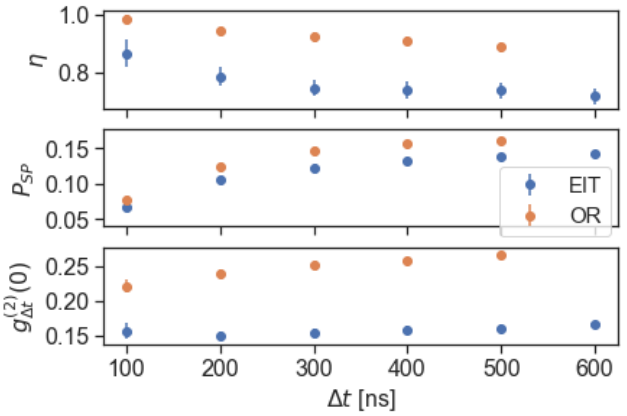

Figure 6.8: Variation of measurement parameters in OR condition with respect to the window duration. In the top panel, the indistinguishability η between a photon from the WCS and a Rydberg photon; in the center, the probability to detect a Rydberg photon in each trial P_{SP} and in the bottom, the second-order correlation function of Rydberg photons $g^{(2)}_{\Delta t}(0)$.

single photon. This decrease could be explained by the effect of the finite laser linewidths, which limits the coherence time of both the WCS and the single photon [150, 151, 152]. Another reason could be the temporal waveform mismatch between the single photons retrieved from the Rydberg ensemble and the WCS. However, in our case we inferred a temporal overlap above 98% for OR excitation and 97% for EIT conditions. If the energy shift between WCS and single photon central frequency in the EIT case is considered, this value is decreased to 94%. These values, while slightly lower than for the OR case, are not sufficient to explain the lower indistinguishability of the single photons generated through EIT.

6.4.4 Variation within the pulse waveform

To further evaluate how the distinguishability varies inside the photon envelope, we implement a time-resolved analysis of the visibility, as shown in figure 6.9. For that, we measure the coincidences profile within one trial for the distinguishable and indistinguishable cases with a bin size of 20 ns. For the distinguishable case, we apply a correction in the delay time between two detections in order to calculate the coincidences

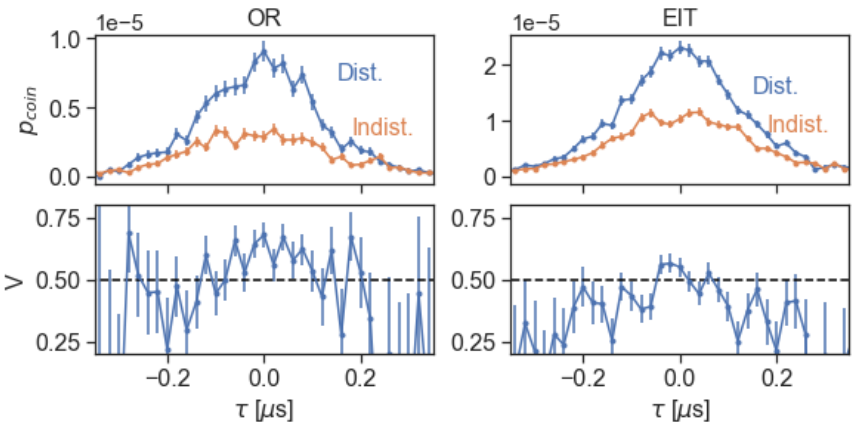

Figure 6.9: Time-resolved coincidences for OR excitation and EIT excitation. On the top charts we show the time resolved coincidences, for a bin size of 20 ns, covering the whole extension of the pulse. On the bottom charts, we show the visibility obtained for the same conditions.

we would obtain if the Rydberg photon and the WCS overlapped in time. We observe that the visibility is higher at the center and decreases on the wings, which is in agreement with the measurements of figure 6.8. However, the decrease is small and the visibility, and therefore the indistinguishability, remains high over the full single-photon pulse. This is in contrast to single photons emitted by ions in cavities [153] or by most solid-state systems and shows that Rydberg emitted photons are well suited for quantum communication tasks, where the possibility of using an extended detection window results in increased efficiency in the generation of entanglement between remote nodes. The lower indistinguishability for the single photons generated by EIT in comparison with the photons generated by OR excitation is also confirmed by this measurement, where we observe a similar behavior than for the OR photons, but with lower visibilities.

6.4.5 Discussion of the differences between EIT and OR excitation

As mentioned before, the expected indistinguishability taking into account waveform mismatch and frequency shifts are different for the EIT and OR excitation cases. However, these arguments are not enough to

explain the disrupted photon generation.

Both in EIT and in OR excitation, the single photons are retrieved from Rydberg spin waves by sending a resonant coupling pulse to the atomic ensemble. Therefore, it is normal to look for the cause in the writing process. The disrupted photon generation may be explained considering that, in Rydberg EIT conditions, input photons can interact with the intermediate excited state and lead to photon scattering depending on the input photon number n_{in}. To further study that, we measure the indistinguishability of photons generated under EIT conditions with respect to n_{in}. The results are shown in figure 6.10, for n_{in} varying from 1 to 20. We observe that the indistinguishability η varies between 0.7 and 0.8. In addition, the probability to generate a single photon P_{SP} decreases with increasing number of input photons, particularly for $n_{in} > 10$. The decrease in efficiency is accompanied by a strong degradation of the single photon quality, witnessed by a large increase in $g^{(2)}(0)$, up to $g^{(2)}(0) = 0.63 \pm 0.02$ for $n_{in} = 20 \pm 2$. The presence of scattering over the n_{in} range is demonstrated by a strong decrease in the light transmission under EIT conditions with increasing n_{in}, decreasing by a factor of 3.6 for n_{in} varying from 1 to 20.

Gorshkov et al. predicted theoretically in 2013 that the photon purity P (which gives an upper bound for the indistinguishability) decreases with n_{in} until reaching a steady value of 0.5, for the light transmitted under the regime of Rydberg EIT [123]. This loss of photon purity is due to the fact that when n_{in} increases, there is an increasing probability of having two photons within a blockade radius, leading to an increase in the scattering events. In a simple picture, when a photon is scattered, there is a leakage of information into the environment about the position of the Rydberg polariton, which should be within a blockade time from the scattered photon. Therefore, it induces a projection of the polariton wavefunction [123], which decreases the purity of the transmitted single photons. However, this seems in contradiction with the data presented in figure 6.10, where the overlap does not clearly decreases with n_{in}. A possible explanation can be found if we consider the photon dissipation due to the finite EIT bandwidth. In this case, if the polariton wavefunction is projected, it can be filtered out of the transmitted mode since its bandwidth does not fit inside the EIT bandwidth [124, 102]. This effect also cause a decrease in the single-

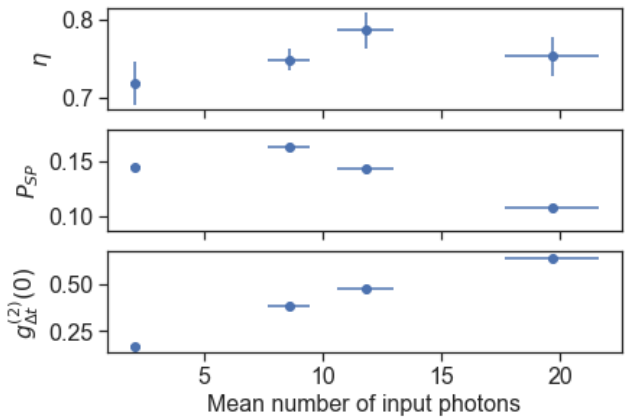

Figure 6.10: Variation of measurement parameters in EIT condition with respect to the mean number of input photons. In the top panel, the overlap η between a photon from the WCS and a Rydberg photon; in the center, the probability to generate a Rydberg photon in each trial P_{SP} and in the bottom, the second-order correlation function of Rydberg photons $g^{(2)}(0)$.

photon generation probability, which is in agreement with the behavior that we observe in figure 6.10. In the second-order correlation function, it produces a bunching around antibunching, for photons propagating as Rydberg polaritons [102]. Another explanation for the decrease in the single-photon generation probability is the formation of pollutants created by the reabsorption of scattered photons [102]. As we have said before, pollutants are Rydberg excitations that cannot be retrieved in the probe mode but prevent the generation of single photons due to the blockade effect. The consequence in the second-order correlation function is also a bunching behavior [102, 50]. These pollutants can be formed, for example, when atoms decay to another Rydberg level not coupled to the coupling field, leading to long-lived pollutants that can block the creation of Rydberg polaritons over several trials. In this way, they produce bunching between consecutive trials, as shown in the figure 6.2. Although these types of contaminants can be generated by both excitation schemes, the presence of scattering in EIT constitutes an additional source of pollutants, which are formed by the reabsorption of scattered photons. Since these contaminants are in resonance with the coupling field, they can be removed from one trial to the next and are

therefore short-lived. However, these could also decay to another Rydberg level, leading to long-lived pollutants. To our knowledge, a proper theory describing the effect of pollutants on the indistinguishability and quality of single photons generated by Rydberg EIT with storage has not yet been proposed.

In summary, we observed that the overlaps and HOM visibilities are lower for the photons generated with the EIT protocol, and that the quality of the single photon degrades faster with n_{in} than with the OR protocol. These effects may be due to the presence of scattering inducing decoherence and generation of pollutants. However, more measurements and a full model of decoherence in Rydberg EIT storage would be needed to quantify the consequences of scattering.

6.5 Conclusion

We conducted an extensive study of the quality of the single photons generated by Rydberg-mediated nonlinearities. We performed Hanbury-Brown and Twiss experiment together with HOM interferometry comparing two excitation schemes, namely OR and EIT. We provided figures of merit for the single-photon generation and characterization in each of those schemes and concluded that the single photons generated by EIT scheme show a lower second-order correlation function than the ones obtained in the OR scheme, giving a value of $g^{(2)}_{\Delta t}(0) \approx 0.17$ for the whole pulse and without background correction. However, the single photons generated by OR excitation have a superior indistinguishability, presenting an overlap of 89% for the full pulse, and up to 98% for a smaller detection window. We discussed the impact of extending the window of observation in the indistinguishability and concluded that, despite higher values of overlap are achieved for smaller windows of observations, the single photons remain highly indistinguishable for the whole duration of the pulse. These observations are interesting for applications in quantum communications, where extending the window of observation implies a gain in efficiency and distant entanglement rate.

Chapter 7

Conclusions

7.1 Main results of the thesis

The first goal of this thesis was to achieve nonlinearities at the single-photon level in a cold Rydberg atomic ensemble, by exploiting the strong dipole interactions between Rydberg atoms. We achieved this by making several improvements to the previous experimental setup, including increasing the atomic density of our cloud, increasing the principal quantum number to n=90 and implementing a dipole trap for the atoms. The latter, of particular relevance, allowed us to obtain an atomic cloud with a density of $3{\cdot}10^{11}$ cm^{-3} and a transverse length of 34 μm. With this configuration, we achieved an optical density per blockade radius (OD_b) of the order of one and a volume of the interaction region small enough to fit very few blockade spheres. Quantum nonlinearity was demonstrated by obtaining an antibunching dip in the statistics of the light after interacting with the Rydberg states under conditions of EIT. The generation of single photons at the output was witnessed by a second order correlation function smaller than 0.5, measured for the whole pulse, when weak coherent states of light pulses were sent as an input. In addition, we performed a detailed characterization of the nonlinearity as a function of the principal quantum number of the Rydberg state, the storage time and the number of photons in the input pulse.

In a second step, we conducted an in-depth study of the transients in the output pulses of light, after propagating through the medium as Rydberg polaritons. We showed that the properties of the light after the second transient are very similar to those obtained after storage, if the

input pulse is switched off fast enough, i.e. faster than the time it takes for a polariton to cross the medium. Thanks to the collaboration with theorists from the group of Darrick Chang at ICFO, we were able to qualitatively and quantitatively explain these results, although we have only presented here an intuition of the physics behind this phenomena. With the intention of exploiting these results to generate single photons more efficiently, we studied the statistics of the light in the final transient as a function of the probability to have a photon at the output of the atomic cloud and we compared these results with the strategy based on storing as Rydberg spin waves. We showed that it is possible to generate photons more efficiently at the cost of slightly deteriorating the single-photon quality.

Finally, we did a more in-depth study of the quality of the single photons retrieved from a Rydberg spin wave. To do this, the Rydberg spin wave was created by means of two different methods: by the previously realized storage under EIT condition and by off-resonant excitation to the Rydberg state, where the atoms were excited using a two-photon transition with a large detuning with respect to the intermediate state. The quality of the generated photons was characterized by measuring the second-order correlation function and the indistinguishability, a crucial property to use Rydberg atoms as quantum network nodes. The indistinguishability was measured from the interference between the single photon and a weak coherent state of light in a Hong-Ou-Mandel experiment. Although the obtained $g^{(2)}$ values of the single photons obtained by excitation under EIT conditions were better than for the off-resonant excitation case, the indistinguishability was considerably better for the off-resonant excitation method, showing visibilities much higher than the classical limit of 50% and an overlap of 82%, taking into account the entire pulse. The mismatch observed between both excitation procedures still needs a proper theoretical simulation, although we introduced some possible explanations. As we said before, these results are important for using Rydberg atoms as quantum nodes. For example, if we want to entangle two remote nodes, we can interfere the single photons emitted by both nodes in a Bell state measurement in which success depends on the indistinguishability between them.

7.2 Future directions

As we said in the introduction, the ultimate goal of this project is to create a two-qubit quantum gate to perform deterministic Bell state measurements in quantum repeater protocols. In this final scenario, the entangled photons will be generated from an external source and sent to the Rydberg atomic cloud to make them interact. The entangled photon source that will be used in our case is a DLCZ quantum memory, based on an atomic ensemble, which is placed in another experiment in our laboratory. To meet this goal, many intermediate steps must be taken. In this sense, the experiment we conducted in 2017 [83] was an important first step, as we demonstrated a good connection between both systems by storing a heralded photon coming from the DLCZ-based photon source in a Rydberg state. We demonstrated that the quantum properties of the photon were preserved after retrieval from the Rydberg spin wave. However, the nonlinearity of the medium was far from the single-photon level.

After this, one possible next step is to demonstrate coherent storage and retrieval of a photonic qubit in the Rydberg atomic cloud. A photonic time-bin qubit generated by the DLCZ quantum memory [154] can be converted into a frequency basis, such that the early bin is connected to a Rydberg state, while the late bin is coupled to a long-lived ground state, by means of two different coupling beams under conditions of EIT. After storage in these states, we can retrieve them and study whether the qubit quantum properties are preserved.

Another possibility will be to study the interaction between a single photon and a weak coherent state, so that the storage of a single photon as a Rydberg spin wave blockades the excitation caused by the weak coherent state. Therefore, the photon (or the photonic qubit) will act as the control and the weak coherent state as the target. The single photon must be coupled to a different Rydberg state than the weak coherent state by using another coupling beam at a different frequency. In that case, the two states can be chosen to be close to a Förster resonance. Another option is to store the control and the target in two independent spatial modes but close enough to interact with each other [66], as in a two-rail configuration [69]. Interactions between two single photons will require an additional source of heralded photons or an improvement in the generation rate of the current one.

At the same time, improvements will be made to the experimental setup. The first will be to reduce the combined probe and coupling laser linewidth by stabilizing them with respect to a highly stable Fabry-Perot cavity [155, 156]. This is necessary due to the long lifetime of Rydberg atoms, of hundreds of μs, which corresponds to a natural linewidth of tens of kHz. A combined laser linewidth of this magnitude will reduce the dephasing from the Rydberg state γ_{gr}, resulting in higher EIT transparency, which will allow us to excite to Rydberg states with higher principal quantum number. Besides this, a smaller volume of the interaction region and higher density of the atoms can be achieved by implementing a crossed dipole trap instead of a single one.

A different approach is to use the Rydberg atomic cloud as an emitter node and take advantage of the blockade effect to entangle a photon and a collective atomic excitation in a deterministic way [28, 72, 73]. This would be very useful for quantum repeaters since it allows to increase the entanglement distribution rate, compared to other protocols based on probabilistic processes such as the DLCZ scheme. In Rydberg atoms-based quantum repeaters [72, 73], the entanglement swapping between remote nodes is performed by deterministic Bell state measurements between two collective atomic excitations. As a first step towards this goal, we could generate a deterministic entanglement between a photon and a collective atomic excitation. In order to achieve this, we should implement a blockade-based quantum gate between two collective atomic excitations. We could also use this method to generate entanglement between two disparate nodes, such as the Rydberg ensemble and the DLCZ quantum memory, by interfering the photonic qubits generated by both systems. For that, we should demonstrate that these photons are indistinguishable.

Therefore, the next step toward the connection between both experiments is to measure the indistinguishability between the photons generated in the Rydberg cloud and the photons generated by the DLCZ quantum memory, something crucial in order to perform remote entanglement between two different nodes. For this, we will realize a HOM experiment similar to the one carried out in section 6.4, but this time by interfering the Rydberg photon with a heralded photon from the DLCZ quantum memory, which adds considerable technical difficulty.

In conclusion, the results achieved in this thesis constitute a fundamental starting point for future applications of Rydberg atoms in quantum processing and communication.

Bibliography

[1] M. A. Nielsen and I. L. Chuang: *Quantum Computation and Quantum Information*, Cambridge (2000).

[2] P. Zoller, T. Beth, D. Binosi, R. Blatt, et al.: *Quantum information processing and communication*, The European Physical Journal D - Atomic, Molecular, Optical and Plasma Physics **36**, 203 (2005).

[3] N. Gisin, G. Ribordy, W. Tittel, and H. Zbinden: *Quantum cryptography*, Rev. Mod. Phys. **74**, 145 (2002).

[4] A. K. Ekert: *Quantum cryptography based on Bell's theorem*, Phys. Rev. Lett. **67**, 661 (1991).

[5] C. H. Bennett, F. Bessette, G. Brassard, L. Salvail, et al.: *Experimental quantum cryptography*, Journal of cryptology **5**, 3 (1992).

[6] C. H. Bennett and G. Brassard: *Quantum cryptography: Public key distribution and coin tossing*, in *Proceedings of the International Conference on Computers, Systems and Signal Processing* (1984).

[7] B. Korzh, C. C. W. Lim, R. Houlmann, N. Gisin, et al.: *Provably secure and practical quantum key distribution over 307 km of optical fibre*, Nat. Photonics **9**, 163 (2015).

[8] S.-K. Liao, W.-Q. Cai, J. Handsteiner, B. Liu, et al.: *Satellite-Relayed Intercontinental Quantum Network*, Phys. Rev. Lett. **120**, 030501 (2018).

[9] J. Yin, Y. Cao, Y.-H. Li, S.-K. Liao, et al.: *Satellite-based entanglement distribution over 1200 kilometers*, Science **356**, 1140 (2017).

[10] H. J. Kimble: *The quantum internet*, Nature **453**, 1023 (2008).

[11] D. Chang, V. Vuletic, and M. Lukin: *Quantum nonlinear optics — photon by photon*, Nat. Photonics **8**, 685 (2014).

[12] W. K. Wootters and W. H. Zurek: *A single quantum cannot be cloned*, Nature **299**, 802 (1982).

[13] D. Dieks: *Communication by EPR Devices*, Phys. Lett. A **92**, 271 (1982).

[14] H.-J. Briegel, W. Dür, J. I. Cirac, and P. Zoller: *Quantum Repeaters: The Role of Imperfect Local Operations in Quantum Communication*, Phys. Rev. Lett. **81**, 5932 (1998).

[15] C. H. Bennett, G. Brassard, C. Crépeau, R. Jozsa, et al.: *Teleporting an unknown quantum state via dual classical and Einstein-Podolsky-Rosen channels*, Phys. Rev. Lett. **70**, 1895 (1993).

[16] N. Sangouard, C. Simon, H. De Riedmatten, and N. Gisin: *Quantum repeaters based on atomic ensembles and linear optics*, Rev. Mod. Phys. **83**, 33 (2011).

[17] N. Sangouard, R. Dubessy, and C. Simon: *Quantum Repeaters based on single trapped ions*, Phys. Rev. A **79**, 042340 (2009).

[18] N. Sangouard, C. Simon, J. Minar, H. Zbinden, et al.: *Long-distance entanglement distribution with single-photon sources*, Phys. Rev. A **76**, 050301 (R) (2007).

[19] N. Sangouard, C. Simon, B. Zhao, Y.-A. Chen, et al.: *Robust and efficient quantum repeaters with atomic ensembles and linear optics*, Phys. Rev. A **77**, 062301 (2008).

[20] L. M. Duan, M. D. Lukin, J. I. Cirac, and P. Zoller: *Long-distance quantum communication with atomic ensembles and linear optics.*, Nature **414**, 413 (2001).

[21] M. Zukowski, A. Zeilinger, M. A. Horne, and A. K. Ekert: *"Event-ready-detectors" Bell experiment via entanglement swapping*, Phys. Rev. Lett. **71**, 4287 (1993).

[22] C. W. Chou, H. de Riedmatten, D. Felinto, S. V. Polyakov, et al.: *Measurement-induced entanglement for excitation stored in remote atomic ensembles*, Nature **438**, 828 (2005).

[23] N. Lütkenhaus, J. Calsamiglia, and K.-A. Suominen: *Bell measurements for teleportation*, Phys. Rev. A **59**, 3295 (1999).

[24] J. Calsamiglia and N. Lütkenhaus: *Maximum efficiency of a linear-optical Bell-state analyzer*, Appl. Phys. B **72**, 67 (2001).

[25] M. Barrett, J. Chiaverini, T. Schaetz, J. Britton, et al.: *Deterministic quantum teleportation of atomic qubits*, Nature **429**, 737 (2004).

[26] M. Riebe, H. Häffner, C. Roos, W. Hänsel, et al.: *Deterministic quantum teleportation with atoms*, Nature **429**, 734 (2004).

[27] W. Pfaff, B. J. Hensen, H. Bernien, S. B. van Dam, et al.: *Unconditional quantum teleportation between distant solid-state quantum bits*, Science **345**, 532 (2014).

[28] J. Li, M.-T. Zhou, C.-W. Yang, P.-F. Sun, et al.: *Semideterministic Entanglement between a Single Photon and an Atomic Ensemble*, Phys. Rev. Lett. **123**, 140504 (2019).

[29] N. Sangouard, R. Dubessy, and C. Simon: *Quantum repeaters based on single trapped ions*, Phys. Rev. A **79**, 042340 (2009).

[30] A. Reiserer and G. Rempe: *Cavity-based quantum networks with single atoms and optical photons*, Rev. Mod. Phys. **87**, 1379 (2015).

[31] K. M. Birnbaum, A. Boca, R. Miller, A. D. Boozer, et al.: *Photon blockade in an optical cavity with one trapped atom*, Nature **436**, 87 (2005).

[32] A. Kubanek, A. Ourjoumtsev, I. Schuster, M. Koch, et al.: *Two-photon gateway in one-atom cavity quantum electrodynamics*, Phys. Rev. Lett. **101**, 203602 (2008).

[33] S. Welte, B. Hacker, S. Daiss, S. Ritter, et al.: *Photon-Mediated Quantum Gate between Two Neutral Atoms in an Optical Cavity*, Phys. Rev. X **8**, 011018 (2018).

[34] K. Hammerer, A. S. Sørensen, and E. S. Polzik: *Quantum interface between light and atomic ensembles*, Rev. Mod. Phys. **82**, 1041 (2010).

[35] T. Gallagher: *Rydberg Atoms*, Cambridge Monographs on Atomic, Molecular and Chemical Physics, Cambridge University Press (2005).

[36] T. Peyronel, O. Firstenberg, Q.-Y. Liang, S. Hofferberth, et al.: *Quantum nonlinear optics with single photons enabled by strongly interacting atoms*, Nature **488**, 57 (2012).

[37] M. Fleischhauer, A. Imamoglu, and J. P. Marangos: *Electromagnetically induced transparency: Optics in coherent media*, Rev. Mod. Phys. **77**, 633 (2005).

[38] M. Fox: *Quantum optics: an introduction*, vol. 15, OUP Oxford (2006).

[39] L.-M. Duan, M. D. Lukin, J. I. Cirac, and P. Zoller: *Long-distance quantum communication with atomic ensembles and linear optics*, Nature **414**, 413 (2001).

[40] D. Felinto, C. W. Chou, J. Laurat, E. W. Schomburg, et al.: *Conditional control of the quantum states of remote atomic memories for quantum networking*, Nat. Phys. **2**, 844 (2006).

[41] J. K. Thompson, J. Simon, H. Loh, and V. Vuletic: *A High-Brightness Source of Narrowband, Identical-Photon Pairs*, Science **313**, 74 (2006).

[42] M. Hijlkema, B. Weber, H. P. Specht, S. C. Webster, et al.: *A single-photon server with just one atom*, Nat. Phys. **3**, 253 (2007).

[43] J. McKeever, A. Boca, A. D. Boozer, R. Miller, et al.: *Deterministic Generation of Single Photons from One Atom Trapped in a Cavity*, Science **303**, 1992 (2004).

[44] M. Mücke, J. Bochmann, C. Hahn, A. Neuzner, et al.: *Generation of single photons from an atom-cavity system*, Phys. Rev. A **87**, 063805 (2013).

[45] D. B. Higginbottom, L. Slodička, G. Araneda, L. Lachman, et al.: *Pure single photons from a trapped atom source*, New Journal of Physics **18**, 093038 (2016).

[46] Y. L. A. Rezus, S. G. Walt, R. Lettow, A. Renn, et al.: *Single-Photon Spectroscopy of a Single Molecule*, Phys. Rev. Lett. **108**, 093601 (2012).

[47] I. Aharonovich, D. Englund, and M. Toth: *Solid-state single-photon emitters*, Nat. Photonics **10**, 631 (2016).

[48] C. Santori, D. Fattal, J. Vuckovic, G. S. Solomon, et al.: *Indistinguishable photons from a single-photon device*, Nature **419**, 594 (2002).

[49] B. Rodiek, M. Lopez, H. Hofer, G. Porrovecchio, et al.: *Experimental realization of an absolute single-photon source based on a single nitrogen vacancy center in a nanodiamond*, Optica **4**, 71 (2017).

[50] D. P. Ornelas-Huerta, A. N. Craddock, E. A. Goldschmidt, A. J. Hachtel, et al.: *On-demand indistinguishable single photons from an efficient and pure source based on a Rydberg ensemble*, Optica **7**, 813 (2020).

[51] F. Ripka, H. Kübler, R. Löw, and T. Pfau: *A room-temperature single-photon source based on strongly interacting Rydberg atoms*, Science **362**, 446 (2018).

[52] M. Saffman, T. G. Walker, and K. Molmer: *Quantum information with Rydberg atoms*, Rev. Mod. Phys. **82**, 2313 (2010).

[53] A. K. Mohapatra, T. R. Jackson, and C. S. Adams: *Coherent Optical Detection of Highly Excited Rydberg States Using Electromagnetically Induced Transparency*, Phys. Rev. Lett. **98**, 113003 (2007).

[54] M. Fleischhauer and M. D. Lukin: *Quantum memory for photons: Dark-state polaritons*, Phys. Rev. A **65**, 022314 (2002).

[55] M. Fleischhauer and M. D. Lukin: *Dark-state polaritons in electromagnetically induced transparency*, Phys. Rev. Lett. **84**, 5094 (2000).

[56] O. Firstenberg, C. S. Adams, and S. Hofferberth: *Nonlinear quantum optics mediated by Rydberg interactions*, J. Phys. B: At. Mol. Opt. Phys. **49**, 152003 (2016).

[57] C. S. Adams, J. D. Pritchard, and J. P. Shaffer: *Rydberg atom quantum technologies*, J. Phys. B: At. Mol. Opt. Phys. **53**, 012002 (2019).

[58] J. D. Pritchard, D. Maxwell, A. Gauguet, K. J. Weatherill, et al.: *Cooperative Atom-Light Interaction in a Blockaded Rydberg Ensemble*, Phys. Rev. Lett. **105**, 193603 (2010).

[59] Y. O. Dudin and A. Kuzmich: *Strongly Interacting Rydberg Excitations of a Cold Atomic Gas*, Science **336**, 887 (2012).

[60] D. Maxwell, D. J. Szwer, D. Paredes-Barato, H. Busche, et al.: *Storage and control of optical photons using Rydberg polaritons*, Phys. Rev. Lett. **110**, 1 (2013).

[61] O. Firstenberg, T. Peyronel, Q.-Y. Liang, A. V. Gorshkov, et al.: *Attractive photons in a quantum nonlinear medium.*, Nature **502**, 71 (2013).

[62] Q.-Y. Liang, A. V. Venkatramani, S. H. Cantu, T. L. Nicholson, et al.: *Observation of three-photon bound states in a quantum nonlinear medium*, Science **359**, 783 (2018).

[63] S. H. Cantu, A. V. Venkatramani, W. Xu, L. Zhou, et al.: *Repulsive photons in a quantum nonlinear medium*, Nat. Phys. 1–5 (2020).

[64] J. Li, M.-T. Zhou, B. Jing, X.-J. Wang, et al.: *Hong-Ou-Mandel Interference between Two Deterministic Collective Excitations in an Atomic Ensemble*, Phys. Rev. Lett. **117**, 180501 (2016).

[65] D. Petrosyan and K. Mølmer: *Deterministic free-space source of single photons using Rydberg atoms*, Phys. Rev. Lett. **121**, 123605 (2018).

[66] H. Busche, P. Huillery, S. W. Ball, T. Ilieva, et al.: *Contactless nonlinear optics mediated by long-range Rydberg interactions*, Nat. Phys. **13**, 655 (2017).

[67] I. Friedler, D. Petrosyan, M. Fleischhauer, and G. Kurizki: *Long-range interactions and entanglement of slow single-photon pulses*, Phys. Rev. A **72**, 043803 (2005).

[68] A. V. Gorshkov, J. Otterbach, M. Fleischhauer, T. Pohl, et al.: *Photon-Photon Interactions via Rydberg Blockade*, Phys. Rev. Lett. **107**, 133602 (2011).

[69] D. Paredes-Barato and C. S. Adams: *All-optical quantum information processing using rydberg gates*, Phys. Rev. Lett. **112**, 1 (2014).

[70] M. Khazali, K. Heshami, and C. Simon: *Photon-photon gate via the interaction between two collective Rydberg excitations*, Phys. Rev. A **91**, 030301 (2015).

[71] Y. Hao, G. Lin, X. Lin, Y. Niu, et al.: *Single-photon transistor based on cavity electromagnetically induced transparency with Rydberg atomic ensemble*, Sci. Rep. **9**, 1 (2019).

[72] Y. Han, B. He, K. Heshami, C.-Z. Li, et al.: *Quantum repeaters based on Rydberg-blockade-coupled atomic ensembles*, Phys. Rev. A **81**, 052311 (2010).

[73] B. Zhao, M. Müller, K. Hammerer, and P. Zoller: *Efficient quantum repeater based on deterministic Rydberg gates*, Phys. Rev. A **81**, 052329 (2010).

[74] D. Tiarks, S. Baur, K. Schneider, S. Dürr, et al.: *Single-photon transistor using a Förster resonance*, Phys. Rev. Lett. **113**, 1 (2014).

[75] H. Gorniaczyk, C. Tresp, J. Schmidt, H. Fedder, et al.: *Single-photon transistor mediated by interstate Rydberg interactions*, Phys. Rev. Lett. **113**, 1 (2014).

[76] S. Baur, D. Tiarks, G. Rempe, and S. Dürr: *Single-Photon Switch Based on Rydberg Blockade*, Phys. Rev. Lett. **112**, 1 (2014).

[77] H. Gorniaczyk, C. Tresp, P. Bienias, A. Paris-Mandoki, et al.: *Enhancement of Rydberg-mediated single-photon nonlinearities by electrically tuned Förster resonances*, Nat. Commun. **7**, 1 (2016).

[78] C. Tresp, C. Zimmer, I. Mirgorodskiy, H. Gorniaczyk, et al.: *Single-photon absorber based on strongly interacting Rydberg atoms*, Phys. Rev. Lett. **117**, 223001 (2016).

[79] D. Tiarks, S. Schmidt, G. Rempe, and S. Dürr: *Optical π phase shift created with a single-photon pulse*, Science Advances **2** (2016).

[80] D. Tiarks, S. Schmidt-Eberle, T. Stolz, G. Rempe, et al.: *A photon-photon quantum gate based on Rydberg interactions*, Nat. Phys. **15**, 124 (2019).

[81] L. Li and A. Kuzmich: *Quantum memory with strong and controllable Rydberg-level interactions*, Nat. Commun. **7**, 13618 (2016).

[82] L. Li, Y. O. Dudin, and A. Kuzmich: *Entanglement between light and an optical atomic excitation.*, Nature **498**, 466 (2013).

[83] E. Distante, P. Farrera, A. Padrón-Brito, D. Paredes-Barato, et al.: *Storing single photons emitted by a quantum memory on a highly excited Rydberg state*, Nat. Commun. **8** (2017).

[84] M. D. Lukin, M. Fleischhauer, R. Cote, L. M. Duan, et al.: *Dipole Blockade and Quantum Information Processing in Mesoscopic Atomic Ensembles*, Phys. Rev. Lett. **87**, 037901 (2001).

[85] D. Jaksch, J. I. Cirac, P. Zoller, S. L. Rolston, et al.: *Fast Quantum Gates for Neutral Atoms*, Phys. Rev. Lett. **85**, 2208 (2000).

[86] M. Saffman: *Quantum computing with atomic qubits and Rydberg interactions: progress and challenges*, J. Phys. B: At. Mol. Opt. Phys. **49**, 202001 (2016).

[87] X.-F. Shi: *Deutsch, Toffoli, and cnot Gates via Rydberg Blockade of Neutral Atoms*, Phys. Rev. Applied **9**, 051001 (2018).

[88] L. S. Theis, F. Motzoi, F. K. Wilhelm, and M. Saffman: *High-fidelity Rydberg-blockade entangling gate using shaped, analytic pulses*, Phys. Rev. A **94**, 032306 (2016).

[89] H. Levine, A. Keesling, A. Omran, H. Bernien, et al.: *High-Fidelity Control and Entanglement of Rydberg-Atom Qubits*, Phys. Rev. Lett. **121**, 123603 (2018).

[90] D. Yu, H. Wang, D. Ma, X. Zhao, et al.: *Adiabatic and high-fidelity quantum gates with hybrid Rydberg-Rydberg interactions*, Opt. Express **27**, 23080 (2019).

[91] L. Isenhower, E. Urban, X. L. Zhang, A. T. Gill, et al.: *Demonstration of a Neutral Atom Controlled-NOT Quantum Gate*, Phys. Rev. Lett. **104**, 010503 (2010).

[92] K. M. Maller, M. T. Lichtman, T. Xia, Y. Sun, et al.: *Rydberg-blockade controlled-not gate and entanglement in a two-dimensional array of neutral-atom qubits*, Phys. Rev. A **92**, 022336 (2015).

[93] I. I. Beterov, I. N. Ashkarin, E. A. Yakshina, D. B. Tretyakov, et al.: *Fast three-qubit Toffoli quantum gate based on three-body Förster resonances in Rydberg atoms*, Phys. Rev. A **98**, 042704 (2018).

[94] X. L. Zhang, L. Isenhower, A. T. Gill, T. G. Walker, et al.: *Deterministic entanglement of two neutral atoms via Rydberg blockade*, Phys. Rev. A **82**, 030306 (2010).

[95] T. Wilk, A. Gaetan, C. Evellin, J. Wolters, et al.: *Entanglement of Two Individual Neutral Atoms Using Rydberg Blockade*, Phys. Rev. Lett. **104**, 010502 (2010).

[96] H. Bernien, S. Schwartz, A. Keesling, H. Levine, et al.: *Probing many-body dynamics on a 51-atom quantum simulator*, Nature **551**, 579 (2017).

[97] D. Barredo, V. Lienhard, S. de Léséleuc, T. Lahaye, et al.: *Synthetic three-dimensional atomic structures assembled atom by atom*, Nature **561**, 79 (2018).

[98] V. Lienhard, S. de Léséleuc, D. Barredo, T. Lahaye, et al.: *Observing the Space- and Time-Dependent Growth of Correlations in Dynamically Tuned Synthetic Ising Models with Antiferromagnetic Interactions*, Phys. Rev. X **8**, 021070 (2018).

[99] P. Schauss: *Quantum simulation of transverse Ising models with Rydberg atoms*, Quantum Sci. Technol. **3**, 023001 (2018).

[100] A. Browaeys and T. Lahaye: *Many-body physics with individually controlled Rydberg atoms*, Nat. Phys. 1–11 (2020).

[101] E. Distante: *A quantum light-matter interface with Rydberg polaritons in a cold atomic ensemble*, Ph.D. thesis, Universitat Politecnica de Catalunya (2017).

[102] P. Bienias, J. Douglas, A. Paris-Mandoki, P. Titum, et al.: *Photon propagation through dissipative Rydberg media at large input rates*, Phys. Rev. Research **2**, 033049 (2020).

[103] D. Maxwell, D. J. Szwer, D. Paredes-Barato, H. Busche, et al.: *Microwave control of the interaction between two optical photons*, Phys. Rev. A **89**, 043827 (2014).

[104] A. N. Craddock, J. Hannegan, D. P. Ornelas-Huerta, J. D. Siverns, et al.: *Quantum Interference between Photons from an Atomic Ensemble and a Remote Atomic Ion*, Phys. Rev. Lett. **123**, 213601 (2019).

[105] C. Murray and T. Pohl: *Quantum and nonlinear optics in strongly interacting atomic ensembles*, in *Advances in Atomic, Molecular, and Optical Physics*, vol. 65, 321–372, Elsevier (2016).

[106] H. Busche: *Contactless quantum non-linear optics with cold Rydberg atoms*, Ph.D. thesis, Durham University (2017).

[107] A. Browaeys and T. Lahaye: *Interacting cold Rydberg atoms: a toy many-body system*, in *Niels Bohr, 1913-2013*, 177–198, Springer (2016).

[108] J. D. Pritchard: *Cooperative Optical Non-linearity in a blockaded Rydberg ensemble*, Ph.D. thesis, Durham University (2011).

[109] D. Paredes-Barato: *Towards optical quantum information processing using Rydberg dark-state polaritons*, Ph.D. thesis, Durham University (2014).

[110] H. J. Kimble, M. Dagenais, and L. Mandel: *Photon antibunching in resonance fluorescence*, Phys. Rev. Lett. **39**, 691 (1977).

[111] R. H. Brown and R. Q. Twiss: *Correlation between photons in two coherent beams of light*, Nature **177**, 27 (1956).

[112] R. H. Brown, R. Q. Twiss, and g. surName: *Interferometry of the intensity fluctuations in light-i. basic theory: the correlation between photons in coherent beams of radiation*, Proceedings of the Royal Society of London. Series A. Mathematical and Physical Sciences **242**, 300 (1957).

[113] R. H. Brown and R. Twiss: *Interferometry of the intensity fluctuations in light. II. An experimental test of the theory for partially coherent light*, Proceedings of the Royal Society of London. Series A. Mathematical and Physical Sciences **243**, 291 (1958).

[114] C. K. Hong, Z. Y. Ou, and L. Mandel: *Measurement of subpicosecond time intervals between two photons by interference*, Phys. Rev. Lett. **59**, 2044 (1987).

[115] H. Chen, X.-B. An, J. Wu, Z.-Q. Yin, et al.: *Hong–Ou–Mandel interference with two independent weak coherent states*, Chin. Phys. B **25**, 020305 (2016).

[116] L. V. Hau, S. E. Harris, Z. Dutton, and C. H. Behroozi: *Light speed reduction to 17 metres per second in an ultracold atomic gas*, Nature **397**, 594 (1999).

[117] D. F. Phillips, A. Fleischhauer, A. Mair, R. L. Walsworth, et al.: *Storage of Light in Atomic Vapor*, Phys. Rev. Lett. **86**, 783 (2001).

[118] Y. O. Dudin, L. Li, and A. Kuzmich: *Light storage on the time scale of a minute*, Phys. Rev. A **87**, 031801 (2013).

[119] Y.-F. Hsiao, P.-J. Tsai, H.-S. Chen, S.-X. Lin, et al.: *Highly Efficient Coherent Optical Memory Based on Electromagnetically Induced Transparency*, Phys. Rev. Lett. **120**, 183602 (2018).

[120] J. D. Pritchard, K. J. Weatherill, and C. S. : *Nonlinear optics using cold Rydberg atoms*, in *Annual Review of Cold Atoms and Molecules: Volume 1*, 301–350, World Scientific (2013).

[121] D. Petrosyan, J. Otterbach, and M. Fleischhauer: *Electromagnetically induced transparency with Rydberg atoms*, Phys. Rev. Lett. **107**, 213601 (2011).

[122] E. Distante, A. Padrón-Brito, M. Cristiani, D. Paredes-Barato, et al.: *Storage Enhanced Nonlinearities in a Cold Atomic Rydberg Ensemble*, Phys. Rev. Lett. **117**, 113001 (2016).

[123] A. V. Gorshkov, R. Nath, and T. Pohl: *Dissipative Many-Body Quantum Optics in Rydberg Media*, Phys. Rev. Lett. **110**, 153601 (2013).

[124] E. Zeuthen, M. J. Gullans, M. F. Maghrebi, and A. V. Gorshkov: *Correlated photon dynamics in dissipative Rydberg media*, Phys. Rev. Lett. **119**, 043602 (2017).

[125] T. Cubel, B. Teo, V. Malinovsky, J. R. Guest, et al.: *Coherent population transfer of ground-state atoms into Rydberg states*, Phys. Rev. A **72**, 023405 (2005).

[126] B. Zhao, Y.-A. Chen, X.-H. Bao, T. Strassel, et al.: *A millisecond quantum memory for scalable quantum networks*, Nat. Phys. **5**, 95 (2009).

[127] X.-F. Shi: *Suppressing Motional Dephasing of Ground-Rydberg Transition for High-Fidelity Quantum Control with Neutral Atoms*, Phys. Rev. Applied **13**, 024008 (2020).

[128] D. H. Meyer, Z. A. Castillo, K. C. Cox, and P. D. Kunz: *Assessment of Rydberg atoms for wideband electric field sensing*, J. Phys. B: At. Mol. Opt. Phys. **53**, 034001 (2020).

[129] J. Qiu, D. Fang, W. Xie, and S. Zhang: *Environmental radiation effect of atomic Rydberg states*, Journal of Quantitative Spectroscopy and Radiative Transfer **62**, 647 (1999).

[130] I. Beterov, D. Tretyakov, I. Ryabtsev, V. Entin, et al.: *Ionization of Rydberg atoms by blackbody radiation*, New Journal of Physics **11**, 013052 (2009).

[131] M. Schlagmüller, T. C. Liebisch, F. Engel, K. S. Kleinbach, et al.: *Ultracold chemical reactions of a single Rydberg atom in a dense gas*, Phys. Rev. X **6**, 031020 (2016).

[132] D. Sadler, E. Bridge, D. Boddy, A. Bounds, et al.: *Radiation trapping in a dense cold Rydberg gas*, Phys. Rev. A **95**, 013839 (2017).

[133] S. Schmidt-Eberle, T. Stolz, G. Rempe, and S. Dürr: *Dark-time decay of the retrieval efficiency of light stored as a Rydberg excitation in a noninteracting ultracold gas*, Phys. Rev. A **101**, 013421 (2020).

[134] F. Bariani, Y. O. Dudin, T. A. B. Kennedy, and A. Kuzmich: *Dephasing of Multiparticle Rydberg Excitations for Fast Entanglement Generation*, Phys. Rev. Lett. **108**, 030501 (2012).

[135] F. Bariani, P. M. Goldbart, and T. A. B. Kennedy: *Dephasing dynamics of Rydberg atom spin waves*, Phys. Rev. A **86**, 041802 (2012).

[136] B. Albrecht: *Quantum control of single spin excitations in cold atomic quantum memories*, Ph.D. thesis, Universitat Politecnica de Catalunya (2015).

[137] E. L. Raab, M. Prentiss, A. Cable, S. Chu, et al.: *Trapping of Neutral Sodium Atoms with Radiation Pressure*, Phys. Rev. Lett. **59**, 2631 (1987).

[138] *ComponentLibrary by Alexander Franzen, under a Creative Commons Attribution-NonCommercial 3.0 Unported License*.

[139] C. J. Foot et al.: *Atomic physics*, vol. 7, Oxford University Press (2005).

[140] W. Petrich, M. H. Anderson, J. R. Ensher, and E. A. Cornell: *Behavior of atoms in a compressed magneto-optical trap*, J. Opt. Soc. Am. B **11**, 1332 (1994).

[141] R. Grimm, M. Weidemüller, and Y. B. Ovchinnikov: *Optical dipole traps for neutral atoms*, Advances in Atomic, Molecular and Optical Physics **42**, 95 (2000).

[142] S. J. M. Kuppens, K. L. Corwin, K. W. Miller, T. E. Chupp, et al.: *Loading an optical dipole trap*, Phys. Rev. A **62**, 013406 (2000).

[143] H. J. Metcalf and P. van der Straten: *Laser cooling and trapping*, Springer (1999).

[144] C. Möhl, N. L. Spong, Y. Jiao, C. So, et al.: *Photon correlation transients in a weakly blockaded Rydberg ensemble*, J. Phys. B: At. Mol. Opt. Phys. **53**, 084005 (2020).

[145] A. Padrón-Brito, R. Tricarico, P. Farrera, E. Distante, et al.: *Transient dynamics of the quantum light retrieved from Rydberg polaritons* (2020).

[146] A. Padrón-Brito, J. Lowinski, P. Farrera, K. Theophilo, et al.: *Probing the indistinguishability of single photons generated by Rydberg atomic ensembles* (2020).

[147] R. Uppu, T. A. Wolterink, T. B. Tentrup, and P. W. Pinkse: *Quantum optics of lossy asymmetric beam splitters*, Opt. Express **24**, 16440 (2016).

[148] L. Mandel: *Photon interference and correlation effects produced by independent quantum sources*, Phys. Rev. A **28**, 929 (1983).

[149] J. Jin, J. A. Slater, E. Saglamyurek, N. Sinclair, et al.: *Two-photon interference of weak coherent laser pulses recalled from separate solid-state quantum memories*, Nat Commun **4**, (2013).

[150] T. Legero, T. Wilk, A. Kuhn, and G. Rempe: *Time-resolved two-photon quantum interference*, Appl. Phys. B **77**, 797 (2003).

[151] J. Beugnon, M. P. Jones, J. Dingjan, B. Darquié, et al.: *Quantum interference between two single photons emitted by independently trapped atoms*, Nature **440**, 779 (2006).

[152] D. Felinto, C.-W. Chou, J. Laurat, E. Schomburg, et al.: *Conditional control of the quantum states of remote atomic memories for quantum networking*, Nat. Phys. **2**, 844 (2006).

[153] M. Meraner, A. Mazloom, V. Krutyanskiy, V. Krcmarsky, et al.: *Indistinguishable photons from a trapped-ion quantum network node*, Phys. Rev. A **102**, 052614 (2020).

[154] P. Farrera, G. Heinze, and H. De Riedmatten: *Entanglement between a photonic time-bin qubit and a collective atomic spin excitation*, Phys. Rev. Lett. **120**, 100501 (2018).

[155] J. de Hond, N. Cisternas, G. Lochead, and N. Van Druten: *Medium-finesse optical cavity for the stabilization of Rydberg lasers*, Applied optics **56**, 5436 (2017).

[156] J. B. Naber, J. Vos, R. J. Rengelink, R. J. Nusselder, et al.: *Optical techniques for Rydberg physics in lattice geometries*, The European Physical Journal Special Topics **225**, 2785 (2016).